Review | Open Access

Energy Materials

Lu *et al. Energy Mater.* **2026**, *6*, 600134 **DOI:**10.20517/energymater.2026.235

# Structure-informed two-electron electrocatalysis for selective redox synthesis

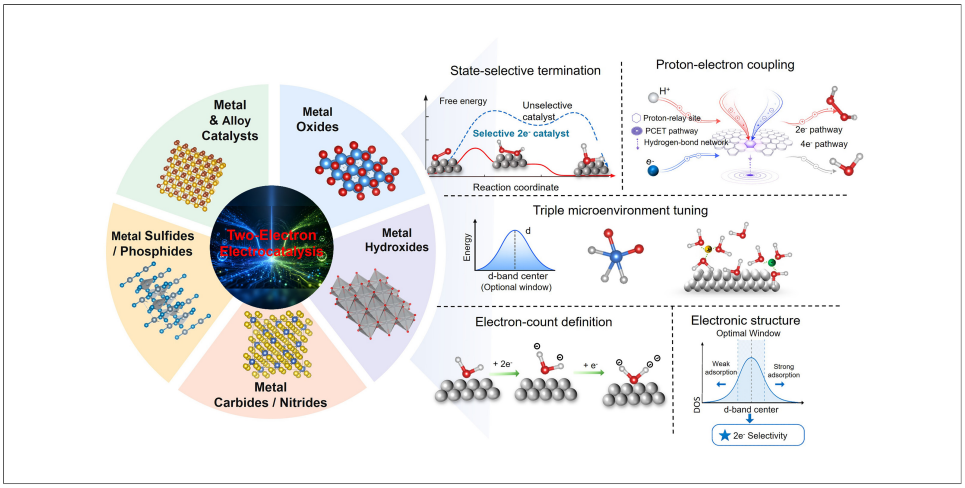
**Yujia Lu[1,#], Jiamu Feng[1,#], Linai Zhou[1], Hui Wang[2], Weilin Xu[1,*], Jun Wan[1,*]**

**Keywords:**
Two-electron electrocatalysis, hydrogen peroxide electrosynthesis, carbon dioxide reduction, nitrate electroreduction, halide electro-oxidation

**Citation:** Lu, Y.; Feng, J.; Zhou, L.; Wang, H.; Xu, W.; Wan, J. Structure-informed two-electron electrocatalysis for selective redox synthesis. *Energy Mater.* **2026**, *6*, 600134. https://dx.doi.org/10.20517/energymater.2026.235

**Received:** 23 Jul 2026
**First Decision:** 13 Aug 2026
**Revised:** 3 Sep 2026
**Accepted:** 4 Sep 2026
**Published:** 19 Oct 2026

**Academic Editor:**
Yuhui Chen
**Copy Editor:**
Fangling Lan
**Production Editor:**
Fangling Lan




## Abstract

Two-electron electrocatalysis has attracted increasing attention because many high-value molecules, including hydrogen peroxide, formate, nitrite, and halogens, correspond to intermediate oxidation states that cannot be obtained efficiently through conventional multielectron electrocatalytic pathways. Achieving selective termination at the two-electron level therefore represents a fundamental requirement for oxidation-state-precise electrosynthesis, yet progress in this field has remained conceptually fragmented since most studies focus on individual reactions or catalyst systems rather than the underlying chemical principles governing two-electron selectivity. This review addresses that gap by establishing a unified framework that connects reaction classes, competing electron-transfer pathways, structural determinants of selectivity, catalyst families, and representative reaction-specific advances across oxygen, carbon dioxide, nitrogen-oxoanion, and halide chemistries. Particular emphasis is placed on how active-site electronic structure, coordination environment, surface and defect chemistry, crystal phase, and interfacial microenvironment collectively determine whether catalytic interfaces terminate reactivity at the two-electron level or proceed toward deeper redox manifolds.

Check for updates

[1]State Key Laboratory of New Textile Materials and Advanced Processing, School of Chemistry and Environmental Engineering, Wuhan Textile University, Wuhan 430200, Hubei, China.
[2]School of Materials Science and Engineering, Nanyang Technological University, Singapore 639798, Singapore.
[#]Authors contributed equally.

***Correspondence to:** Prof. Weilin Xu, Prof. Jun Wan, State Key Laboratory of New Textile Materials and Advanced Processing, School of Chemistry and Environmental Engineering, Wuhan Textile University, 1 Sunshine Avenue, Jiangxia District, Wuhan 430200, Hubei, China. E-mail: weilin_xu@wtu.edu.cn; wanj@wtu.edu.cn

By integrating reaction chemistry with materials structural chemistry, this review moves the field beyond reaction-specific observations toward a broader understanding of oxidation-state-precise electrosynthesis. Such a perspective provides a conceptual basis for transferable catalyst design and offers important implications for selective molecular manufacturing and future electrochemical synthesis.

## INTRODUCTION

Electrocatalysis has redefined the chemical logic of small-molecule conversion by making electron transfer number itself a controllable synthetic variable rather than a passive consequence of redox thermodynamics. In many inorganic reaction systems, the decisive question is no longer whether a substrate such as $O_2$, $H_2O$, $CO_2$, $NO_3^-$, or $X^-$ can be activated at an electrode interface, but whether the catalytic process can be arrested at a prescribed redox level before further oxidation or reduction becomes dominant. This issue gives two-electron electrocatalysis a significance that is both fundamental and practical[1,2]. At the fundamental level, two-electron pathways occupy a chemically sensitive position within multistep proton-coupled electron transfer networks, where the first bond rearrangement, the first oxygen-atom transfer, or the first heteroatom protonation event often determines whether the reaction remains on a partially transformed pathway or evolves toward deeper reduction or oxidation products[3]. At the practical level, many two-electron products are themselves terminal targets rather than incomplete intermediates, because they embody distinct molecular functions, separation profiles, and downstream reactivity that cannot be replaced by fully oxidized or fully reduced analogs. The central importance of two-electron electrocatalysis therefore does not arise simply from a smaller electron count[4,5]. It arises because a two-electron process is frequently the first redox threshold at which catalytic selectivity becomes chemically meaningful. Once this threshold is crossed in an uncontrolled manner, the catalytic system often loses access to valuable molecules and collapses into thermodynamically deeper but functionally less selective outcomes[6]. For this reason, two-electron electrocatalysis represents one of the clearest manifestations of selective redox synthesis in modern chemistry. It provides a stringent platform for understanding how catalytic interfaces encode oxidation-state precision, how intermediate lifetimes are translated into product identity, and how reaction networks can be steered toward defined molecular endpoints under nonequilibrium electrochemical conditions[7,8].

Precisely because two-electron electrocatalysis lies at this boundary between activation and overconversion, it remains chemically difficult in a way that cannot be resolved by activity enhancement alone. The principal challenge is that two-electron products are usually formed in reaction landscapes where deeper electron-transfer pathways are intrinsically available, and often thermodynamically favored once the initial activation barrier has been overcome[9]. As a result, the problem of two-electron selectivity is fundamentally a problem of controlling intermediate-state fate. The catalytic interface must be sufficiently reactive to induce substrate activation, yet sufficiently discriminating to prevent subsequent elementary steps that would consume the desired partially transformed species. This requirement creates a delicate and highly nonlinear coupling among adsorption energetics, charge redistribution, proton availability, solvent organization, and surface redox flexibility[10,11]. Considerable progress has been made by tuning catalyst composition, alloying motifs, heteroatom coordination, defect populations, crystal phases, and electrolyte environments, all of which can shift the relative stability of key adsorbed states and alter the competition between two-electron and multielectron pathways[12-14]. However, current understanding remains fragmented in two important senses. First, most studies are organized around individual reactions, so the underlying commonality of two-electron selectivity across oxygen, carbon, nitrogen, and halide chemistries remains insufficiently extracted. Second, even when selectivity is improved, mechanistic interpretation is often partitioned into isolated descriptors such as adsorption energy, oxidation state, vacancy concentration, or local pH, without clarifying how chemical structure and materials structural chemistry operate together as an integrated selectivity framework. What remains lacking is not merely additional examples of selective catalysts, but a unified

conceptual language that links electron-transfer number to active-site electronic structure, local coordination geometry, surface and defect chemistry, crystal-phase characteristics, and interfacial microenvironment[15-17]. Without such a framework, it is difficult to distinguish universal design principles from reaction-specific observations, to compare catalysts developed in different subfields on a chemically consistent basis, or to rationally predict when a catalyst will terminate reactivity at the two-electron level rather than proceed toward deeper redox manifolds[18,19].

Herein, this review is organized to address that gap through a chemistry-centered and structure-informed analysis of inorganic two-electron electrocatalysis. It first establishes the conceptual foundation of two-electron electrocatalysis by clarifying its governing principles, scientific importance, and broader significance within selective redox chemistry. It then classifies the major inorganic two-electron reaction families, including oxygen-related, carbon dioxide-related, nitrogen-oxoanion, and halide systems, with explicit attention to their competition against four-electron and deeper pathways. Building on this reaction map, the review next examines the principal structural determinants of two-electron selectivity, focusing on active-site electronic structure, local coordination environment and atomic configuration, surface structure, defects and crystal phases, and interfacial microenvironment effects [Figure 1]. The catalyst landscape is subsequently organized across metals and alloys, metal oxides and oxide-derived materials, metal hydroxides, metal sulfides and phosphides, metal carbides and nitrides, and other emerging catalytic materials, together with a comparative summary of catalyst distributions and performance metrics across reported systems. On this basis, representative reaction-specific advances are discussed for the two-electron oxygen reduction reaction, two-electron water oxidation reaction, two-electron carbon dioxide reduction reaction, two-electron nitrate reduction reaction, and two-electron halide oxidation reaction. By integrating reaction chemistry, structural chemistry, and catalyst science into a common analytical framework, this review aims to move the field beyond reaction-by-reaction description toward a more general understanding of how two-electron selectivity is chemically encoded, thereby providing a basis for the rational design of electrocatalytic systems for high-value molecular synthesis and selective inorganic redox transformation.

## CONCEPTUAL FRAMEWORK OF TWO-ELECTRON ELECTROCATALYSIS

### Fundamentals and significance of two-electron electrocatalysis

Two-electron electrocatalysis is most appropriately understood not as a simplified subset of multielectron electrochemistry, but as a distinct regime of selective redox chemistry in which the catalytic interface directs a substrate toward a defined oxidation-state change of exactly two electrons per product-forming event. Its conceptual foundation therefore rests on three tightly connected dimensions [Figure 2]. The first is electron-count definition, because the number of transferred electrons determines the redox depth of the product and thus its chemical identity. For $O_2$ reduction, a two-electron pathway terminates at $H_2O_2$ rather than $H_2O$. For $CO_2$ reduction, a two-electron process can yield HCOOH or $HCOO^-$ rather than more deeply reduced $C_1$ or $C_2$ products. For nitrate reduction, a two-electron transformation gives $NO_2^-$ as a discrete nitrogen-oxo product rather than $NH_3$ or $N_2$[20-22]. The second is state-selective termination, because a two-electron process is meaningful only when the catalyst does not merely pass through a partially transformed intermediate, but allows the reaction network to stop at that state with chemically significant selectivity. In this sense, two-electron electrocatalysis differs fundamentally from a transient elementary step embedded within a longer cascade. It describes a catalytic outcome in which the two-electron product has sufficient kinetic persistence and interfacial release probability to emerge as the dominant observable species[23]. A critical distinction should therefore be made between a terminal two-electron product and a transient intermediate in a multielectron pathway. After formation, the two-electron state may either desorb or undergo further surface reactions. A sufficiently long interfacial lifetime and high desorption probability favor its accumulation as the dominant product, whereas strong surface binding and rapid downstream conversion lead to further redox chemistry. Thus, two-electron selectivity depends not simply on two-electron transfer, but on kinetic

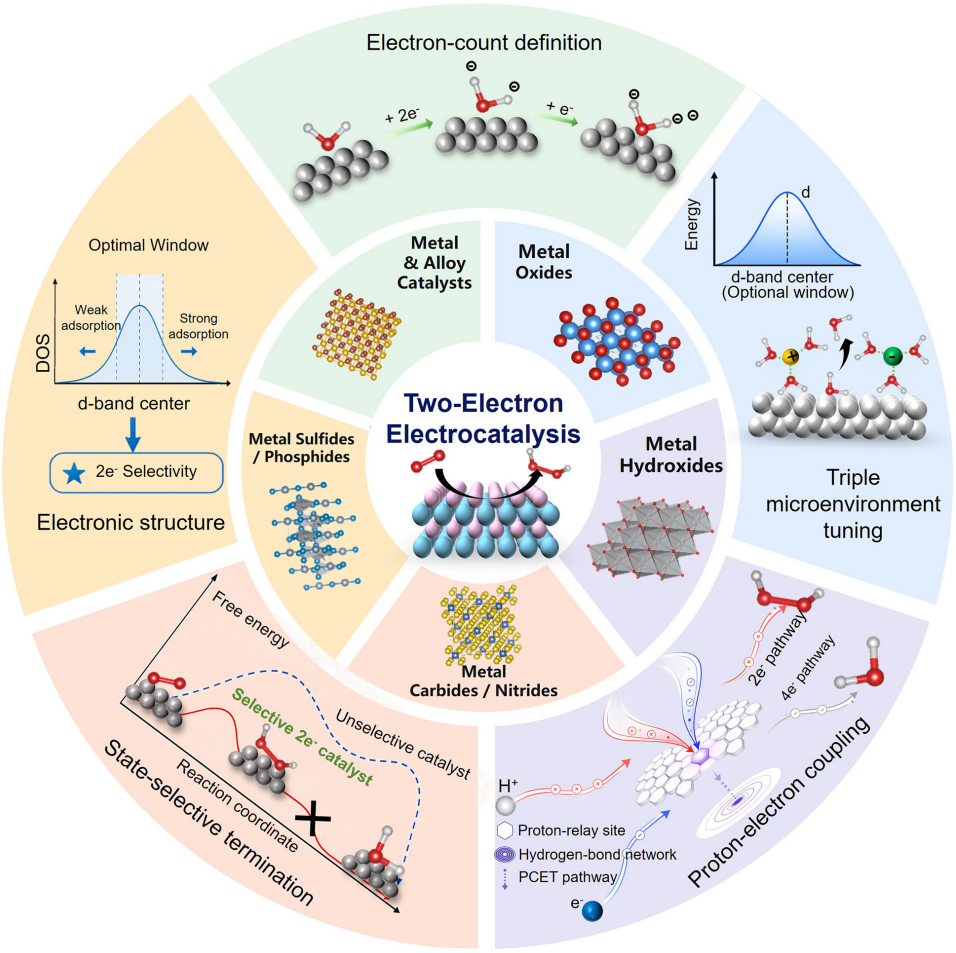



**Figure 1.** Schematic overview of two-electron electrocatalysis and selectivity regulation strategies.

termination at the corresponding redox state. The third is proton-electron coupling, because most inorganic two-electron processes do not proceed through electron transfer alone, but through proton-coupled electron transfer sequences that jointly govern charge compensation, bond polarization, and product speciation. This coupling determines whether the same nominal two-electron conversion appears as $H_2O_2$, $HO_2^-$, HCOOH, or $HCOO^-$ under different pH conditions, and it also dictates whether key intermediates remain electrophilic, nucleophilic, radical-like, or protonated at the moment of bond formation or cleavage[24,25]. On this basis, the fundamental concept of two-electron electrocatalysis can be defined more rigorously as the electrocatalytic control of a reaction network such that substrate activation, intermediate transformation, and product desorption are orchestrated to realize a chemically discrete two-electron redox endpoint under nonequilibrium interfacial conditions. This definition already implies that two-electron selectivity cannot be reduced to a simple thermodynamic preference. It is a kinetic and chemical organization problem in which the catalyst must satisfy two conditions simultaneously. It must lower the barrier for the first productive transformation, and it must prevent the newly formed redox state from being re-engaged in further electron-transfer chemistry. The basic principles governing such behavior follow logically from this definition[26-28]. A two-electron pathway becomes accessible when the free-energy landscape allows initial substrate activation and key intermediate formation at a reasonable overpotential, yet does not strongly favor subsequent bond cleavage, deeper protonation, or continued electron accumulation. The catalytic interface must therefore operate within an unusually narrow reactivity window, where adsorption is strong enough to trigger transformation but weak enough to permit release of the partially converted product. This balance gives

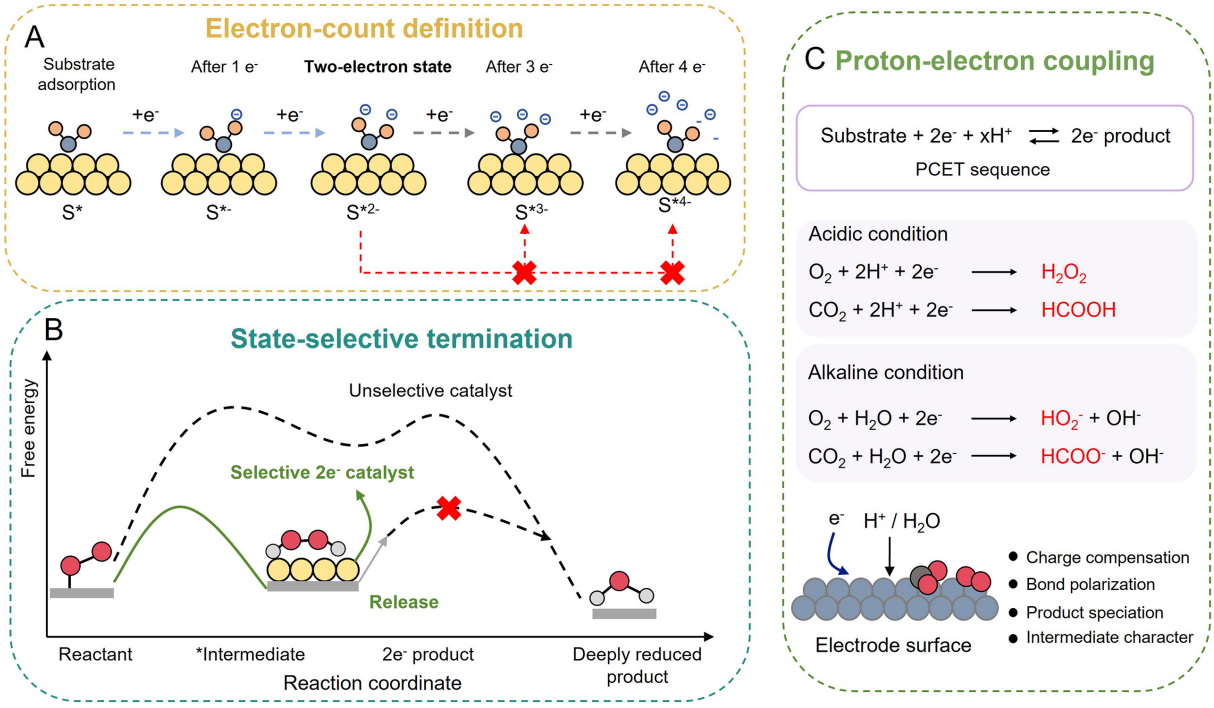



**Figure 2.** Fundamental concepts underlying two-electron electrocatalysis and selectivity control. (A) Electron-count definition of the two-electron state during substrate activation. (B) Free-energy landscapes illustrating selective two-electron termination and competing reaction pathways. (C) Representative proton-coupled electron transfer (PCET) mechanisms governing typical two-electron electrocatalytic reactions.

two-electron electrocatalysis its distinctive mechanistic character. It is governed by redox-level precision rather than maximal conversion depth, by kinetic arrest rather than complete thermodynamic descent, and by selective intermediate management rather than indiscriminate activation[29,30].

The scientific importance of two-electron electrocatalysis follows directly from this mechanistic position, because two-electron processes define the earliest stage at which catalytic systems begin to express true chemical selectivity within complex redox networks. That importance can be viewed at three progressively broader levels. At the first level, two-electron electrocatalysis is significant as a model problem in interfacial chemical dynamics, since it reveals how adsorption, proton transfer, charge redistribution, and desorption cooperate to determine whether a catalytic event remains partial or becomes overextended. It therefore provides an especially stringent testing ground for mechanistic concepts such as proton-coupled electron transfer, scaling relations, interfacial field effects, and the competition between surface retention and molecular release[31,32]. At the second level, it is significant as a synthetic principle for selective electrosynthesis, because many two-electron products possess intrinsic value precisely due to their intermediate redox state. Molecules such as $H_2O_2$ and HCOOH are not desirable because they are partially transformed, but because that partial transformation gives rise to distinctive oxidizing ability, hydrogen-storage capacity, reactivity, transport behavior, and downstream utility that cannot be reproduced by deeper oxidation or reduction products[33]. In this respect, two-electron electrocatalysis offers an alternative to conventional chemical manufacture by enabling direct access to oxidation-state-specific molecules from abundant feedstocks such as $O_2$, $H_2O$, $CO_2$, and $NO_3^-$ through electricity-driven routes[34-36]. At the third and broadest level, two-electron electrocatalysis is significant as a conceptual bridge between molecular redox chemistry and catalyst design, because it forces the field to confront the question of how far a reaction should proceed rather than how fast it can proceed. This distinction has far-reaching implications. Much of classical electrocatalyst development has been guided by the pursuit of lower overpotential, higher current density,

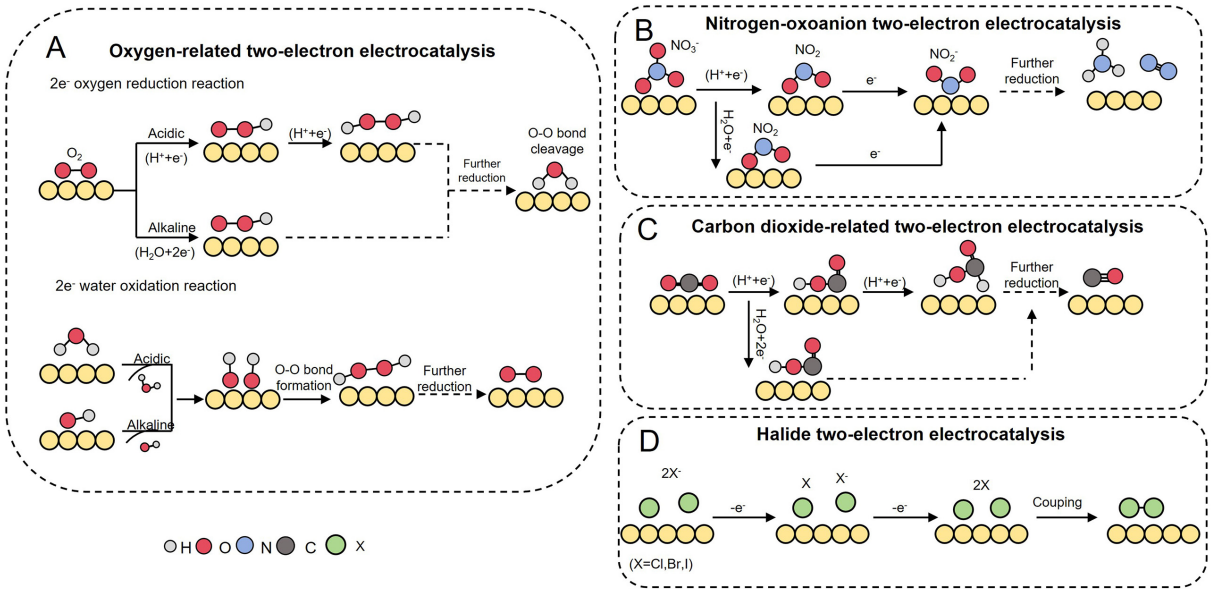



**Figure 3.** Schematic overview of representative two-electron electrocatalytic reactions and mechanisms. (A) Oxygen-related two-electron pathways, including oxygen reduction and water oxidation. (B) Nitrogen-oxyanion reduction through nitrate/nitrite-derived intermediates. (C) $CO_2$ reduction through representative carboxyl- and formate-type intermediates. (D) Halide oxidation via sequential electron transfer and halogen coupling.

and faster turnover[37,38]. Two-electron chemistry exposes the limitation of that logic, since greater activity alone may accelerate the undesired descent into deeper redox manifolds. The more relevant objective becomes chemically resolved selectivity, namely the ability to encode a target oxidation-state change into the catalytic interface itself. For this reason, two-electron electrocatalysis is not only an application-oriented subfield, but also a framework that reshapes how electrocatalytic performance is interpreted. It moves the emphasis from total electron throughput to electron-allocation fidelity, from maximal bond activation to controlled bond reorganization, and from reaction completion to reaction definition. Such a shift is scientifically necessary for the next stage of electrosynthesis, because the future utility of electrochemical conversion will depend not only on replacing thermochemical steps with electrical ones, but on achieving a finer degree of molecular control over how electrons are delivered, where they are stopped, and which chemical function is ultimately created.

## Reaction classes and competing electron-transfer pathways

The reaction landscape of two-electron electrocatalysis can be organized most coherently according to the chemical identity of the substrate and the redox logic of the corresponding product manifold. Such a classification is not merely descriptive. It provides a chemically meaningful basis for comparing systems in which the same nominal two-electron transfer leads to fundamentally different bond-evolution patterns, proton-coupling requirements, and selectivity constraints [Figure 3]. Oxygen-related reactions are governed primarily by O-O bond preservation or formation, carbon dioxide-related reactions by the selective stabilization of partially reduced carbon-oxygen intermediates, nitrogen-oxoanion systems by controlled deoxygenation without excessive hydrogenation, and halide chemistry by the competition between halogen evolution and oxygen-centered oxidation[39]. Considered together, these four classes capture the principal inorganic reaction families in which two-electron pathways emerge as chemically discrete and technologically relevant outcomes. More importantly, this classification makes it possible to examine two-electron chemistry not as a collection of isolated examples, but as a set of related selectivity problems embedded within competing multielectron networks[40-42]. On this basis, the following sections discuss these reaction classes in sequence, with emphasis on how their characteristic two-electron pathways are defined and how they contend with deeper electron-transfer channels.

### *Oxygen-related two-electron electrocatalysis*

Oxygen-related two-electron electrocatalysis constitutes the most archetypal and chemically instructive class within this field because it places selectivity control directly on the question of whether an O-O unit is preserved, generated, or cleaved during interfacial redox transformation[43]. Its core importance arises from the fact that both the cathodic reduction of $O_2$ and the anodic oxidation of $H_2O$ can, in principle, terminate at $H_2O_2$ as a discrete two-electron product, yet the mechanistic logic by which this occurs is fundamentally different on the reduction and oxidation sides[44-46]. In the two-electron oxygen reduction reaction, the essential chemical requirement is retention of the O-O bond throughout activation and proton-coupled electron transfer, typically described in acidic medium by $O_2 + 2H^+ + 2e^- \rightarrow H_2O_2$ and in alkaline medium by $O_2 + H_2O + 2e^- \rightarrow HO_2^- + OH^-$[47,48]. The defining selectivity problem is therefore not oxygen activation itself, but the ability of the catalytic interface to activate $O_2$ sufficiently to form an adsorbed hydroperoxo-type intermediate while avoiding subsequent O-O scission that would divert the pathway toward the four-electron reduction to $H_2O$[49-51]. This makes the oxygen reduction case a highly sensitive expression of intermediate-state control, since the same interfacial reactivity that enables $O_2$ adsorption and reduction can also facilitate bond cleavage if the surface binds oxygen-containing fragments too strongly. By contrast, in the two-electron water oxidation reaction, described in acidic conditions as $2H_2O \rightarrow H_2O_2 + 2H^+ + 2e^-$ or in alkaline conditions as $2OH^- \rightarrow H_2O_2 + 2e^-$, the chemical challenge is not bond preservation but selective O-O bond formation at the peroxide oxidation level without further oxidation to $O_2$. The catalytic interface must therefore create an oxygen-coupling route that terminates at peroxide rather than continuing into the thermodynamically and kinetically dominant four-electron oxygen evolution manifold[52-54]. This distinction is chemically profound. In oxygen reduction, two-electron selectivity is achieved by suppressing overreduction after initial oxygen activation[55,56]. In water oxidation, it is achieved by suppressing overoxidation after initial oxygen coupling[57]. The oxygen-related family thus defines a complete redox pair in which the same product, $H_2O_2$, can be approached either from molecular oxygen or from water, while the central selectivity principle remains the same: the catalytic process must stabilize the peroxide redox level as a chemically persistent endpoint. For this reason, oxygen-related two-electron electrocatalysis has become a benchmark system for understanding how proton-coupled electron transfer, O-O bond chemistry, and product desorption are coordinated under nonequilibrium electrochemical conditions. It also provides a uniquely revealing framework for distinguishing two-electron and four-electron pathways in chemical terms[58,59]. The two-electron route privileges peroxide formation as a redox-defined molecular outcome, whereas the four-electron route drives the system toward the more thermodynamically relaxed endpoints of $H_2O$ production or $O_2$ evolution. The competition between these pathways is therefore not simply a difference in electron number. It is a competition between two fundamentally different reaction logics, one centered on selective access to an oxygenated molecular oxidant and the other on complete redox exhaustion of the oxygen substrate[60,61]. This is precisely why oxygen-related two-electron electrocatalysis occupies such a central place in the broader framework of selective electrosynthesis: it captures, in its most explicit form, the chemical problem of how an electrocatalytic interface can recognize a partially transformed oxygen state as the desired product rather than as a transient species to be consumed further.

### *Carbon dioxide-related two-electron electrocatalysis*

Carbon dioxide-related two-electron electrocatalysis represents a chemically distinctive branch of $CO_2$ conversion because it seeks to arrest carbon at an early reduction level where the carbon atom remains bound to oxygen, yet has already undergone a discrete change in electron density and protonation state sufficient to generate a synthetically useful product. In its most representative form, this chemistry is expressed by the two-electron reduction of $CO_2$ to formic acid or formate, written as $CO_2 + 2H^+ + 2e^- \rightarrow HCOOH$ in acidic media or $CO_2 + H_2O + 2e^- \rightarrow HCOO^- + OH^-$ in alkaline conditions[62,63]. The significance of this pathway lies in the fact that it preserves the monocarbon framework while selectively converting a highly

oxidized, thermodynamically stable molecule into an energy-bearing liquid product without requiring the deeper deoxygenation steps associated with CO, hydrocarbons, or alcohols. The underlying chemical problem is therefore not merely reduction of $CO_2$, but selective control over the first productive branch of carbon-centered proton-coupled electron transfer. Because linear $CO_2$ possesses a closed-shell electronic structure and a high degree of C=O bond stabilization, its activation at an electrode interface necessarily involves interfacial polarization, bending of the molecular geometry, and redistribution of charge into antibonding orbitals. Once this activation occurs, the reaction network can diverge into chemically different pathways depending on how the carbon center and oxygen atoms are differentially stabilized[64-66]. A two-electron route toward HCOOH or $HCOO^-$ requires the catalytic interface to favor a formate-type reduction logic in which hydrogen addition and electron transfer are directed toward generating a partially reduced carbon-oxygen framework rather than promoting a carboxyl-type intermediate that evolves toward CO formation. In this sense, carbon dioxide-related two-electron electrocatalysis is governed by a fundamental issue of chemoselective oxygen retention. The catalyst must enable reduction of carbon without driving excessive C-O bond weakening, and it must permit release of the oxygen-containing product before further reduction or competing hydrogen evolution consumes the available interfacial reducing equivalents. This places the two-electron $CO_2$ pathway in a chemically delicate position. If activation is too weak, the substrate remains kinetically inert because the first electron-transfer event to $CO_2$ is intrinsically demanding. If activation is too strong or too reducing, the system may be diverted toward CO-producing or more deeply reduced pathways, thereby losing control over the oxidation-state-defined endpoint[67-69]. Carbon dioxide-related two-electron electrocatalysis is therefore best understood as a selective partial reduction problem in which the central objective is not maximal electron delivery to carbon, but controlled accumulation of two reducing equivalents in a manner that preserves oxygen functionality and defines product identity at the earliest chemically useful stage of $CO_2$ conversion. Precisely for this reason, this reaction class occupies a special place in the broader landscape of two-electron electrocatalysis. It demonstrates that selective redox synthesis is not always a matter of breaking stronger bonds or reaching more reduced products, but can instead depend on recognizing partial reduction itself as the desired chemical outcome and on constructing an interfacial reaction environment that stabilizes that outcome against both underactivation and overreduction[70,71].

### *Nitrogen-oxoanion two-electron electrocatalysis*

Nitrogen-oxoanion two-electron electrocatalysis introduces a further level of chemical complexity because the target transformation is no longer defined primarily by O-O bond retention or partial carbon reduction, but by the selective deoxygenation of an already oxidized nitrogen center without allowing the system to descend into extensive hydrogenation or complete reduction. Its most representative expression is the two-electron reduction of nitrate to nitrite, which can be written in acidic medium as $NO_3^- + 2H^+ + 2e^- \rightarrow NO_2^- + H_2O$ and in alkaline conditions as $NO_3^- + H_2O + 2e^- \rightarrow NO_2^- + 2OH^-$[72].

This reaction class is chemically significant because it occupies the first decisive reduction threshold in the broader electrochemical nitrogen redox network. At this stage, the oxidation state of nitrogen is lowered while the nitrogen-oxo framework remains intact, so the reaction does not yet enter the more deeply reduced manifolds associated with $NH_3$, $N_2$, hydroxylamine, or other downstream nitrogen species. The essential feature of this chemistry is therefore selective oxygen-atom removal under conditions where the substrate remains highly susceptible to further proton-coupled electron transfer[73-75]. Unlike $CO_2$ reduction, where the central challenge is selective protonation of an activated carbon-oxygen framework, or oxygen electrocatalysis, where the principal issue is preservation or formation of an O-O unit; nitrogen-oxoanion chemistry is governed by the controlled editing of N-O bonding within a multistate reduction ladder. This ladder is intrinsically dense because nitrate, nitrite, NO, $N_2O$, $NH_2OH$, $NH_3$, and $N_2$ are all chemically accessible nodes connected by interfacial proton-electron transfer, oxygen abstraction, and nitrogen-centered

bond reorganization. As a consequence, the two-electron pathway to nitrite is rarely an isolated event. It is the first chemically defined branch point at which the catalytic interface either releases a partially reduced oxyanion or continues to drive the system into deeper nitrogen reduction chemistry. Nitrogen-oxoanion two-electron electrocatalysis is thus best understood as a problem of selective decoupling between initial activation and subsequent overreduction. The catalyst must promote sufficient interaction with nitrate to weaken one N-O bond and allow oxygen removal, yet it must not stabilize the resulting reduced nitrogen species so strongly that additional protonation, deoxygenation, or hydrogenation becomes unavoidable. This requirement gives the two-electron nitrate-to-nitrite route a conceptually important status within selective electrosynthesis[76]. It reveals how control over redox depth can be exerted not by maximizing reduction power, but by defining a chemically precise stopping point within a cascade of energetically accessible nitrogen transformations. It also distinguishes nitrogen-oxoanion electrocatalysis from many other inorganic redox processes, because the two-electron product is not simply a useful chemical target but also a mechanistically critical discriminator of pathway logic. Once nitrite is released as the dominant product, the catalytic system demonstrates an ability to recognize partial deoxygenation as a terminal outcome. Once nitrite remains adsorbed or is further activated *in situ*, the chemistry rapidly transitions from selective two-electron conversion to multielectron nitrogen reduction. In this sense, nitrogen-oxoanion two-electron electrocatalysis offers an especially revealing framework for understanding how electrode interfaces govern the balance between controlled oxyanion editing and uncontrolled descent into more reduced nitrogen states, thereby extending the broader concept of two-electron electrocatalysis into a chemically richer domain of valence-state management, oxygen transfer selectivity, and nitrogen-centered reaction-network control[77,78].

### *Halide two-electron electrocatalysis*

Halide two-electron electrocatalysis defines an anodic class of selective redox chemistry in which the central task is the controlled oxidation of halide anions to molecular halogens through a discrete two-electron process, most commonly represented by $2Cl^- \rightarrow Cl_2 + 2e^-$, $2Br^- \rightarrow Br_2 + 2e^-$, or $2I^- \rightarrow I_2 + 2e^-$. In chemical terms, this class differs fundamentally from the preceding oxygen-, carbon-, and nitrogen-centered systems because the target transformation is not a partial reduction of a highly oxidized substrate, but a selective oxidation in which an anionic main-group species is converted into a covalently bonded neutral molecule. Its conceptual significance within two-electron electrocatalysis arises from the fact that electron count directly determines whether the anodic interface performs productive halogen evolution or diverts oxidative equivalents into oxygen-centered pathways arising from $H_2O$ or $OH^-$ activation[79]. The key issue is therefore not simply halide oxidation itself, since halides are in many cases readily oxidizable, but the ability of the electrochemical interface to discriminate between halogen-forming redox chemistry and competing oxygen evolution under strongly anodic conditions. This makes halide electrocatalysis an especially revealing case of selective charge allocation at positive potentials. The catalyst must promote interfacial electron withdrawal from $X^-$ to generate a surface-associated halide-derived oxidized state, yet it must also channel that oxidizing power toward X-X bond formation and halogen release rather than toward the buildup of oxygenated surface species that ultimately lead to $O_2$ evolution. In this sense, halide two-electron electrocatalysis is governed by a distinctive coupling between anion adsorption, outer- or inner-sphere oxidation character, and bimolecular or surface-mediated bond formation between halogen equivalents. Its mechanistic identity therefore depends on whether the anodic interface recognizes halide oxidation as a self-contained molecular synthesis pathway or merely treats halide as a spectator in a broader oxygen evolution environment. This distinction is chemically consequential because halogen evolution represents a selective oxidation-state transition with clear product definition, whereas oxygen evolution corresponds to redirection of current into a fundamentally different redox manifold[80]. Halide two-electron electrocatalysis also occupies an important position in the general theory of competing pathways because it illustrates that two-electron selectivity is not restricted to partial reduction chemistry. It can also emerge in oxidation processes where the desired

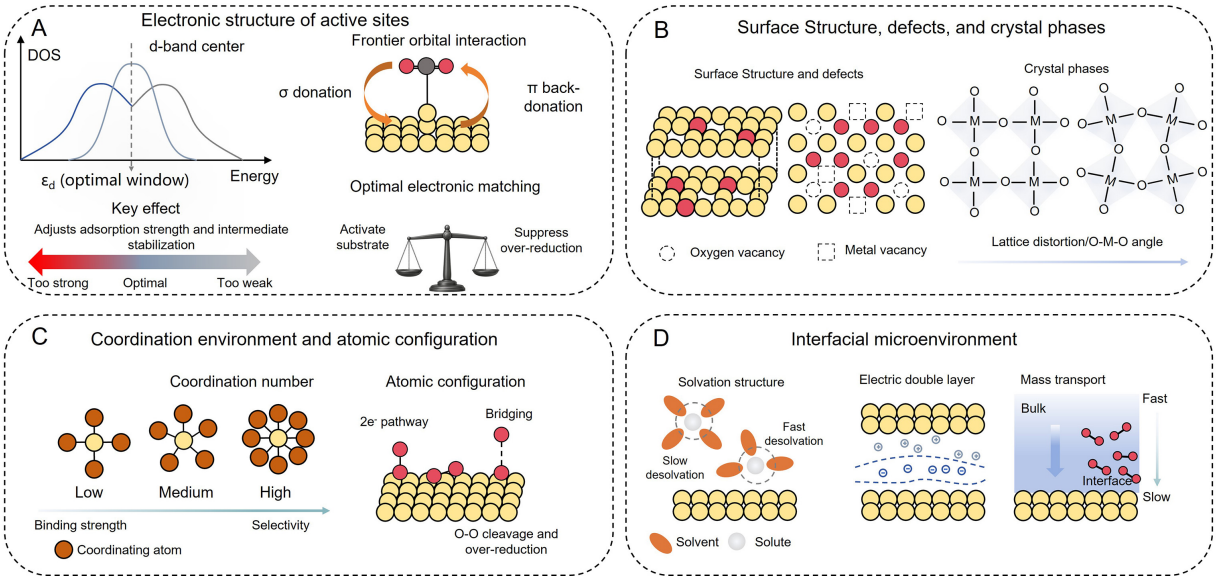



**Figure 4.** Schematic overview of structural regulation strategies and microenvironmental engineering for selective two-electron electrocatalysis. (A) Electronic structure of active sites, highlighting the d-band center, frontier orbital interactions, and the optimal electronic matching window to balance substrate activation and suppress over-reduction. (B) Surface structure and defects, including oxygen vacancies and metal vacancies, as well as crystal phases characterized by lattice distortion and O-M-O angles. (C) Coordination environment and atomic configuration, showing the impact of coordination number on binding strength and selectivity, alongside typical 2e⁻ pathways. (D) Interfacial microenvironment, covering solvation structure, electric double layer properties, and mass transport dynamics between the bulk solution and the interface.

outcome requires arrest at a lower oxidative depth than the surrounding anodic environment would otherwise favor. The reaction thus exemplifies a general principle of two-electron electrocatalysis: the relevant selectivity problem is determined not by the absolute ease of electron transfer, but by whether the interface can stabilize the chemically intended redox channel long enough for product-defining bond formation and desorption to occur[81,82]. In halide systems, that intended channel is molecular halogen generation. Once the interface instead accumulates oxygenated intermediates from solvent or hydroxide oxidation, the chemistry shifts away from selective halide conversion and into the multielectron oxygen evolution regime[83]. Halide two-electron electrocatalysis therefore provides a chemically clean and conceptually important model for understanding how anodic interfaces partition oxidizing equivalents between substrate-centered molecular formation and solvent-derived overoxidation, thereby extending the broader framework of two-electron electrocatalysis to include oxidation-state precision on the oxidative side of inorganic electrosynthesis.

## Structural determinants of two-electron selectivity

The structural origin of two-electron selectivity can be understood most clearly by separating the problem into four interconnected yet chemically distinguishable levels of control [Figure 4]. At the most fundamental level, active-site electronic structure determines how the catalytic center redistributes charge, interacts with frontier orbitals of adsorbates, and stabilizes key redox states along a two-electron pathway[84,85]. That electronic behavior is then concretized by the local coordination environment and atomic configuration, which define the geometric and chemical identity of the reactive center and thereby shape the mode of substrate binding and elementary-step accessibility. Beyond the immediate active site, surface structure, defect chemistry, and crystal phase further regulate adsorption topology, surface redox flexibility, and the energetic landscape of intermediate transformation[86]. Finally, these intrinsic structural features operate within an interfacial microenvironment in which solvation, proton activity, ionic organization, and local electric fields modulate the actual expression of catalytic selectivity under electrochemical conditions. Considered together, these four categories provide a hierarchical framework for understanding how two-electron pathways are chemically encoded, from the electronic nature of the catalytic center to the interfacial environment in which selective redox conversion ultimately occurs[87,88].

### *Electronic structure of active sites*

The electronic structure of active sites constitutes the most fundamental determinant of two-electron selectivity because it defines how the catalytic center exchanges charge with the reacting substrate, how strongly key intermediates are stabilized, and whether the interfacial redox process terminates at a partially transformed state or continues into deeper reaction manifolds. In chemical terms, two-electron electrocatalysis is governed by the need to place the active site within a narrow electronic window. The site must be sufficiently electron-rich or electronically polarizable to activate a relatively inert molecule such as $O_2$, $CO_2$, or $NO_3^-$, yet it must not stabilize the resulting adsorbate-derived states so strongly that subsequent bond cleavage, excessive protonation, or further electron accumulation becomes unavoidable. This requirement makes two-electron selectivity highly sensitive to the frontier-orbital interaction between the catalyst and the adsorbate[89-91]. The energy, symmetry, and occupancy of valence orbitals at the active site determine the extent of σ donation, π back-donation, and charge redistribution during adsorption, which in turn dictates whether an intermediate is bound in a configuration compatible with release at the two-electron level or with progression toward multielectron conversion. For transition-metal-centered sites, this behavior is closely associated with the position of the d-band manifold, the degree of orbital degeneracy or splitting under the local ligand field, and the oxidation-state flexibility of the metal center during proton-coupled electron transfer[92,93]. A more electronically elevated and weakly filled d manifold can facilitate initial substrate activation by enhancing overlap with antibonding orbitals of the adsorbate, whereas a more stabilized and lower-lying manifold may weaken excessive covalent interaction and favor desorption of a partially reduced or oxidized product. The decisive issue is therefore not strong binding in a generic sense, but electronically discriminating binding that stabilizes the desired precursor state without overstabilizing the states that lead to further transformation. An optimized electronic structure should balance substrate activation and intermediate release rather than simply maximize adsorption strength. Appropriate orbital interactions facilitate substrate activation, whereas excessively strong interactions can hinder desorption and promote deeper redox pathways. Conversely, weak interactions may suppress substrate activation. Thus, electronic-structure regulation should establish an appropriate adsorption-desorption balance to promote the desired two-electron transformation while preventing further conversion[94]. This principle becomes especially important in reactions where two-electron and multielectron pathways diverge only after the first adsorbed intermediate has formed. Under such conditions, small changes in charge density, spin state, covalency, or metal-ligand electronic coupling can shift the relative energy ordering of surface intermediates and thereby redirect the reaction network. Electronic structure also determines the redox noninnocence of the active center itself. In some catalysts, charge transfer during catalysis is borne predominantly by the metal site, whereas in others substantial electron density is delocalized onto ligands, lattice anions, or electronically coupled neighboring atoms[95,96]. Such differences are chemically consequential because they alter whether the active site behaves as a localized redox center, a covalent adsorption platform, or a more distributed electronic ensemble capable of buffering charge without excessively deepening the reduction or oxidation state of the bound species. From this perspective, two-electron selectivity can be viewed as a problem of electronic-state matching between catalyst and reaction intermediate. When this matching is appropriate, the active site lowers the barrier for the first chemically productive step while preserving a thermodynamic and kinetic bias toward product release at the two-electron stage. When the matching becomes too strong, the interface begins to favor bond scission, overprotonation, or continued electron transfer, thereby collapsing selectivity into deeper pathways[97-99]. Electronic structure is thus not merely one descriptor among many. It is the primary chemical variable that governs how the active site interprets the redox identity of the substrate and decides whether a two-electron state is treated as a target product or as a transient species en route to further conversion.

### *Coordination environment and atomic configuration*

Beyond the intrinsic electronic character of the active center, two-electron selectivity is critically shaped by the coordination environment and atomic configuration that define how that center is spatially and chemically expressed at the catalytic interface. This level of control is distinct because it concerns not simply how many electrons are available for substrate interaction, but how the reactive atom is embedded, constrained, and exposed to the approaching molecule. The coordination number, the identity of neighboring atoms, the symmetry of the local ligand field, and the nuclearity of the active ensemble together determine whether the catalytic site presents a highly localized adsorption motif, a cooperative multiatom platform, or a geometrically frustrated environment in which partial transformation is favored over complete redox conversion[100]. In two-electron electrocatalysis, this distinction is especially important because the difference between selective termination and overconversion often emerges from subtle changes in binding geometry rather than from large differences in overall adsorption strength. A coordinatively unsaturated site may facilitate initial substrate capture by increasing orbital accessibility and local electrophilicity, yet the same site can also promote excessive activation if it allows multidentate binding or bond dissociation geometries that open deeper pathways. Conversely, a more saturated or symmetry-constrained coordination environment may attenuate full bond cleavage while still permitting the end-on or weakly asymmetric adsorption modes that are compatible with two-electron product formation and release[101,102]. Atomic configuration further refines this behavior by determining whether catalysis occurs at an isolated atom, a pair of adjacent heterometallic or homometallic centers, a cluster-like ensemble, or an extended surface motif. These configurations are not electronically equivalent, but their significance in the present context is fundamentally geometric and chemical. An isolated site often limits the configurational space available for adsorbate reorganization, thereby suppressing pathways that require bridging adsorption, multi-center bond scission, or sequential deep reduction at neighboring atoms. By contrast, binuclear or ensemble sites can either enhance two-electron selectivity through controlled cooperativity or undermine it by enabling excessive intermediate stabilization and further transformation. The decisive question is whether the local atomic arrangement imposes a reaction geometry that favors partial redox editing while disfavoring the reorganizations required for multielectron descent. This is why coordination environment and atomic configuration are best regarded as structural filters of selectivity. They determine the orientation of substrate approach, the multiplicity of accessible adsorption states, the degree of bond polarization induced upon binding, and the probability that the first product-like intermediate will remain terminal or become a precursor to deeper chemistry. Their role is also chemically significant because they mediate the balance between rigidity and adaptability at the active site. An overly rigid coordination framework may prevent the substrate from reaching the transition-state geometry needed for productive two-electron conversion, whereas an overly flexible environment may accommodate multiple downstream configurations and thereby erode selectivity. The most effective coordination motifs are therefore those that combine sufficient structural definition to restrict undesirable pathways with sufficient local lability to permit the specific geometric distortion associated with the desired two-electron event. In this sense, two-electron electrocatalysis depends not only on what the active site is electronically, but also on how it is built atom by atom. Coordination environment and atomic configuration determine whether catalytic reactivity is localized, cooperative, constrained, or overextended, and they thereby translate structural chemistry into a concrete decision about whether a substrate will be released after a two-electron transformation or driven onward into a deeper reaction manifold[103].

### *Surface structure, defects, and crystal phases*

Two-electron selectivity is further governed by the extended structural state of the catalyst surface, because the same chemically defined active site can exhibit markedly different reaction behavior once it is embedded within different surface terminations, defect populations, and crystallographic phases. This level of control operates beyond local coordination in a narrower sense and concerns the broader structural context that

determines how adsorption motifs are distributed, how surface atoms relax under bias, and how reactive intermediates migrate, reorganize, or couple during turnover[104]. Surface structure is central in this regard because crystallographic orientation and atomic termination define the spatial arrangement, density, and connectivity of adsorption sites available to the substrate[105-107]. Recent studies on electrochemical $CO_2$ reduction further demonstrate that phase and facet engineering can regulate catalytic selectivity by modifying surface atomic arrangements, coordination environments, defect structures, and interfacial strain, thereby altering the adsorption behavior and energetic barriers of key intermediates[108]. A close-packed terrace, a stepped edge, and a kink-rich surface may expose nominally similar elemental compositions, yet they impose fundamentally different adsorption geometries and bond polarization environments. For two-electron electrocatalysis, this distinction is crucial because selective partial conversion often requires a surface that permits the first productive adsorption event but disfavors the ensemble geometries needed for deeper bond cleavage, excessive hydrogenation, or prolonged intermediate retention. Defects introduce a further layer of chemical complexity. Vacancies, antisite disorder, lattice distortion, dislocations, and undercoordinated surface motifs can alter local charge density, redistribute frontier states, and create chemically nonuniform adsorption microdomains in which intermediate-state energetics deviate substantially from those of the ideal lattice[109-111]. This defect-mediated electronic regulation is also evident in graphene-derived quantum dots, where edge and structural defects introduce surface states and modulate electron density and heterogeneous electron-transfer behavior, demonstrating that defect-induced electronic perturbations can directly influence electrochemical reactivity[112]. Such perturbations may be beneficial when they lower the barrier for substrate activation or tune the adsorption state into the narrow window required for two-electron termination, but they may also undermine selectivity if they generate highly reactive sites that capture intermediates too strongly and facilitate continued transformation. Defect and phase engineering should therefore be treated as structure-dependent strategies rather than universally beneficial approaches. Appropriate defects and stable phases can promote the desired two-electron pathway, whereas excessive defects or unstable phases may overstabilize intermediates and promote deeper multielectron conversion. Effective regulation therefore requires balancing reaction activation with intermediate release. The role of defects is therefore not reducible to a general enhancement of activity. Their true significance lies in whether they selectively stabilize the product-forming branch without opening additional pathways that consume the partially transformed species[113]. Crystal phase exerts a similarly profound influence because phase identity determines not only long-range atomic ordering but also metal-anion covalency, bond ionicity, lattice flexibility, and redox adaptability under electrochemical conditions[114-116]. Even when composition remains constant, distinct polymorphs can present different surface energies, different capacities for structural relaxation, and different propensities for forming metastable adsorbate-bound states during catalysis. These differences matter acutely in two-electron systems, where a modest shift in the surface free-energy landscape can determine whether a reaction terminates at peroxide, formate, nitrite, or halogen, or instead proceeds toward deeper reduction or oxidation[117]. Surface structure, defects, and crystal phase also share a common mechanistic consequence in that they regulate how far the catalyst departs from its idealized static configuration during operation. Two-electron electrocatalysis often depends on maintaining a surface state that is reactive but not overadaptive. If the surface is too inert, the first electron-transfer event remains difficult and selectivity is lost through underactivation. If the surface is too labile, restructuring under bias may generate highly active motifs that favor multielectron chemistry or transform the original catalyst into a different reactive phase altogether[118]. The relevant structural question is therefore not simply which surface or phase is intrinsically most active, but which one preserves an adsorption and transformation landscape compatible with controlled arrest at the two-electron level. In this sense, surface structure, defect chemistry, and crystal phase function collectively as mesoscale regulators of selectivity[119]. They translate bulk structural chemistry into the real interfacial topology encountered by reacting molecules and determine whether the catalyst surface behaves as a platform for selective partial redox conversion or as a continuously evolving environment that drives the system beyond the intended two-electron endpoint[120,121].

### *Interfacial microenvironment effects*

Even when the active-site electronic structure and the catalyst lattice are held constant, two-electron selectivity can still change profoundly because the electrochemical reaction is expressed not in vacuum but within a dynamically organized interfacial microenvironment. This microenvironment constitutes the final level at which selectivity is determined, since it governs how reactants, intermediates, protons, solvent molecules, counterions, and electric fields are arranged at the moment of electron transfer. Its importance in two-electron electrocatalysis is especially pronounced because partial redox conversion is intrinsically sensitive to whether a newly formed intermediate remains solvated and releasable or is immediately driven into further transformation. In chemical terms, the interfacial microenvironment controls this balance through four tightly coupled effects. The first is local proton activity, which determines not only proton availability for proton-coupled electron transfer but also the protonation state and chemical identity of the product itself[122]. A nominally identical electron-transfer sequence can therefore terminate in chemically different forms depending on whether the interface favors $H_2O_2$ or $HO_2^-$, HCOOH or $HCOO^-$, and whether partially reduced nitrogen-oxo species are rapidly protonated or remain in less reactive oxyanion forms[123]. The second is solvation structure and hydrogen-bond organization, because the orientation and mobility of interfacial water molecules influence charge stabilization, transition-state polarity, and the desorption tendency of polar oxygenated or oxyanion intermediates. A hydrogen-bond network that stabilizes a released two-electron product in the outer coordination environment can favor selective termination, whereas a more weakly accommodating solvent structure may leave the product vulnerable to readsorption or continued surface reaction. The third is the ionic environment and double-layer organization, including the identity, concentration, and spatial distribution of cations and anions near the electrode[124-126]. These species reshape the local electric field, alter electrostatic screening, and selectively stabilize charged or polarizable intermediates through noncovalent interactions. Such effects are chemically consequential because two-electron and multielectron pathways often diverge only after a charged intermediate has formed, so even modest changes in interfacial field strength or ion pairing can shift the relative accessibility of partial versus deep redox conversion. These interfacial factors are closely coupled through the electric double layer, which governs the local distribution of ions, solvent molecules, and electric fields. Changes in proton activity, electrolyte composition, and solvation can reshape the electric double layer, thereby affecting charge transfer, intermediate stabilization, and proton-coupled electron transfer. Thus, interfacial regulation should be viewed as coordinated control of the electric double layer, solvation, and transport processes, which collectively determine two-electron selectivity[127]. The fourth is mass-transport-defined concentration polarization, which determines how rapidly substrate is replenished, how efficiently product is removed, and whether local accumulation of reactants or products perturbs the reaction network away from its intended two-electron endpoint. This factor is not merely hydrodynamic in a physical sense. It has direct chemical implications because local buildup of $H_2O_2$, $HO_2^-$, halogen species, or partially reduced nitrogen intermediates can change secondary reaction probability, alter interfacial acidity, or induce competitive pathways that are absent under dilute boundary conditions[128]. Interfacial microenvironment effects are therefore best understood as the operational chemical context in which intrinsic catalyst structure is translated into actual selectivity[129-131]. They determine whether the catalyst experiences the substrate as a neutral molecule, an ion-paired complex, a strongly polarized adsorbate precursor, or a species embedded within a proton-rich or proton-deficient solvent cage. They also define whether the two-electron product leaves the interface as a chemically stabilized molecular entity or remains trapped within a reactive interfacial zone that promotes further oxidation or reduction. In this sense, two-electron electrocatalysis cannot be explained solely by the structure of the solid catalyst. It must also be understood through the structure of the liquid-side interface, where proton distribution, solvation fields, ionic organization, and local concentration gradients collectively decide whether a partially transformed state survives as the desired product or is consumed as a transient intermediate on the way to deeper redox chemistry.

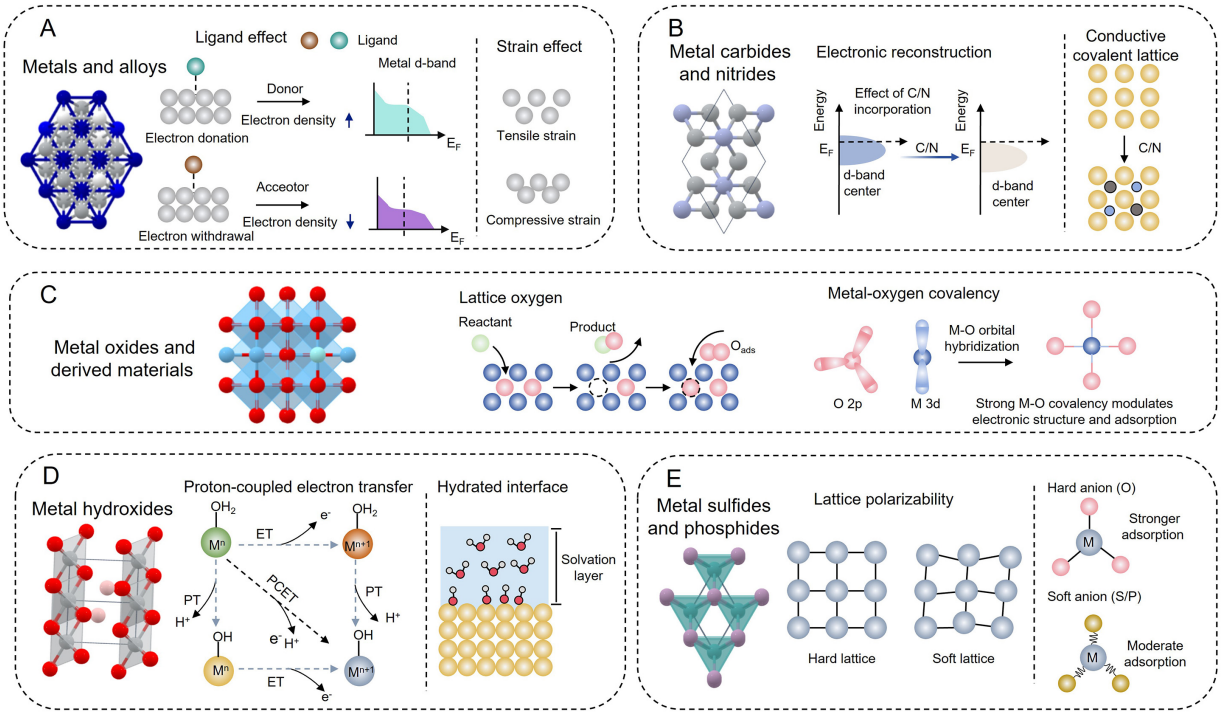



**Figure 5.** Schematic overview of representative catalyst materials and structure-performance relationships for two-electron electrocatalysis. (A) Metals and alloys, illustrating the ligand effect and strain effect on the metal d-band. (B) Metal carbides and nitrides, showing electronic reconstruction via C/N incorporation and the formation of a conductive covalent lattice. (C) Metal oxides and derived materials, highlighting the role of lattice oxygen and metal-oxygen covalency. (D) Metal hydroxides, depicting proton-coupled electron transfer mechanisms and the hydrated interfacial solvation layer. (E) Metal sulfides and phosphides, emphasizing lattice polarizability and the impact of anion type on adsorption strength.

## Classes of electrocatalysts for two-electron reactions

The catalyst landscape of two-electron electrocatalysis can be most usefully interpreted by grouping materials according to the chemical nature of the catalytically dominant phase, since different classes impose fundamentally different modes of charge transfer, adsorbate binding, lattice participation, and interfacial redox flexibility [Figure 5]. Such a classification is not merely taxonomic. It provides a chemically grounded framework for understanding how catalyst composition and bonding characteristics influence the ability of an interface to terminate reactivity at the two-electron level rather than proceed toward deeper oxidation or reduction pathways[132]. Metals and alloys offer electronically tunable surfaces with well-defined adsorption energetics, whereas metal oxides and oxide-derived materials introduce more pronounced metal-oxygen covalency and lattice-mediated redox behavior. Metal hydroxides further emphasize proton-coupled interfacial chemistry under hydrated conditions, while metal sulfides and phosphides provide more polarizable anion frameworks that can reshape substrate activation and intermediate stabilization. Metal carbides and nitrides bring yet another regime in which covalent-metallic bonding and non-oxide lattice chemistry alter the balance between activity and selective termination[133-135]. Beyond these established families, other emerging catalytic materials expand the structural and electronic design space through unconventional coordination environments, hybrid architectures, and chemically heterogeneous interfaces[136-138]. Considered together, these classes capture the principal material platforms through which two-electron electrocatalysis has been explored, and they offer a practical basis for comparing how different catalytic chemistries encode selectivity across otherwise diverse reaction systems.

### *Metals and alloys*

Metals and alloys constitute one of the most foundational catalyst classes in two-electron electrocatalysis because they provide electronically coherent surfaces on which adsorption, charge transfer, and bond

activation can be regulated with comparatively high chemical precision. Their importance arises first from the fact that metallic bonding creates delocalized electronic states capable of mediating rapid interfacial electron exchange, while at the same time permitting continuous variation in adsorbate binding strength through changes in elemental identity, surface composition, and alloy structure[139]. This combination is particularly relevant to two-electron chemistry, where the central requirement is not maximal substrate activation but selective stabilization of an intermediate state that is reactive enough to form and yet labile enough to desorb before deeper conversion occurs. In pure metals, this balance is often governed by the intrinsic position and filling of valence states, especially for transition-metal surfaces where adsorption of oxygenated, carbon-containing, or nitrogen-oxo intermediates depends sensitively on metal-adsorbate orbital overlap[140-142]. A metal surface that binds reaction intermediates too weakly may fail to induce the first chemically productive step, whereas one that binds too strongly can prolong surface residence, facilitate bond scission, or promote additional proton-coupled electron transfer beyond the intended two-electron endpoint. The chemical role of metals in this context is therefore best understood as providing a continuous adsorption-energy platform from which selective partial conversion can be achieved only within a narrow reactivity window. Noble metals are often prominent in this regard because their relatively moderate affinity for oxygenated intermediates can favor molecular release over overreduction, while post-transition metals may promote oxygen-retaining carbon reduction pathways by stabilizing particular adsorption geometries associated with partial reduction rather than deep deoxygenation. The mechanistic significance of metallic catalysts thus lies in their ability to translate band-structure-defined adsorption into oxidation-state-specific product formation, making them especially suitable for reactions in which the distinction between two-electron and multielectron pathways is controlled by subtle changes in surface bonding rather than by wholesale changes in catalytic composition.

Alloying extends this chemistry into a much broader regime of selective control by introducing compositional heterogeneity, altered surface atom distributions, and modified electronic coupling between constituent elements. Its value in two-electron electrocatalysis does not lie simply in averaging the properties of two metals, but in generating new catalytic states through ligand, strain, and ensemble effects that are inaccessible to monometallic surfaces. Through ligand effects, one component can perturb the electron density and orbital energy of another, thereby tuning the binding strength and transformation pathway of key intermediates without necessarily changing the overall metallic character of the surface[143]. Through strain effects, lattice mismatch can alter bond lengths and orbital overlap, shifting the energetic balance between intermediate formation and further conversion[144]. Through ensemble effects, alloying can dilute contiguous active atoms, isolate reactive motifs, or create heteroatomic neighborhoods that favor one adsorption geometry over another. These consequences are chemically decisive for two-electron pathways because deeper redox chemistry often requires multi-atom cooperation, stronger adsorption ensembles, or more extensive intermediate stabilization than selective partial conversion. Alloy surfaces can therefore suppress overreaction either by electronically weakening undesired states or by geometrically interrupting the site architectures needed for continued transformation. At the same time, they may preserve sufficient reactivity to promote the first substrate-activation event, which is essential for avoiding the opposite failure mode of underactivation[144,145]. This makes alloys particularly powerful as catalysts for two-electron electrocatalysis, since they allow the reaction coordinate to be reshaped at both the electronic and atomic scales without abandoning the efficient interfacial charge-transfer properties of metallic systems. From a broader materials-chemistry perspective, metals and alloys thus serve as a canonical platform for understanding selective electrocatalysis in its most controlled form. They show how continuous tuning of surface electronic structure, atomic distribution, and cooperative adsorption behavior can convert a highly reactive metallic interface from a driver of deep redox conversion into a chemically disciplined surface that recognizes the two-electron state as the preferred catalytic endpoint[146].

In non-noble and low-noble alloy systems, alloying first manifests as a strategy for regulating the electronic structure of active metal sites and the adsorption mode of reaction intermediates. Liu *et al*.[147] first pointed out that Bi in BiNi alloys can regulate Ni sites through a dual-isolation effect involving both physical and electronic isolation. At the electronic-structure level, the three-dimensional charge-density distribution of BiNi alloys shows that Bi incorporation reshapes the local electronic environment around Ni and provides a basis for tuning *OOH adsorption [Figure 6A]. Structurally, the High-resolution transmission electron microscopy (HR-TEM) image of BiNi/C, together with the inset diffractogram, further confirms the formation of the crystalline BiNi alloy phase [Figure 6B]. On this basis, the OOH-adsorbed configurations and free-energy diagrams of Bi, Ni, BiNi-Bi, and BiNi-Ni sites at 0.7 V *vs*. Reversible hydrogen electrode (RHE) suggest that alloyed BiNi sites can optimize *OOH adsorption and conversion [Figure 6C]. At the kinetic level, the Tafel slopes of Ni/C, Bi/C, and BiNi/C show that BiNi/C displays faster ORR kinetics than the corresponding monometallic counterparts [Figure 6D][147]. In parallel, Du *et al*.[148] focused on a PdCu bimetallic system and showed that Cu incorporation can promote the formation of Pd-O species, thereby enhancing the $2e^-$ ORR activity of Pd sites. To clarify the adsorption configuration, the computational model of OOH adsorption on an oxygen-containing PdCu surface describes the interaction between the oxygen intermediate and the alloy surface through Pd, Cu, and O atoms [Figure 6E]. Then, the HR-TEM image of PdCu nanowires, with the inset selected-area electron diffraction (SAED) pattern, confirms their crystalline structure [Figure 6F]. From the thermodynamic perspective, the calculated free-energy diagrams for the $2e^-$ ORR over bare PdCu and oxygen-containing PdCu surfaces indicate that surface oxygen species optimize the energetics related to $H_2O_2$ formation [Figure 6G]. Finally, the correlation between the $H_2O_2$ selectivity of PdCu NWs/C and the normalized Raman intensity of Pd-O suggests that reaction-induced Pd-O species are closely associated with improved $H_2O_2$ selectivity [Figure 6H][148]. Taken together, these two studies demonstrate that performance enhancement in non-noble or low-noble alloy catalysts does not arise from composition change alone, but from the synergistic optimization of *OOH adsorption and the $2e^-$ ORR pathway through electronic regulation, active-site isolation, and stabilization of surface oxygen species.

In noble-metal alloy systems, Zhang *et al*.[149] further demonstrated that Pd-Hg-based pure metallic aerogels can construct single-atom-like Pd sites by suppressing Pd-Pd coordination, while Au doping further tunes the electronic structure of Pd sites without substantially changing their geometric environment. Specifically, the OOH-adsorption-induced charge-density difference of Au-$Pd_2Hg_5$ (001) shows electron accumulation and depletion around the adsorption region, indicating that Au doping modifies the electronic interaction between Pd sites and oxygenated intermediates [Figure 6I]. Meanwhile, the HR-TEM image of M-$Pd_2Hg_5$ aerogels confirms that the crystalline alloy aerogel framework is retained after heterometal doping [Figure 6J]. In terms of reaction energetics, the calculated reaction-coordinate diagrams of $Pd_2Hg_5$ and Au-$Pd_2Hg_5$ for the $2e^-$ ORR show that Au-$Pd_2Hg_5$ follows a pathway closer to ideal $H_2O_2$ formation [Figure 6K]. Consistently, the linear sweep voltammetry (LSV) curves and $H_2O_2$ currents detected on the Pt ring electrode demonstrate the enhanced $H_2O_2$-generation response of Au-$Pd_2Hg_5$ relative to $Pd_2Hg_5$ [Figure 6L][149]. Extending this site-isolation concept, Lin *et al*.[150] developed Pd@M-in-Au core-shell nanocrystals with dilute binary alloy surfaces, using an inert Au matrix to isolate Pt, Pd, or Rh active atoms and thereby regulate OOH adsorption configurations and ORR selectivity. First, the prepared Pd@$Pt_{0.05}Au_{0.95}$ core-shell nanocube and its {100}-related Pt-in-Au alloy surface present the structural basis for isolating Pt atoms within the Au matrix [Figure 6M]. Subsequently, the high-angle annular dark-field scanning transmission electron microscopy (HAADF-STEM) image of Pd@$Pt_{0.05}Au_{0.95}$-6L core-shell nanocubes verifies their ordered core-shell structure [Figure 6N]. To reveal the role of Pt aggregation, the ΔGOOH values of Pt aggregates with different sizes embedded in the Au matrix show that the Pt aggregation state and *OOH adsorption configuration strongly affect *OOH binding [Figure 6O]. Finally, rotating ring-disk electrode (RRDE)

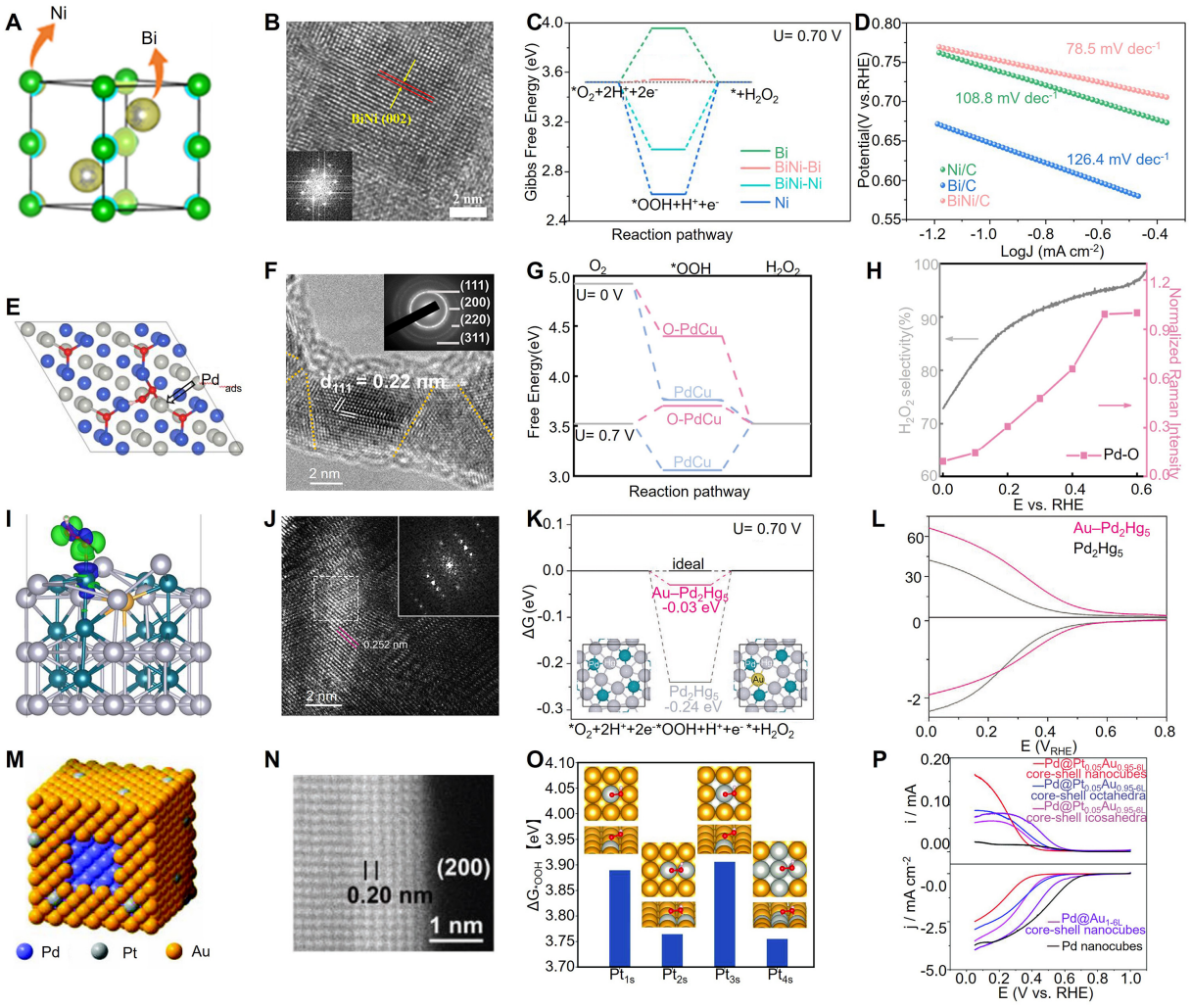



**Figure 6.** (A) Three-dimensional charge-density diagrams of the BiNi alloys. (B) HR-TEM image of BiNi/C, with the corresponding diffractogram shown in the inset. (C) OOH adsorption configurations on Bi, Ni, BiNi-Bi, and BiNi-Ni sites, and the corresponding free-energy diagrams at 0.7 V *vs.* RHE. (D) Tafel slopes of Ni/C, Bi/C, and BiNi/C samples. (A-D) is reprinted with permission from Ref.[147]. Copyright © 2025 American Chemical Society. (E) Computational model of the OOH adsorption configuration on an oxygen-containing PdCu surface. Silver, blue, and red spheres represent Pd, Cu, and O atoms, respectively. (F) HR-TEM image of PdCu nanowires, with the SAED pattern shown in the inset. (G) Calculated free-energy diagrams for the 2e$^-$ ORR over bare PdCu and oxygen-containing PdCu. (H) $H_2O_2$ selectivity of the PdCu NWs/C ORR catalyst and normalized Raman intensities of Pd-O. (E-H) is reprinted with permission from Ref.[148]. Copyright © 2023 American Chemical Society. (I) Charge-density difference of Au-$Pd_2Hg_5$ (001) induced by OOH adsorption. Green and blue regions represent electron accumulation and depletion, respectively; the isosurface value is 0.004 e Å$^{-3}$. (J) HR-TEM image of the heterometal-doped M-$Pd_2Hg_5$ aerogel. (K) Calculated reaction-coordinate diagrams for $Pd_2Hg_5$ and Au-$Pd_2Hg_5$ aerogels, with insets showing the corresponding atomic configurations. This model represents the (100) plane of the $Pd_2Hg_5$ structure. (L) LSV curves of $Pd_2Hg_5$ and Au-$Pd_2Hg_5$ aerogels in $O_2$-saturated 0.1 M $HClO_4$ at a rotation speed of 1,600 rpm and a scan rate of 20 mV s$^{-1}$, together with the detected $H_2O_2$ currents on the Pt ring electrode at a fixed potential of 1.2 V *vs.* RHE. (I-L) is reprinted with permission from Ref.[149]. Copyright © 2023 Wiley-VCH GmbH. (M) Structural illustration of the obtained Pd@$Pt_{0.05}Au_{0.95}$ core-shell nanocube covered by facets and the corresponding Pt-in-Au square atomic arrangement. (N) HAADF-STEM image of Pd@$Pt_{0.05}Au_{0.95}$-6L core-shell nanocubes. (O) ΔG*OOH values for Pd@Pt-in-Au (100) surfaces with Pt aggregates of different sizes embedded in the Au matrix. In Ptnx, n and x denote the number of Pt atoms and the *OOH adsorption arrangement, respectively, where e and s refer to end-on and side-on adsorption. (P) Electrocatalytic ORR performance of Pd@M-in-Au core-shell nanocrystals measured by RRDE in $O_2$-saturated 0.1 M $HClO_4$, where M = Pt, Pd, and Rh. The upper panel shows ring-current polarization curves, and the lower panel shows disk-current-density polarization curves. (M-P) is reprinted with permission from Ref.[150]. Copyright © 2024 Wiley-VCH GmbH.

measurements of Pd@M-in-Au core-shell nanocrystals in $O_2$-saturated 0.1 M $HClO_4$ demonstrate that Pd@Pt-in-Au nanocubes exhibit a more favorable $H_2O_2$-related current response, with the upper ring current reflecting $H_2O_2$ generation and the lower disk current density representing overall ORR activity [Figure 6P][150].

### *Metal oxides and derived materials*

Metal oxides and oxide-derived materials occupy a chemically distinctive position in two-electron electrocatalysis because their catalytic behavior is governed not only by metal-centered adsorption chemistry, but also by the participation of oxygen-containing lattices that can redistribute charge, reorganize local bonding, and stabilize polar intermediates in ways that are fundamentally different from purely metallic surfaces[119,151]. This distinction is especially important for two-electron pathways, where selective termination often depends on the ability of the interface to support partial redox transformation without triggering deeper bond cleavage or further proton-coupled electron transfer. In oxides, such control arises from the coupled influence of metal oxidation state, metal-oxygen covalency, lattice ionicity, and surface hydroxylation. A metal center embedded in an oxide lattice is not exposed as an electronically isolated atom. It exists within a chemically constrained M-O framework that shapes the distribution of charge density between cationic and anionic sublattices and therefore alters how reactants are polarized upon adsorption. This framework frequently favors more directional and chemically differentiated interactions with oxygenated or oxyanion intermediates, which can be advantageous for two-electron processes because it allows selective stabilization of a product-forming intermediate without necessarily promoting the strong multidentate adsorption modes associated with deeper conversion. At the same time, the oxide lattice can influence catalysis through its capacity for local redox adjustment. Changes in cation valence, transient accumulation of oxygen vacancies, and partial rehybridization of surface metal-oxygen bonds under applied potential can all reshape the energetic landscape of intermediate formation and release[152-154]. The essential advantage of metal oxides in this context is therefore not simply that they are polar materials, but that they provide a chemically adaptive yet structurally defined environment in which redox chemistry can be modulated through both cation-centered and lattice-mediated effects. Such behavior is particularly relevant when two-electron selectivity depends on preserving oxygen functionality, stabilizing partially reduced carbon-oxygen species, or preventing overreduction of nitrogen-oxo intermediates[155,156]. In these cases, the oxide surface often acts less as an inert support for electron transfer and more as a chemically active matrix that controls how far a substrate can descend along the redox coordinate before product release becomes favored.

This framework becomes even more interesting in oxide-derived materials, especially oxyhydroxide-type surfaces generated through hydration, electrochemical activation, or near-surface reconstruction, because the introduction of hydroxyl groups transforms the catalyst from a predominantly lattice-controlled oxide into an interface where metal-oxygen-hydrogen connectivity becomes an intrinsic part of the catalytic state. In chemical terms, this means that the active surface is no longer defined solely by M-O linkages, but by dynamic M-OH and M-O(H)-M motifs capable of mediating proton transfer, hydrogen-bond-assisted adsorption, and local acid-base buffering at the reaction interface. Such features are highly consequential for two-electron electrocatalysis, since selective partial conversion often requires careful synchronization between electron transfer and proton delivery[157,158]. Oxyhydroxide-derived surfaces can lower the barrier for the first productive proton-coupled electron transfer event by providing a more hydrated and proton-responsive environment, while at the same time altering the desorption behavior of polar intermediates through hydrogen-bond interactions and surface hydroxyl exchange. Their catalytic role is therefore not reducible to that of a simple modified oxide[159-161]. Rather, they introduce a different chemical regime in which the lattice and the interfacial proton network become more strongly coupled. This coupling can favor two-electron selectivity when it supports controlled substrate activation and selective stabilization of partially transformed states, yet it can also undermine selectivity if excessive proton responsiveness promotes continued hydrogenation or deeper oxidation. The decisive issue is whether the oxyhydroxide-like surface maintains a balanced reactivity in which hydroxyl-assisted adsorption and proton transfer remain sufficiently discriminating to terminate catalysis at the desired two-electron level. From a broader structural-chemical perspective, metal oxides and oxide-derived materials therefore exemplify a catalyst class in which

selective electrocatalysis emerges from the interplay of cation electronic structure, lattice oxygen chemistry, and surface hydroxyl reactivity[162]. Their importance in two-electron systems lies precisely in this multidimensional control, because they demonstrate how a chemically complex inorganic framework can encode selectivity not through a single descriptor, but through the integrated behavior of redox-active metal centers, oxygen-containing lattices, and proton-responsive surface structures[163].

Metal oxides and oxide-derived materials are important platforms for two-electron electrocatalysis because their metal-oxygen coordination, surface facets, oxygen defects, and heterointerfaces can regulate oxygen-intermediate adsorption and reaction selectivity. In Fe-based oxide systems, Yin *et al.*[164] reported crystalline nitrogen-doped-carbon-anchored $Fe_3O_4$ nanoparticles for neutral $H_2O_2$ electrosynthesis. The charge density difference for $O_2$ adsorbed on $Fe_3O_4$(220)-nitrogen-doped carbon with vacancy (CNV) first presents the interfacial electronic redistribution between $Fe_3O_4$ and nitrogen-defective carbon, providing a theoretical basis for understanding oxygen activation at the oxide-carbon interface [Figure 7A]. The high-resolution transmission electron microscopy (HRTEM) image of $Fe_3O_4$@TNC then shows the crystalline oxide structure and its contact with the carbon matrix, supporting the structural basis of the proposed interfacial active sites [Figure 7B]. After the structural and electronic features are established, the free-energy profiles at U = 0.7 V reveal the thermodynamic preference of the $Fe_3O_4$(220)-CNV interface for the two-electron reduction of $O_2$ to $H_2O_2$ [Figure 7C]. The capacitance current densities measured at 1.0 V give a higher double-layer capacitance for $Fe_3O_4$TNC (11.1 mF $cm^{-2}$) than for $Fe_3O_4$@TNC-AE (6.7 mF $cm^{-2}$) and TNC (4.6 mF $cm^{-2}$), supporting its larger electrochemically accessible surface area [Figure 7D][164]. From charge redistribution, crystalline structure, capacitance response, and reaction free energy, this work illustrates how $Fe_3O_4$@TNC regulates neutral two-electron oxygen reduction reaction through oxide-carbon interfacial coupling. In $SnO_2$-based systems, Hu *et al.*[165] designed Zn/$SnO_2$ for paired two-electron electrosynthesis. The optimized adsorption configuration of the *OCHO intermediate on the Zn-Sn(101) alloy surface first describes the interaction between the key $CO_2$-reduction intermediate and the Zn-Sn site [Figure 7E]. TEM images of Zn/$SnO_2$ at different magnifications, together with the corresponding SAED pattern, then present the nanoscale morphology and crystalline features of the catalyst [Figure 7F]. The calculated reaction energy profiles for water oxidation on the Zn site of Zn/$SnO_2$ further describe the energetic pathway associated with $H_2O_2$ formation [Figure 7G]. Finally, the Faradaic efficiency of formate ($FE_{HCOO^-}$) over bare $SnO_2$ and Zn/$SnO_2$ compares their formate-generation behavior, demonstrating the influence of Zn incorporation on the $CO_2$ reduction process [Figure 7H][165].

The role of oxide-derived interfaces is further reflected in ZnO@$ZnO_2$ and layered Bi-based oxyhalides. Zhou *et al.*[166] identified ZnO@$ZnO_2$ as an oxide-derived interface for neutral two-electron oxygen reduction reaction. The adsorption model of $O_2$ molecules on ZnO@$ZnO_2$ first shows the interaction between $O_2$ and the ZnO/$ZnO_2$ surface, where red and gray spheres represent O and Zn atoms, respectively [Figure 7I]. HRTEM images of ZnO treated with 0.4 mol $L^{-1}$ $H_2O_2$ then present the structural features of the peroxide-treated ZnO surface, providing microscopic evidence for the oxide/peroxide-related interface [Figure 7J]. On this structural basis, the LSV curves measured in 0.1 M $K_2SO_4$ show the electrochemical oxygen-reduction responses of ZnO, ZnO@$ZnO_2$, and $ZnO_2$, with the ring currents displayed in the upper panel and the disk current densities displayed in the lower panel [Figure 7K]. The corresponding calculated electron transfer number and $H_2O_2$ selectivity in 0.1 M $K_2SO_4$ further evaluate the two-electron reaction pathway, with the bottom panel showing electron transfer number and the upper panel showing $H_2O_2$ selectivity [Figure 7L][166]. This set of results forms a continuous logic from $O_2$ adsorption, interface formation, electrochemical response, and pathway evaluation. In defect-engineered oxide systems, Deng *et al.*[167] reported oxygen-vacancy-rich $In_2O_{3-x}$ for electrocatalytic $H_2O_2$ production. The image of the final obtained $In_2O_{3-x}$ catalyst first presents the oxide material produced after the synthetic process, providing a direct visual representation of the prepared catalyst [Figure 7M]. The AC-TEM images of $In_2O_{3-x}$ then reveal its crystalline lattice structure

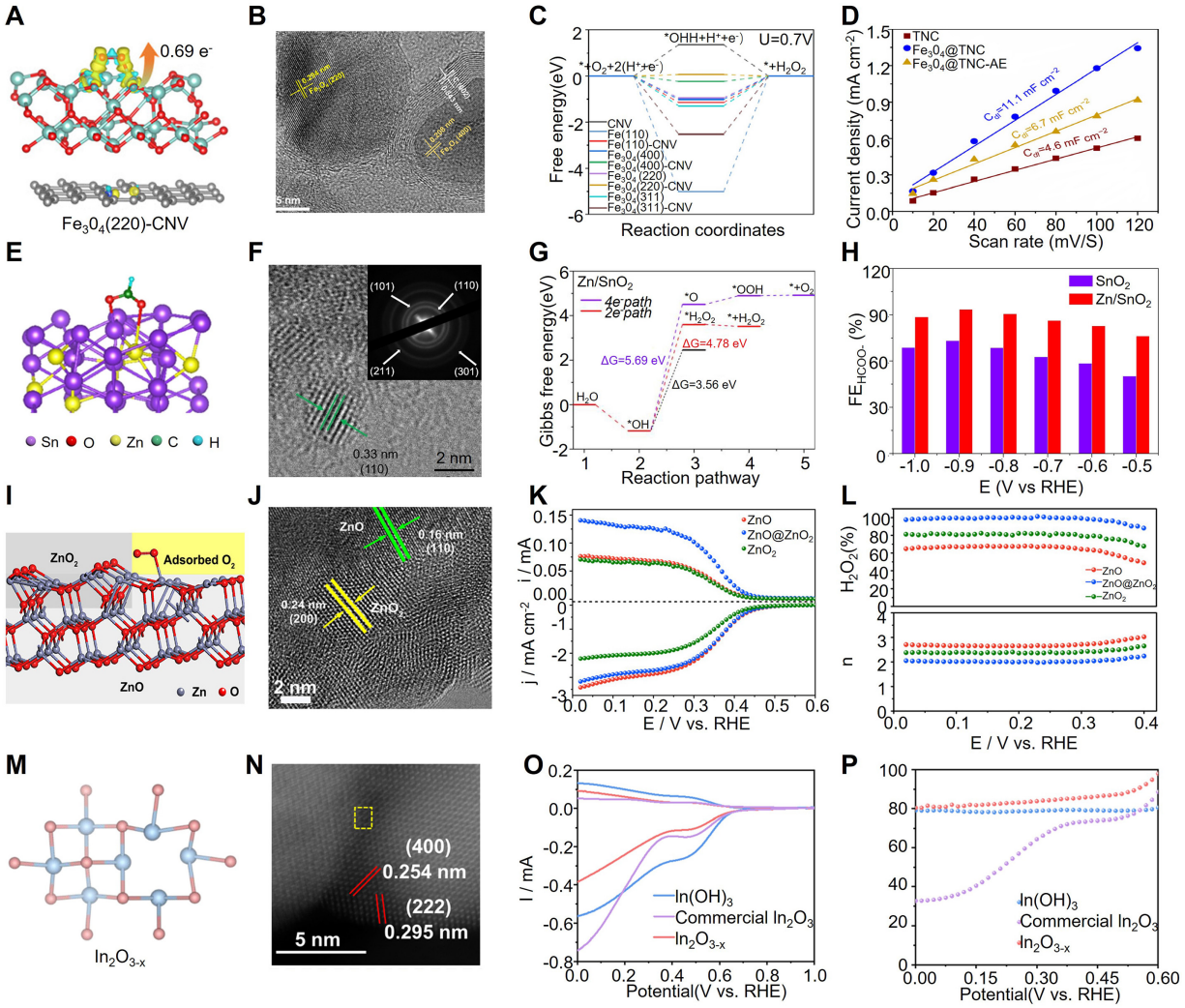



**Figure 7.** (A) Charge density difference for $O_2$ adsorbed on $Fe_3O_4$(220)-CNV. (B) HRTEM image of $Fe_3O_4$@TNC. (C) Free energy diagram at U = 0.7 V for the reduction of $O_2$ to $H_2O_2$. (D) Capacitance current densities measured at 1.0 V using 40 mF $cm^{-2}$ as the specific capacitance standard. (A-D) is reprinted with permission from Ref.[164]. Copyright © 2025 The Royal Society of Chemistry. (E) Optimized adsorption configuration of the *OCHO intermediate on the Zn-Sn (101) alloy surface. (F) TEM images of Zn/$SnO_2$ at different magnifications; the inset is the corresponding SAED pattern. (G) Calculated reaction energy profiles for water oxidation on the Zn site of Zn/$SnO_2$. (H) Faradaic efficiency of formate ($FE_{HCOO-}$) over bare $SnO_2$ and Zn/$SnO_2$. (E-H) is reprinted with permission from Ref.[165]. Copyright © 2023 Wiley-VCH GmbH. (I) Adsorption model of $O_2$ molecules on ZnO@$ZnO_2$; red and gray spheres represent O and Zn atoms, respectively. (J) HRTEM image of ZnO treated with 0.4 mol $L^{-1}$ $H_2O_2$. (K) LSV curves of ZnO, ZnO@$ZnO_2$, and $ZnO_2$ measured in 0.1 M $K_2SO_4$, with ring currents in the upper part and disk current densities in the lower part. (L) Calculated electron transfer number and $H_2O_2$ selectivity in 0.1 M $K_2SO_4$; the bottom panel shows electron transfer number and the upper panel shows $H_2O_2$ selectivity. (I-L) is reprinted with permission from Ref.[166]. Copyright © 2023 The Royal Society of Chemistry. (M) Image of the final obtained $In_2O_{3-x}$ catalyst. (N) AC-TEM images of $In_2O_{3-x}$. (O) LSV curves of RRDE measurement at 5 mV $s^{-1}$ and 1,600 rpm in $O_2$-saturated 0.1 M KOH. (P) Calculated $H_2O_2$ selectivity of $In_2O_{3-x}$. (M-P) is reprinted with permission from Ref.[167]. Copyright © 2024 The Royal Society of Chemistry.

and provide microscopic evidence for the formed oxide catalyst [Figure 7N]. Subsequently, the RRDE LSV curves measured at 5 mV $s^{-1}$ and 1,600 rpm in $O_2$-saturated 0.1 M KOH record the oxygen-reduction response of $In_2O_{3-x}$ and reference samples [Figure 7O]. Finally, the calculated $H_2O_2$ selectivity further demonstrates that $In_2O_{3-x}$ favors the two-electron ORR pathway for $H_2O_2$ production [Figure 7P][167].

### *Metal hydroxides*

Metal hydroxides represent a chemically distinctive catalyst class in two-electron electrocatalysis because their reactive surfaces are intrinsically built from hydrated metal-oxygen coordination units in which hydroxyl ligands are not merely spectators but constitutive elements of the catalytic state. This gives metal hydroxides a mode of reactivity that differs in an essential way from both metallic surfaces and more lattice-rigid oxides. The catalytic interface is defined by M-OH connectivity, variable hydrogen-bond organization, and a high degree of proton responsiveness, so the surface can regulate substrate activation through coupled electron-transfer and acid-base processes rather than through adsorption energetics alone. Such characteristics are especially relevant to two-electron pathways, where selective termination frequently depends on whether the first partially transformed intermediate can be stabilized and released without being driven into further protonation, deoxygenation, or oxidation. In hydroxide frameworks, this control arises from several interrelated chemical features[168]. First, the hydroxylated coordination sphere can create a strongly polarized and hydrated local environment that facilitates interaction with polar substrates and oxygen-containing intermediates while preserving a degree of reversibility in surface binding. Second, proton mobility within hydrogen-bonded surface hydroxyl networks can lower the barrier for elementary proton-coupled electron transfer steps, thereby making partially transformed redox states kinetically accessible under milder driving force. Third, the metal center in a hydroxide is often electronically modulated by the σ-donating and hydrogen-bond-active character of surrounding OH ligands, which affects the balance between substrate activation and product release in a manner not captured by dry-lattice descriptors alone[169,170]. This is chemically important because two-electron selectivity is often lost when the interface either underactivates the substrate or overstabilizes the intermediate state. Metal hydroxides can occupy an intermediate regime in which the surface is sufficiently reactive to initiate conversion yet sufficiently hydrated and proton-buffered to favor controlled arrest at the desired redox level. Their layered or partially disordered structures may further contribute by enabling local reorganization of hydrogen-bond geometry and metal coordination during turnover without requiring the extensive lattice rearrangements that often accompany deeper redox chemistry. The decisive advantage of metal hydroxides, therefore, lies in their ability to couple structural hydration, proton transfer, and coordination flexibility into a single catalytic environment. This makes them especially valuable as platforms for two-electron electrocatalysis, because they illustrate how selective inorganic redox conversion can be regulated not only by the electronic identity of the metal center, but also by the chemical behavior of a hydroxyl-rich surface that mediates when electrons and protons are delivered, how long intermediates remain interfacially trapped, and whether the catalytic sequence terminates at a discrete two-electron product rather than progressing into a more extensive reaction manifold.

Metal hydroxides and hydroxide-derived materials are important platforms for two-electron electrocatalysis because their hydrated metal-oxygen coordination can regulate water activation, proton transfer, and oxygen-intermediate adsorption. In Ni-based hydroxide systems, Nie *et al*.[171] designed $Ni(OH)_2$/carbon nanotube (CNT) for $H_2O_2$ electrosynthesis in chloride-containing electrolytes. The geometries of $Ni(OH)_2$ first present the atomic arrangement of the hydroxide structure, providing a structural basis for understanding the Ni-O-H coordination environment [Figure 8A]. The TEM image of $Ni(OH)_2$/CNT then shows the morphology of the hydroxide/carbon composite; under high resolution, the lattice fringes with a planar spacing of 0.236 nm can be assigned to the (101) facet of $Ni(OH)_2$ [Figure 8B]. Based on this structure, the wavelet transform (WT) analysis of the Ni $K^3$-weighted extended X-ray absorption fine structure (EXAFS) signals further records the local Ni coordination feature in $Ni(OH)_2$/CNT [Figure 8C]. The LSV polarization curves of $Ni(OH)_2$/CNT in NaCl solutions with different concentrations and the Faradaic efficiency in 1 M NaCl then evaluate its electrocatalytic response and peroxide-generation behavior under saline conditions [Figure 8D][171]. This sequence from hydroxide geometry, lattice structure, local coordination, and saline-electrolyte performance shows how $Ni(OH)_2$/CNT connects hydroxide active sites with two-electron electrocatalysis in chloride-containing media. In another Ni hydroxide-derived system,

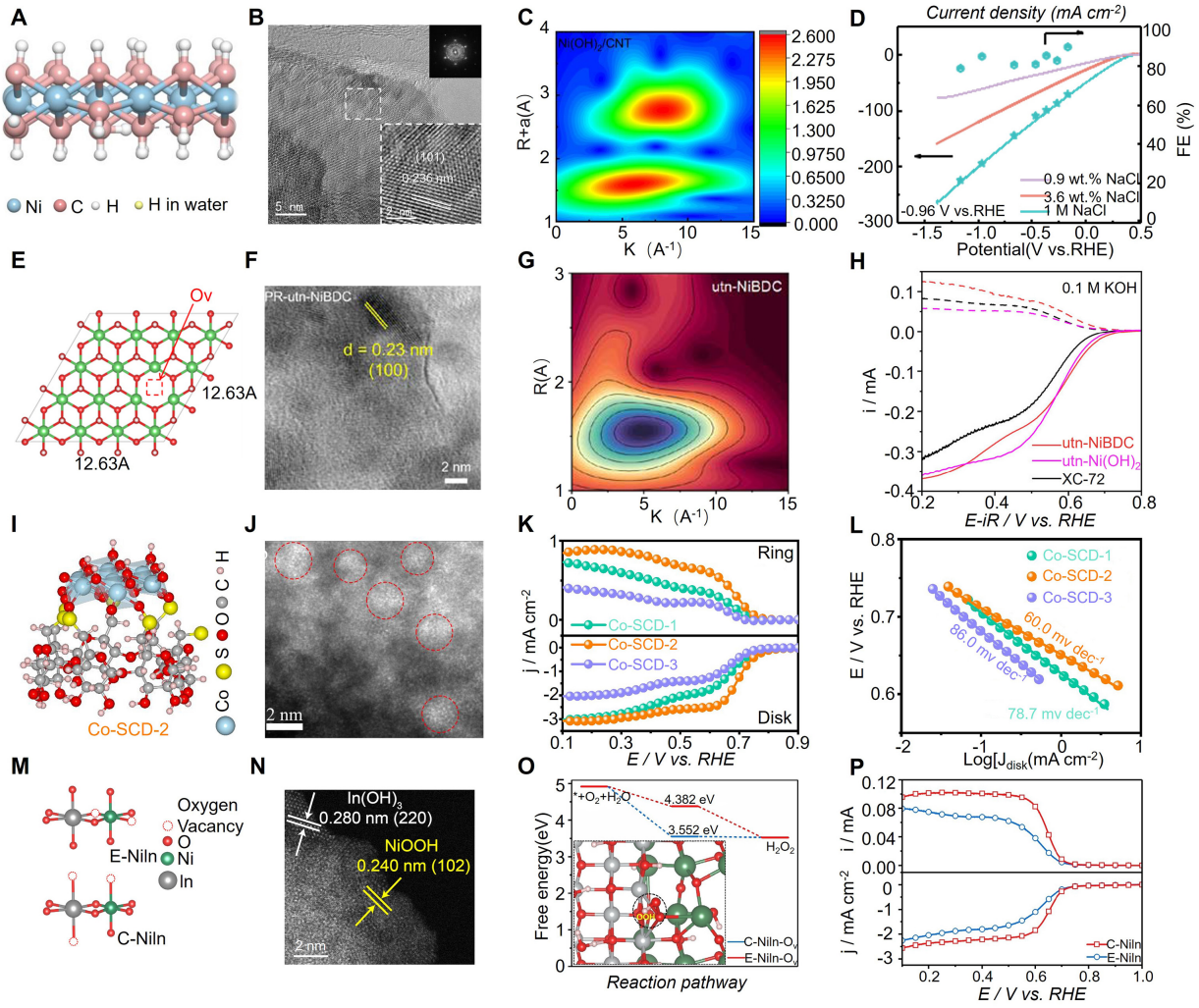



**Figure 8.** (A) Geometries of $Ni(OH)_2$; blue, pink, and white spheres represent Ni, O, and H atoms, respectively. (B) TEM image of $Ni(OH)_2$/CNT; under high resolution, the lattice fringes show a planar spacing of 0.236 nm, which can be ascribed to the (101) facet of $Ni(OH)_2$. (C) WT of the Ni $K^3$-weighted EXAFS signals of $Ni(OH)_2$/CNT. (D) LSV polarization curves of $Ni(OH)_2$/CNT in NaCl solutions with different concentrations and Faradaic efficiency of $Ni(OH)_2$/CNT in 1 M NaCl. (A-D) is reprinted with permission from Ref.[171]. Copyright © 2025 Springer Nature. (E) Top view of BDC ligand-functionalized $Ni(OH)_2$; pink, red and green spheres represent H, O and Ni atoms, respectively. (F) HRTEM image of PR-utn-NiBDC. (G) WT of the $k^3$-weighted Ni K-edge EXAFS signals of utn-NiBDC. (H) Polarization curves of utn-NiBDC, utn-$Ni(OH)_2$, and XC-72 recorded at 1,600 rpm and a scan rate of 5 mV $s^{-1}$, together with the detected $HO_2^-$ currents on the ring electrode at a fixed potential of 1.2 V *vs.* RHE. (E-H) is reprinted with permission from Ref.[172]. Copyright © 2025 Springer Nature. (I) Co-SCD-2 models; azure, yellow, red, gray, and light pink spheres represent Co, S, O, C, and H atoms, respectively. (J) HAADF-STEM image of Co-SCD-2 after the test. (K) LSV polarization curves of Co-SCD-1, Co-SCD-2, and Co-SCD-3. (L) Tafel slope curves of Co-SCD-1, Co-SCD-2, and Co-SCD-3. (I-L) is reprinted with permission from Ref.[173]. Copyright © 2023 Wiley-VCH GmbH. (M) Schematic illustration of deficient $[NiO_6]$-$[InO_6]$ motifs of NiOOH/$In(OH)_3$ heterostructures for E-NiIn and C-NiIn. (N) High-resolution STEM image. (O) Free-energy diagram for the two-electron oxygen reduction reaction on C-NiIn-Ov and E-NiIn-Ov at U = 0 V; inset: configuration of HOO* adsorbed on E-NiIn. (P) Oxygen reduction reaction LSV curves of E-NiIn and C-NiIn measured by RRDE. (M-P) is reprinted with permission from Ref.[174]. Copyright © 2024 Wiley-VCH GmbH.

Zhang *et al.*[172] investigated 1,4-Benzenedicarboxylate (BDC) ligand-functionalized $Ni(OH)_2$ derived from ultrathin NiBDC. The top view of BDC-functionalized $Ni(OH)_2$ presents the local ligand-modified hydroxide structure [Figure 8E]. The HRTEM image of PR-utn-NiBDC then records the reconstructed nanosheet structure and lattice information [Figure 8F]. The WT of the $k^3$-weighted Ni K-edge EXAFS signals of utn-NiBDC further describes the local coordination state of Ni after ligand-related structural regulation [Figure 8G]. Finally, the polarization curves of utn-NiBDC, utn-$Ni(OH)_2$, and XC-72, together with the detected $HO_2^-$ currents on the ring electrode at a fixed potential of 1.2 V *vs.* RHE, compare their oxygen-reduction behavior and peroxide-generation response under RRDE conditions [Figure 8H][172].

Hydroxide chemistry can also be extended to Co hydroxide clusters and reconstructed heterometallic oxyhydroxide interfaces. Qi *et al.*[173] reported Co-SCD-2 as a Co hydroxide cluster system for two-electron oxygen reduction reaction. The Co-SCD-2 model first presents the local cluster configuration of the Co-based catalytic structure [Figure 8I]. The HAADF-STEM image of Co-SCD-2 after the test then provides structural information on the Co-containing species after electrochemical operation [Figure 8J]. On this basis, the LSV polarization curves of Co-SCD-1, Co-SCD-2, and Co-SCD-3 compare their oxygen-reduction responses [Figure 8K]. The corresponding Tafel slope curves further evaluate the kinetic differences among these Co-SCD catalysts [Figure 8L][173]. This progression from cluster model, post-test structural characterization, polarization behavior, and kinetic comparison illustrates how Co hydroxide cluster structures can be related to two-electron oxygen reduction reaction activity. In reconstructed heterometallic systems, Yu *et al.*[174] studied NiOOH/$In(OH)_3$ heterostructures derived from Ni-In precatalysts. The schematic illustration of deficient [$NiO_6$]-[$InO_6$] motifs compares the interfacial structures of E-NiIn and C-NiIn, providing a model for understanding oxygen-vacancy-related Ni-In coordination [Figure 8M]. The high-resolution STEM image then records the local atomic structure of the reconstructed heterostructure [Figure 8N]. The free-energy diagram for the two-electron oxygen reduction reaction on C-NiIn-Ov and E-NiIn-Ov at U = 0 V further compares the reaction energetics, with the inset showing the configuration of HOO* adsorbed on E-NiIn [Figure 8O]. Finally, the oxygen reduction reaction LSV curves of E-NiIn and C-NiIn measured by RRDE record their disk-current responses, while the ring-current behavior is used to evaluate peroxide-related reaction performance [Figure 8P][174].

### *Metal sulfides and phosphides*

Metal sulfides and phosphides constitute an important non-oxide catalyst family for two-electron electrocatalysis because they introduce a fundamentally different anion chemistry into the catalytic interface, thereby reshaping how charge is distributed, how substrates are polarized, and how partially transformed intermediates are stabilized during turnover. In contrast to oxides and hydroxides, where oxygen-based ligands strongly influence ionicity, proton responsiveness, and lattice redox behavior, sulfides and phosphides are built from softer and more polarizable anionic frameworks[175]. This chemical distinction has profound consequences for two-electron selectivity. Sulfur and phosphorus generally form bonds with transition metals that are less ionic and often more covalent than metal-oxygen linkages, which modifies the electronic density around the metal center and changes the nature of adsorbate interaction from the outset[176]. A more polarizable lattice can facilitate substrate activation by allowing flexible charge redistribution during adsorption, yet it may also weaken the overly rigid stabilization of oxygenated or oxyanion intermediates that often drives overconversion on more strongly binding surfaces. For two-electron processes, this balance is highly advantageous because selective partial conversion typically requires a catalyst that can induce the first productive electron-transfer event without locking the product-forming intermediate into an excessively deep surface-bound state[177]. In this sense, sulfides and phosphides frequently operate as chemically intermediate platforms between metallic and oxide-like behavior. They retain sufficient electronic conductivity and redox accessibility to support efficient interfacial charge transfer, while their non-oxide lattice chemistry imposes a distinct adsorption environment that can favor controlled redox termination over complete reduction or oxidation. Their catalytic significance is therefore not simply that they are alternative compounds of familiar metals, but that the presence of S or P changes the entire bonding logic of the interface, from the polarity of the active site to the degree of covalency involved in intermediate stabilization and release[178].

This altered bonding logic becomes even more consequential when considering the structural and mechanistic flexibility of sulfide and phosphide surfaces under electrochemical conditions. The metal center in these materials is embedded within an anion framework that can respond to bias, solvation, and local redox demand in ways that differ substantially from oxygen-based lattices. Sulfur- and

phosphorus-containing environments can modify the electron density and oxidation-state adaptability of the catalytic metal, but they also introduce a surface chemistry in which ligand softness, local coordination asymmetry, and partial surface reconstruction may selectively reshape the free-energy landscape of partial redox conversion[179]. This is especially relevant in two-electron electrocatalysis, where deeper pathways often require prolonged retention of an intermediate, stronger bond cleavage capability, or a more highly oxidizing or reducing local state than that needed for selective product release. Sulfides and phosphides can suppress these undesired trajectories either by attenuating the adsorption strength of overreactive intermediates or by favoring adsorption geometries that are compatible with product formation but less favorable for continued transformation[180,181]. At the same time, their surfaces are often chemically less static than idealized bulk structures suggest. Under operation, local sulfur or phosphorus environments may reorganize, partially oxidize, or become heterogeneously solvated, generating catalytically relevant interfaces that are best understood as dynamic chalcogenide- or phosphide-derived states rather than purely stoichiometric solids. The value of this class in two-electron electrocatalysis lies precisely in that dynamic balance. The interface can remain electronically competent for substrate activation while avoiding the strongly oxygen-affine or excessively rigid binding environments that frequently push reactions toward multielectron manifolds. From a broader materials-chemistry perspective, metal sulfides and phosphides therefore expand the design space of two-electron electrocatalysis by demonstrating how non-oxide inorganic frameworks can encode selective redox behavior through softer anion fields, more covalent metal-anion interactions, and structurally adaptive surfaces that favor controlled arrest at chemically defined two-electron endpoints[182,183].

Metal sulfides and phosphides are important material systems in two-electron electrocatalysis because metal-S and metal-P bonding can regulate the electronic structure of metal centers and influence oxygen-intermediate adsorption. In sulfide-based systems, Zhang *et al.*[184] reported exfoliated $NiPS_3$ nanosheets for $H_2O_2$ electrosynthesis from seawater. The energetically optimized structure of $NiPS_3$ first presents the stable atomic configuration of the layered metal phosphorus trisulfide framework, providing a theoretical structural basis for understanding the catalytic environment of Ni sites [Figure 9A]. The high-resolution TEM image of $NiPS_3$ then shows clear lattice information of the nanosheet structure, confirming the crystallinity of the sulfide catalyst [Figure 9B]. At the local coordination level, the EXAFS-related analysis shows two major peaks located at 2.52 and 3.47 A, which are attributed to the scattering of Ni-S and Ni-P paths, respectively, consistent with the Ni K-edge WT-EXAFS observations [Figure 9C]. In terms of catalytic kinetics, the Tafel plots compare $FePS_3$, $CoPS_3$, $NiPS_3$, $ZnPS_3$, NiS, and $NiPSe_3$, showing the kinetic differences among metal phosphorus sulfides and related sulfide catalysts [Figure 9D][184]. Through the progression from optimized structure, high-resolution lattice characterization, local coordination analysis, and kinetic comparison, these results indicate that the Ni-S/Ni-P coordination environment of $NiPS_3$ is closely associated with its two-electron oxygen reduction reaction behavior. Che *et al.*[185] further used CdS as another sulfide model and introduced carbon-shell engineering. The final structural model of $C_{0.01}$@CdS nanorods presents the structural configuration of carbon-coated CdS nanorods, showing the composite structure in which the carbon layer covers the CdS nanorod surface [Figure 9E]. The HRTEM image of $C_{0.01}$@CdS nanorods then confirms the retained crystalline structure after carbon coating [Figure 9F]. Based on this structure, the charge-density difference of C@CdS samples further describes the interfacial electronic redistribution between CdS and the carbon shell [Figure 9G]. Finally, the $H_2O_2$ yield of pure CdS and C@CdS nanorods compares their peroxide-production performance [Figure 9H][185].

In phosphide and ligand-regulated sulfide systems, Kim *et al.*[186] synthesized facet-controlled MoP single crystals and investigated their catalytic behavior in two-electron oxygen reduction reaction for $H_2O_2$ production. The *OOH-adsorbed MoP (1010) phosphorus-terminated pillar surface first presents the adsorption configuration of the key oxygen intermediate on a specific phosphide facet, providing a structural basis for understanding facet-dependent catalytic behavior [Figure 9I]. The high-resolution TEM image of

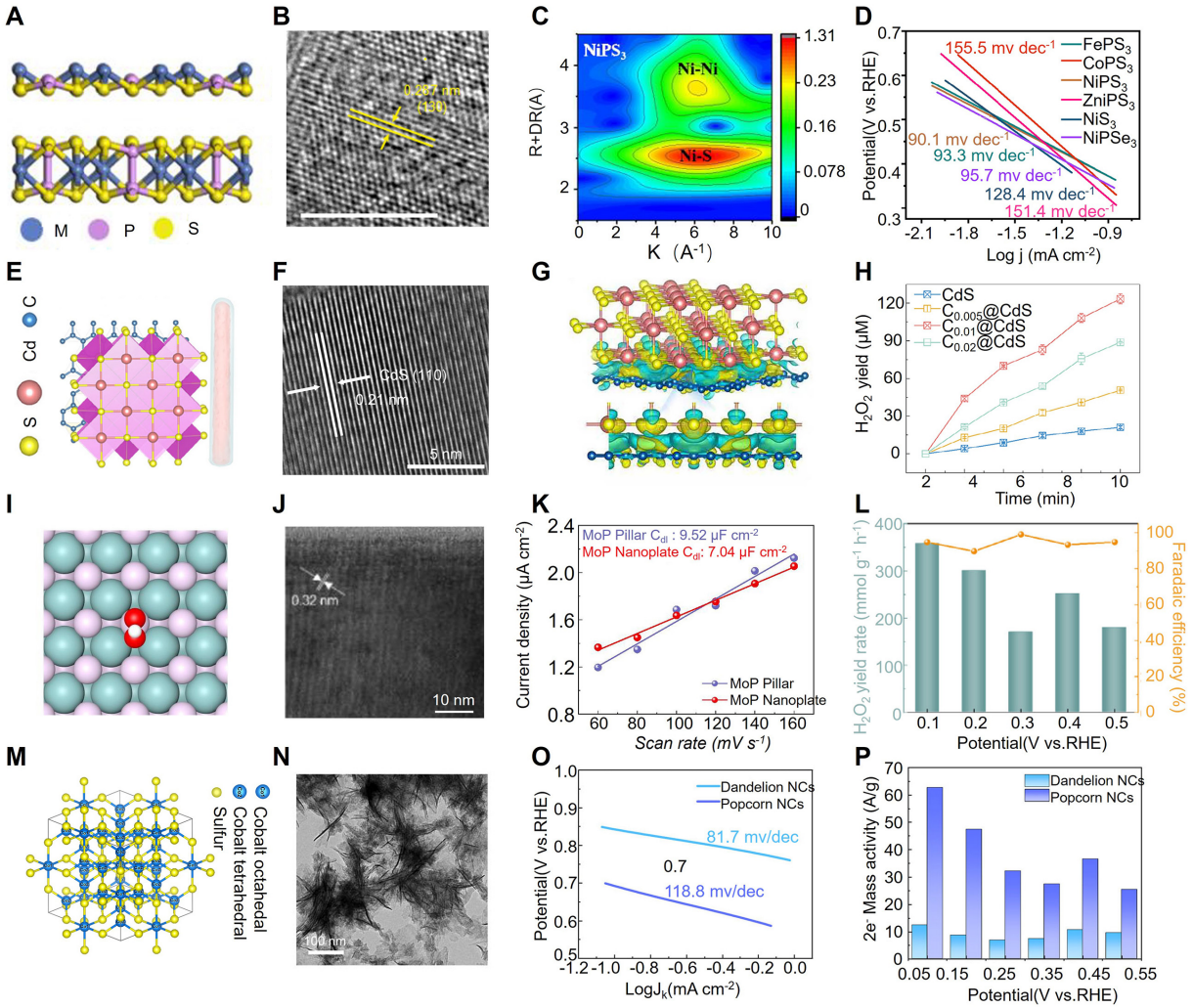



**Figure 9.** (A) Energetically optimized structure of $NiPS_3$. (B) High-resolution TEM image of $NiPS_3$. (C) EXAFS-related analysis of $NiPS_3$, where the two major peaks located at 2.52 and 3.47 A are attributed to the scattering of Ni-S and Ni-P paths, respectively, in accordance with the observations in the Ni K-edge WT-EXAFS. (D) Tafel plots of $FePS_3$, $CoPS_3$, $NiPS_3$, $ZnPS_3$, NiS, and $NiPSe_3$. (A-D) is reprinted with permission from Ref.[184]. Copyright © 2025 Springer Nature. (E) Final structural model of $C_{0.01}$@CdS nanorods in the schematic of pure CdS and $C_{0.01}$@CdS nanorods. (F) HRTEM image of $C_{0.01}$@CdS nanorods. (G) Charge density difference for C@CdS samples; blue and yellow colors denote electron depletion and accumulation areas, respectively. (H) $H_2O_2$ yield of pure CdS and C@CdS nanorods. (E-H) is reprinted with permission from Ref.[185]. Copyright © 2025 Wiley-VCH GmbH. (I) *OOH-adsorbed MoP (1010) phosphorus-terminated pillar surface. (J) High-resolution TEM image of a MoP pillar cross-section. (K) Double-layer capacitance determined from the scan-rate-dependent capacitive current densities of MoP pillars and MoP nanoplates. (L) $H_2O_2$ yield rates and Faradaic efficiencies of MoP pillars at potentials from 0.1 to 0.5 V *vs.* RHE. (I-L) is reprinted with permission from Ref.[186]. Copyright © 2025 Wiley-VCH GmbH. (M) Cubic crystal structure of $Co_9S_8$ generated using VESTA software. (N) TEM image of popcorn-shaped $Co_9S_8$ nanocrystals synthesized under inert conditions. (O) Mass-transfer-corrected Tafel plots for the two-electron oxygen reduction reaction. (P) Mass activities of Dandelion NCs and Popcorn NCs for the two-electron oxygen reduction reaction at different potentials. (O) Mass activity for the two-electron oxygen reduction reaction of the catalysts. (P) Mass-transfer-corrected Tafel plots of kinetic current densities for the two-electron oxygen reduction reaction; the kinetic current densities were calculated based on the Koutecky-Levich equation. (M-P) is reprinted with permission from Ref.[187]. Copyright © 2024 John Wiley and Sons.

the pillar cross-section then shows the crystalline quality and lattice structure of the MoP pillar [Figure 9J]. In the catalytic evaluation, the scan-rate-dependent capacitive current densities give double-layer capacitances of 9.52 and 7.04 μF $cm^{-2}$ for the MoP pillars and MoP nanoplates, respectively, indicating a larger electrochemically accessible surface area for the pillar architecture [Figure 9K]. The $H_2O_2$ yield rates and Faradaic efficiencies measured from 0.1 to 0.5 V *vs.* RHE further demonstrate the potential-dependent peroxide-production performance of the MoP pillars [Figure 9L]. From *OOH adsorption configuration,

lattice characterization, $H_2O_2$ production performance, and electrochemical surface analysis, this study indicates that exposed phosphide facets play a key role in regulating two-electron oxygen reduction reaction behavior. In another sulfide system, Kim *et al.*[187] reported ligand-driven electron-deficient $Co_9S_8$ nanocrystals. The cubic crystal structure of $Co_9S_8$ generated using visualization for electronic and structural analysis (VESTA) first presents the pentlandite lattice and Co/S atomic arrangement [Figure 9M]. The TEM image of popcorn-shaped $Co_9S_8$ nanocrystals synthesized under inert conditions then provides the representative nanoscale morphology of the catalyst [Figure 9N]. The mass-transfer-corrected Tafel plots subsequently reveal faster two-electron ORR kinetics for Dandelion NCs, with a Tafel slope of 81.7 mV $dec^{-1}$ compared with 118.8 mV $dec^{-1}$ for Popcorn NCs [Figure 9O]. Consistently, the potential-dependent mass activities further demonstrate the substantially higher two-electron ORR activity of Dandelion NCs across the investigated potential range [Figure 9P][187].

### *Metal carbides and nitrides*

Metal carbides and nitrides form another chemically distinctive catalyst family for two-electron electrocatalysis because the incorporation of carbon or nitrogen into a metal-centered lattice creates a bonding framework that differs fundamentally from those of metals, oxides, hydroxides, sulfides, or phosphides[188,189]. Their catalytic significance arises from the fact that interstitial or strongly coordinated C and N atoms do not behave merely as inert lattice occupants. Instead, they reshape the electronic structure of the metal sublattice, modify metal-metal spacing, alter charge density distribution, and establish a hybrid bonding regime that combines metallic conductivity with substantial covalent character. This combination is highly relevant to two-electron chemistry. Selective partial conversion requires an interface that can activate relatively stable substrates while avoiding the deep trapping of intermediates that would promote further reduction or oxidation[190]. Carbides and nitrides are often well positioned in this respect because their metal centers are electronically perturbed by neighboring C or N atoms in a way that can emulate certain aspects of noble-metal-like surface behavior while retaining access to chemically richer adsorption states. In carbides, the presence of carbon frequently induces strong metal-carbon hybridization and modifies the d-state distribution of the transition metal, which can weaken or rebalance adsorption of oxygenated intermediates relative to the parent metal[191]. In nitrides, the higher electronegativity of nitrogen and the often more polarized metal-nitrogen bonding can further alter the electron density and local electrophilicity of surface metal atoms[192-194]. The resulting surface chemistry is neither purely metallic nor conventionally ionic. It is best described as electronically reconstituted, with adsorption properties emerging from the coupled influence of conductive metal frameworks and strongly bound nonmetal sublattices. For two-electron electrocatalysis, this is advantageous because it creates a chemically differentiated surface on which the first productive electron-transfer event can remain accessible, while the subsequent transformation steps that drive multielectron conversion may become less favorable due to modified adsorbate covalency, altered bond polarization, or reduced propensity for excessive intermediate stabilization.

A second feature that makes carbides and nitrides important in this context is the way their lattice chemistry influences structural persistence and surface reactivity under electrochemical bias. The strongly integrated metal-carbon and metal-nitrogen frameworks often provide a degree of structural rigidity that differs from the more labile behavior of hydroxides or some sulfide- and phosphide-based systems, yet this rigidity does not imply chemical inertness. Instead, these materials can present surfaces in which partial oxidation, termination-dependent reconstruction, and near-surface heterogeneity generate catalytically active states that remain constrained by the underlying carbide or nitride scaffold. This is especially valuable for two-electron pathways, because selectivity often requires a surface that is reactive enough to engage the substrate but not so dynamically transformed that it continuously evolves toward structures favoring deeper redox chemistry. Carbides and nitrides can provide precisely such an intermediate regime. Their surfaces may support directional adsorption and efficient charge transfer, while the underlying lattice resists the formation of

excessively oxygen-affine or overhydrogenating environments that would erase the kinetic distinction between two-electron and multielectron channels[195]. At the same time, carbon- or nitrogen-modified metal centers can alter the balance between product desorption and readsorption, which is a decisive issue whenever the desired two-electron product is chemically vulnerable to further interfacial conversion. The broader materials-chemistry importance of this class therefore lies in its demonstration that selective electrocatalysis can be engineered not only by changing the surface element itself, but by embedding that element within a non-oxide covalent-metallic lattice that redefines its chemical behavior. Metal carbides and nitrides thus expand the conceptual space of two-electron electrocatalysis by offering catalyst platforms in which electronic reconstitution, lattice robustness, and chemically moderated adsorption cooperate to favor controlled arrest at a defined redox level rather than unrestricted descent into deeper reaction manifolds[196].

Metal carbides and nitrides have emerged as important material platforms for two-electron electrocatalysis because their high conductivity and stable metal-nonmetal bonding can be coupled with surface functionalization, lattice regulation, and interfacial reconstruction to tune key intermediate adsorption. In nitride-based systems, Liu *et al*.[197] reported triazolate-functionalized ZrN for air-fed $H_2O_2$ electrosynthesis. The HR-TEM image of T-ZrN displays the crystalline structure of the functionalized zirconium nitride, showing that the nitride lattice remains well defined after triazolate modification [Figure 10A]. The model of aqueous $O_2$ conversion on T-ZrN further illustrates how $O_2$ adsorbs and transforms on the functionalized surface, reflecting the regulatory effect of the triazolate ligand on the local oxygen-adsorption environment [Figure 10B]. To examine its response to different gas atmospheres, LSV curves of T-ZrN with $O_2$, air, Ar, $N_2$, or $CO_2$ flowing were compared to evaluate the electrochemical behavior under different feeding conditions, indicating that the main catalytic response originates from oxygen reduction [Figure 10C]. The $H_2O_2$ yield and Faradaic efficiency of T-ZrN under different current densities with $O_2$ or air flowing show that the catalyst can maintain peroxide production under air-fed and high-current-density conditions [Figure 10D][197]. This work demonstrates that triazolate modification can regulate $O_2$ adsorption on ZrN, converting a stable nitride surface into an air-fed two-electron oxygen reduction reaction catalytic interface. Different from this surface-ligand strategy, Li *et al*.[198] developed ordered $Ni_3ZnC_{0.7}$/C from the perspective of intermetallic lattice regulation. The HR-TEM image of $Ni_3ZnC_{0.7}$/C presents the crystalline structure of carbon-supported ordered Ni-Zn-C nanoparticles, providing morphological and structural evidence for the catalyst [Figure 10E]. The charge-density difference of $Ni_3ZnC_{0.7}$/C(111) with *OOH adsorption reveals electronic redistribution around the oxygenated intermediate from a side-view perspective, indicating that the ordered lattice can alter the local adsorption environment of *OOH [Figure 10F]. The activity volcano plot based on *OOH adsorption free energy further shows that moderate *OOH adsorption is essential for high two-electron oxygen reduction reaction selectivity [Figure 10G]. The $H_2O_2$ yield rate and Faradaic efficiency at corresponding potentials then verify the potential-dependent $H_2O_2$ electrosynthesis performance of $Ni_3ZnC_{0.7}$/C [Figure 10H][198].

If T-ZrN and $Ni_3ZnC_{0.7}$/C emphasize surface modification and ordered lattice regulation, $Ni_3N$/MX and FeN/$Fe_3N$ further reveal the importance of structural evolution during reaction and heterointerface effects. Liu *et al*.[199] reported $Ni_3N$/MX, in which $Ni_3N$ undergoes surface reconstruction under oxygen reduction reaction conditions to form NiOOH-related active species. The HR-TEM image of $Ni_3N$/MX shows the lattice structure of the nickel nitride phase, providing a structural basis for understanding subsequent electronic modulation and reconstruction behavior [Figure 10I]. At the interfacial electronic level, the charge-density distribution of $Ni_3N$/$Ti_3CN$ reveals electronic interaction between the nitride and $Ti_3CN$, suggesting that the conductive substrate can influence the electronic state of the Ni-based surface through charge transfer [Figure 10J]. With attention to the reconstructed surface, the charge-distribution disparity between *OOH on NiOOH/$Ni_3N$ and NiO/$Ni_3N$ shows that different oxide/oxyhydroxide surface states lead to distinct *OOH electronic environments and adsorption behaviors [Figure 10K]. Accordingly, the $H_2O_2$

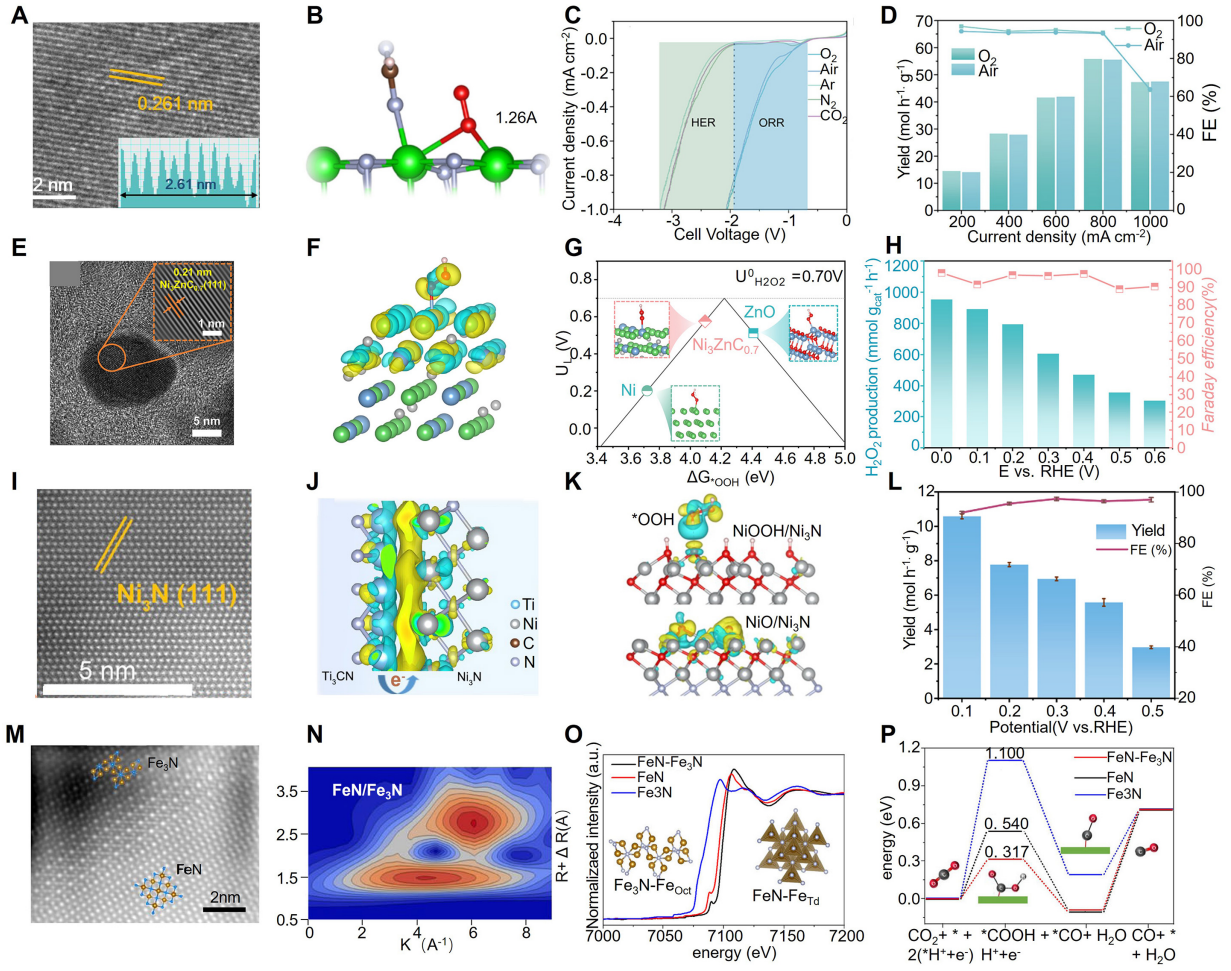



**Figure 10.** (A) HR-TEM image of T-ZrN. (B) Structural model of the conversion of aqueous $O_2$ on T-ZrN. (C) LSV curves of T-ZrN with $O_2$, air, Ar, $N_2$, or $CO_2$ flowing. (D) $H_2O_2$ yield and Faradaic efficiency of T-ZrN under different current densities with $O_2$ or air flowing. (A-D) is reprinted with permission from Ref.[197]. Copyright © 2025 American Chemical Society. (E) HR-TEM image of $Ni_3ZnC_{0.7}$/C. (F) Charge density difference of $Ni_3ZnC_{0.7}$/C (111) with *OOH adsorption, side view. (G) Activity volcano plot for the two-electron oxygen reduction reaction based on *OOH adsorption free energy. (H) $H_2O_2$ yield rate and Faradaic efficiency of $Ni_3ZnC_{0.7}$/C at the corresponding potentials. (E-H) is reprinted with permission from Ref.[198]. Copyright © 2026 Elsevier B.V. (I) HR-TEM images of $Ni_3N$/MX. (J) Charge density distribution of $Ni_3N/Ti_3CN$. (K) Disparity in charge distribution between *OOH on NiOOH/$Ni_3N$ and NiO/$Ni_3N$. (L) $H_2O_2$ yield and Faradaic efficiency of $Ni_3N$/MX under $O_2$ flowing at different potentials; the test time under each potential is 1 h. (I-L) is reprinted with permission from Ref.[199]. Copyright © 2025 Elsevier B.V. (M) HRHAADF-STEM image of the FeN/$Fe_3N$ interface. (N) Wavelet transforms for the $k^3$-weighted EXAFS signals of FeN/$Fe_3N$. (O) Normalized Fe K-edge EXAFS spectra; inset: the local FeN structure showing tetrahedral coordination and the $Fe_3N$ structure showing octahedral coordination. (P) Calculated Gibbs free-energy diagrams for carbon dioxide reduction reaction on FeN, $Fe_3N$, and FeN/$Fe_3N$ surfaces. (M-P) is reprinted with permission from Ref.[200]. Copyright © 2023 Springer Nature.

yield and Faradaic efficiency of $Ni_3N$/MX under $O_2$ flowing at different potentials demonstrate that the reconstructed Ni-based surface can promote $H_2O_2$ generation in the two-electron oxygen reduction reaction [Figure 10L][199]. This system suggests that the activity of nitrides may not originate solely from the initial nitride phase; the reconstructed surface generated during operation can also become a decisive selectivity-determining structure. In contrast to the reconstruction-centered $Ni_3N$/MX system, Yin *et al.*[200] constructed FeN/$Fe_3N$ heterostructured nanoparticles to emphasize the role of nitride-nitride interfaces in the two-electron reduction of $CO_2$ to CO. The HRHAADF-STEM image of the FeN/$Fe_3N$ interface directly presents the atomic arrangement at the junction between the two nitride phases, offering visual evidence for the interfacial structure [Figure 10M]. The wavelet transforms for the $k^3$-weighted EXAFS signals of FeN/$Fe_3N$ further record the local coordination features around Fe sites, reflecting the coexistence of different Fe-N

coordination environments at the interface [Figure 10N]. The normalized Fe K-edge EXAFS spectra compare the local structural differences among FeN/$Fe_3N$, FeN, and $Fe_3N$, while the inset distinguishes tetrahedral FeN coordination from octahedral $Fe_3N$ coordination [Figure 10O]. In terms of reaction energetics, the calculated Gibbs free-energy diagrams for carbon dioxide reduction reaction on FeN, $Fe_3N$, and FeN/$Fe_3N$ surfaces show that the heterointerface provides a more favorable pathway for *COOH formation and CO generation [Figure 10P][200].

Beyond conventional catalyst families, emerging materials such as MOFs, COFs, and SACs further expand the structural design space for two-electron electrocatalysis by providing highly tunable coordination environments and electronically distinct active sites. MOFs and COFs offer controllable pore structures, ligand environments, and spatially defined catalytic centers, enabling regulation of substrate confinement, local solvation, charge transfer, and intermediate stabilization at the molecular level. SACs, in contrast, provide atomically dispersed metal centers whose coordination number, ligand identity, oxidation state, and electronic coupling with the support can be precisely tailored. These structural features allow the adsorption configuration and electronic activation of key intermediates to be selectively modulated, which is particularly relevant for distinguishing desired two-electron pathways from deeper multielectron conversion. However, the high structural tunability of these materials does not inherently guarantee enhanced two-electron selectivity; excessive confinement, overly strong coordination, or insufficient structural stability may instead promote intermediate retention and subsequent reaction. Their effectiveness therefore depends on precise control of the local coordination and interfacial environment to establish an appropriate balance between substrate activation, intermediate stabilization, and product release.

### Catalyst landscape and performance summary for two-electron electrocatalysis

To provide a more systematic understanding of the current state of inorganic two-electron electrocatalysis, the representative catalysts, reaction media, and key performance metrics reported across different two-electron reaction systems are summarized in Table 1. This compilation reveals several common trends that transcend individual reactions and catalyst families. First, two-electron electrocatalysis has evolved from conventional noble-metal catalysts toward structurally engineered inorganic materials with increasingly diverse compositions and architectures. While Pd/C, Au, and Ag remain benchmark catalysts in oxygen reduction, carbon dioxide reduction, and nitrate reduction, respectively, recent studies increasingly rely on oxide-derived materials, transition-metal chalcogenides, carbides, nitrides, single-atom catalysts, heterostructures, and defect-engineered interfaces to regulate intermediate adsorption and suppress competing multielectron pathways. Second, catalyst performance is now characterized by a simultaneous optimization of selectivity, stability, and activity rather than by Faradaic efficiency alone. Across the summarized systems, product selectivity frequently exceeds 90%, with numerous catalysts reaching 95%-100%, such as ZnO@$ZnO_2$ (97.75%-100%), $Co(OH)_2$/C-Co-S/Co-SCD-2 (95.2%–98.2%), C-N-O/HG-CD-Ph (94.93%), Co-O-C/N-C/DAT-HOF@Co-HHTP (99.3%), Ag catalysts for nitrate reduction (99.5%-99.9%), and $RuO_4$/C/Ru-$O_4$ SAM for chlorine evolution (99%). Likewise, Faradaic efficiencies above 95% have become increasingly common, with several systems approaching quantitative electron utilization, including Cu/Ni-NC (≈100%), Li-$Bi_2O_2CO_3$/BOC-Li (>95%), Co (≈93%), Ag (97.9%-98.4%), and $In_2O_3$/$SnO_2$/rGO (98.3%). Stability has also improved substantially, ranging from conventional operation over 10-20 h to 100, 289, 450, 600, and even 1,000 h, while certain oxygen reduction catalysts maintain activity for 60,000 s without significant degradation. A further notable trend is the emergence of high-current-density operation. Stable performance has already been demonstrated at 300, 700, and 1,200 mA $cm^{-2}$, indicating that selective two-electron pathways are no longer restricted to low-flux laboratory conditions. From a structural perspective, these improvements consistently correlate with catalysts capable of simultaneously weakening excessive intermediate binding while preserving sufficient activation of the first electron-transfer step. Materials possessing electronically regulated active centers, asymmetric coordination

environments, defect-modified surfaces, heterointerfaces, or compositionally coupled phases generally outperform structurally homogeneous catalysts because they broaden the kinetic window separating desired two-electron termination from deeper reduction or oxidation. Collectively, these observations suggest that the field is gradually shifting from empirical catalyst discovery toward structure-guided regulation of oxidation-state-specific reaction pathways, where precise control over intermediate energetics rather than maximal intrinsic activity has become the defining criterion for high-performance two-electron electrocatalysis.

## REACTION-SPECIFIC TWO-ELECTRON ELECTROCATALYSIS

Having established the conceptual basis, structural determinants, and catalyst classes of two-electron electrocatalysis, the discussion can now be advanced to specific reaction systems in which these general principles acquire chemically explicit form. Such a transition is necessary because the meaning of two-electron selectivity is ultimately defined within concrete reaction coordinates, where substrate identity, bond-evolution pattern, proton-coupling mode, and competing redox channels together determine whether a partially transformed state can emerge as the dominant product. Oxygen reduction and water oxidation represent a redox-connected pair centered on peroxide-level chemistry, yet they differ fundamentally in whether selectivity depends on suppressing overreduction or overoxidation[235,236]. Carbon dioxide reduction introduces a distinct problem of partial carbon-centered reduction in which oxygen-retaining products must be differentiated from deeper deoxygenation pathways. Nitrate reduction further increases mechanistic complexity because two-electron nitrite formation is embedded within a dense nitrogen redox network that readily proceeds toward more reduced species. Halide oxidation, by contrast, provides an anodic counterpart in which selective halogen generation must compete against oxygen evolution under strongly oxidizing conditions. Considered together, these five reaction families cover the principal inorganic manifestations of two-electron electrocatalysis and provide a chemically coherent basis for comparing how common selectivity principles are expressed across fundamentally different redox environments. On this basis, the following sections discuss each reaction class in sequence, with emphasis on reaction fundamentals, pathway competition, and catalyst design logic[237].

### Two-electron oxygen reduction reaction

Among all reaction-specific manifestations of two-electron electrocatalysis, the two-electron oxygen reduction reaction occupies the most central position because it transforms a readily available oxidant, $O_2$, into $H_2O_2$ through a chemically defined partial reduction process that is both mechanistically revealing and industrially consequential. Its cathodic half-reaction can be expressed in acidic electrolyte as $O_2 + 2H^+ + 2e^- \rightarrow H_2O_2$ and in alkaline medium as $O_2 + H_2O + 2e^- \rightarrow HO_2^- + OH^-$, with the actual product distribution governed by local proton activity and the acid-base equilibrium between $H_2O_2$ and $HO_2^-$[238,239]. The reaction is chemically distinctive because the desired two-electron product is formed only when the O-O bond remains intact throughout substrate activation and proton-coupled electron transfer. This requirement immediately differentiates the process from the four-electron reduction to $H_2O$, in which oxygen activation proceeds through eventual O-O cleavage and complete reduction of both oxygen atoms. The two-electron oxygen reduction reaction is therefore best understood as a selective bond-preserving reduction in which the catalytic interface must recognize peroxide formation as a terminal redox outcome rather than as a transient intermediate en route to deeper reduction. This feature gives the reaction a dual importance[240,241]. On the one hand, $H_2O_2$ is itself a high-value molecular oxidant with broad relevance to chemical synthesis, disinfection, bleaching, environmental remediation, and decentralized oxidation chemistry. On the other hand, the reaction provides one of the clearest model systems for interrogating how electrocatalytic interfaces govern partial versus complete redox conversion[242]. The chemical challenge arises from the fact that $O_2$ is a triplet ground-state molecule with substantial kinetic stability, so activation requires charge transfer into antibonding orbitals and the formation of a hydroperoxo-like intermediate state, yet the same

**Table 1. Compilation of representative electrocatalytic performances for two-electron transfer reactions**

| Reaction type | Catalysts | Electrocatalytic | Tafel slope (mV $dec^{-1}$) | Selectivity | Stability | Faradaic efficiency (%) | Ref. |
|---|---|---|---|---|---|---|---|
| 2e⁻ ORR | BiNi/C | 0.1 M KOH | 78.5 | > 90%@0.20-0.60 V | 17 h@0.4 V | > 80%@0.20-0.60 V | [147] |
| 2e⁻ ORR | PdCu/C | 0.1 M $HClO_4$ | | > 85%@0.15-0.60 V | 10 h@0.35 V | | [148] |
| 2e⁻ ORR | Au-$Pd_2Hg_5$ | 0.1 M $HClO_4$ | | 92.8%@0.0-0.4 V | 10 h | 71.6% | [149] |
| 2e⁻ ORR | Pd@$Pt_{0.05}Au_{0.95\text{-}6L}$ | 0.1 M $HClO_4$ | | 90%@0.36 V | | 85%@0.36 V | [150] |
| 2e⁻ ORR | Co-$N_3$SC | 0.1 M $KHCO_3$ | 54 | 97%@0.5 V | 110 h@180 mA $cm^{-2}$ | 82.5%@180 mA $cm^{-2}$ | [201] |
| 2e⁻ ORR | Ni-N/S-C/Ni-SAC | 0.1 M KOH | 79.5 | | 20 h@0.3 V | ~85%@0.3-0.7 V | [202] |
| 2e⁻ ORR | Sb-$N_4$/S-C/Sb-NSCF | 0.1 M KOH⁻ | 29.4 | > 90%@0.40-0.70 V | 10 h@0.65 V | | [203] |
| 2e⁻ CER | $(Fe,Co,Ni)_3O_4$ /C/FCNO@CQDs | 5 M NaCl | 49.5 | 98.8%-99.7% | 240 h@1.48 V | | [204] |
| 2e⁻ ORR | $Fe_3O_4$/N-C/$Fe_3O_4$@TNC | 0.1 M LiClO | 147 | ≈96%@0.70 V | 12 h@0.5 V | 96%@0.70 V | [164] |
| 2e⁻ ORR | ZnO@$ZnO_2$ | M $K_2SO_4$ | | 97.75%-100% | 12 h@0.1 V | 95.5%@0.1 V | [166] |
| 2e⁻ ORR | $Co(OH)_2$/C-O-S /Co-SCD-2 | 0.1 M KOH | 60.0 | 95.2%-98.2% @0.1-0.65 V | 50 h@0.6 V | 94.9%@0.6 V | [173] |
| 2e⁻ $CO_2$RR | CuHHTP/$Cu(OH)_2$ | 1 M $KHCO_3$-KCl | | | 66 h@-1.4 V | 88.8%@−1.4 V | [205] |
| 2e⁻ ORR | NiOOH/$In(OH)_3$ | 0.1 M KOH | | > 90%@0.2-0.6 V | 0.5 h@0.4 V | ≈98.1%@0.4 V | [174] |
| 2e⁻ ORR | $NiPS_3$ | 0.5 M NaCl | 90.1 | ≈98% | 1,000 h@0 V | 85%@100 mA $cm^{-2}$ | [184] |
| 2e⁻ $CO_2$RR | C@$In_2O_3$ | 0.05 M $H_2SO_4$ + 0.05 M $K_2SO_4$ +0.1 M $K^+$ | | | > 100 h@300 mA $cm^{-2}$ | 98.9%@300 mA $cm^{-2}$ | [206] |
| 2e⁻ $CO_2$RR | FeN/$Fe_3N$ | 0.5 M $KHCO_3$ | | | 100 h@-0.4 to -0.9 V | 98%@−0.4 V | [200] |
| 2e⁻ ORR | $Ni_3ZnC_{0.7}$/C | 0.1 M KOH | 85.15 | > 92%@0.2-0.6 V | 13 h@0.5 V | 98.3%@0 V | [198] |
| 2e⁻ ORR | S-$C_2^+$ | 0.1 M $HClO_4$ | 53.1 | 99.3%@0.4 V | 60,000 s@0.4 V | 96.8%@0.4 V | [9] |
| 2e⁻ ORR | Ni-N-C/$PW_{12}O_{40}$ /Ni-HITP/$PW_{12}$-2 | 0.1 M KOH | 88.0 | 96.12%-97.94% @0.2-0.5 V | 48 h@0 V | 81%@80 mA $cm^{-2}$ | [207] |
| 2e⁻ ORR | C-N-O/HG-CD-Ph | 0.1 M KOH | 75.56 | 94.93%@0.4 V | 10 h@0.4 V | 98.01%@80 mA $cm^{-2}$ | [1] |
| 2e⁻ ORR | Co-O-C/N-C /DAT-HOF@Co-HHTP | 0.1 M PBS | 71.3 | 99.3%@0.6 V | 100 h@1,200 mA $cm^{-2}$ | 97.1 ± 0.4%@1,200 mA $cm^{-2}$ | [208] |
| 2e⁻ WOR | $V_2CT_x$/$(C_8H_{16}NCl)_n$ | 3.5 M $K_2CO_3$ + 0.5 M $KHCO_3$ | 252 | | 450 min@3.2 V | ≈80%@3.2 V | [209] |
| 2e⁻ $CO_2$RR | CuS | 1.0 M KOH | | Nearly complete @-0.4 to -0.7 V | 96 h@-0.6 V | > 85% | [210] |
| 2e⁻ $CO_2$RR | $In_2O_3$/$SnO_2$/rGO | 0.5 M $K_2SO_4$ | | | > 24 h@700 mA $cm^{-2}$ | 98.3%@700 mA $cm^{-2}$ | [211] |
| 2e⁻ $CO_2$RR | Li-$Bi_2O_2CO_3$/BOC-Li | 1.0 M KOH | 64 | | 289 h@100 mA $cm^{-2}$ | > 95% | [212] |
| 2e⁻ $NO_3$RR | $CuSn(OH)_6$ | 10 mM $NaNO_3$ + 100 mM $Na_2SO_4$ | | 97%@-0.7 V | 10 cycles × 30 min@-0.7 V | ≈75%@-0.7 V | [213] |
| 2e⁻ CER | Ce-$Co_3O_4$ | 4.0 M NaCl, pH = 2 adjusted with $HClO_4$ | 58.2 | | 600 h@10 mA $cm^{-2}$ | | [214] |
| 2e⁻ CER | Fe-$Ti_4O_7$ | Unbuffered natural seawater, $Cl^-$ ≈ 0.5 M | 98 | | 10 days@10 mA $cm^{-2}$ | 75%@10 mA $cm^{-2}$ | [215] |
| 2e⁻ $NO_3$RR | Ag | 1.61 mM $NaNO_3$ + 0.05 M $Na_2SO_4$ | | 99.5%@-1.2 V *vs*. Ag/AgCl | 108 h@-1.2 V *vs*. Ag/AgCl | 97.9%@-1.2 V *vs*. Ag/AgCl | [216] |
| 2e⁻ $NO_3$RR | Cu/Cu-O/OD-CF | $Na_2SO_4$ + 100 mg-N $L^{-1}$ $NO_3^-$ | | 98.0%@-0.16 V | | | [217] |

| | | | | | | | |
|---|---|---|---|---|---|---|---|
| 2e⁻ $NO_3RR$ | Ti | 1 M $NaClO_4$ + 10 mM $HNO_3$ | | 83.3%@-1.0 V | | 34.1%@-1.0 V | [218] |
| 2e⁻ $NO_3RR$ | Ag | 100 mM $NaNO_3$ + 50 mM $Na_2SO_4$ | | 99.90%@-1.0 V *vs.* Ag/AgCl | | 98.40%@-1.0 V *vs.* Ag/AgCl | [219] |
| 2e⁻ CER | $RuO_4$/C/Ru-$O_4$ SAM | 1 M NaCl, pH = 1 | 48.2 | 99%@~10.8 mA $cm^{-2}$ | 12 h@10 mA $cm^{-2}$ | | [220] |
| 2e⁻ IOR | Ru-Sn-O/RuSn SAO | 0.1 M $HClO_4$ + 0.1 M NaI | 40 | | 30 h@10 mA $cm^{-2}$ | ≈92%@1.07 V cell voltage | [221] |
| 2e⁻ $CO_2RR$ | Cu/Ni-NC | 0.5 M $KHCO_3$ | 157 | | 20 h@-0.9 V | ≈100%@-0.9 V | [222] |
| 2e⁻ $CO_2RR$ | L-Ni-NC-C | 0.1 M $KHCO_3$ | 144 | | 50 h@-0.9 V | > 96%@-0.9 V | [223] |
| 2e⁻ $NO_3RR$ | $Fe^0$ | 0.05 M $Na_2SO_4$ + 50 mg N $L^{-1}$ $NaNO_3$ | | 78.9% ± 3.2%@10 mA | 10 h@10 mA | 91.6% ± 2.7%@10 mA | [224] |
| 2e⁻ $CO_2RR$ | Fe-P-N-C | 1.0 M KOH | 151 | | 50 h@-1.17 V | ≈80%@-1.17 V | [225] |
| 2e⁻ $CO_2RR$ | $CoN_4O$/$ZnN_4$-C /COF@$MOF_{800}$-Co | 0.5 M $KHCO_3$ | 350 | | 30 h@-0.8 V | 92.6%@-0.8 V | [226] |
| 2e⁻ WOR | $In_2O_3$/$SnO_2$/Pt/ITO/Pt | 0.92 M $KHCO_3$ + 3.08 M $K_2CO_3$ | | | 72 h@2.7 V | ≈50%@2.8-3.5 V | [227] |
| 2e⁻ WOR | $C_3N_2$/HAT-CTF | 1.0 M $K_2CO_3$ | | | 24 h@2.7 V | 48.2%@2.7 V | [228] |
| 2e⁻ WOR | $LiScO_2$ | 0.5 M $KHCO_3$ | 69 | | 168 h@2.2 V | = 82%-86%@2.2 V | [229] |
| 2e⁻ WOR | $Mg_{1-x}SnWO_{6-x}$700 | 2 M $KHCO_3$ | 143.84 | | 35 h@2.6 V | = 84.81%@2.6 V | [230] |
| 2e⁻ $CO_2RR$ | In/C/mp-In@MWCNTs | 0.1 M $KHCO_3$ | 134 | | 30 h@-1.0 V | > 90%@-1.0 V | [231] |
| 2e⁻ $CO_2RR$ | BiS-1 | 1.0 M KOH | | | 16 h@300 mA $cm^{-2}$ | ≈95%@2,000 mA $cm^{-2}$ | [232] |
| 2e⁻ BER | $Co_3O_{4-x}$/C/Co-OV@CP | 0.5 M NaBr | ≈48 | | 80 h@10 mA $cm^{-2}$ | | [233] |
| 2e⁻ $CO_2RR$ | Cu/$C_{19}H_{42}BrN$/Cu-CTAB | 0.5 M $KHCO_3$ + 0.167 mM CTAB | ≈110 | | 10 h@-0.5 V | 82.3%@-0.5 V | [234] |

activation event can also lower the barrier toward O-O bond scission if the interface binds oxygen too strongly or permits excessive electron accumulation. Selective two-electron oxygen reduction therefore sits at a narrow mechanistic boundary between underactivation and overreduction. If adsorption is insufficient, $O_2$ remains poorly activated and the first proton-coupled electron transfer becomes sluggish. If adsorption is too strong, the peroxide-level state loses kinetic independence and the surface instead channels the reaction toward complete reduction[243,244]. This balance explains why the two-electron oxygen reduction reaction has become a paradigmatic system in selective electrosynthesis. It compresses several core themes of modern electrocatalysis into a single chemically tractable problem, including spin-sensitive $O_2$ activation, proton-coupled electron transfer, interfacial stabilization of oxygenated intermediates, acid-base-dependent product speciation, and the kinetic survival of a partially reduced molecular product at the electrified interface. For these reasons, this reaction is not only one of the most developed two-electron electrocatalytic transformations, but also one of the most conceptually informative for understanding how a catalytic surface can stop electron flow at a prescribed oxidation-state level and thereby convert molecular oxygen into a selectively released peroxide product rather than a fully reduced endpoint[245-247].

In the two-electron oxygen reduction reaction toward $H_2O_2$ production, the adsorption of *OOH on catalytic sites is important, while proton supply, local electric fields, and interfacial water structures also strongly influence the selective conversion of $O_2$ to $H_2O_2$. Zou *et al.*[208] constructed a DAT-HOF@Co-HHTP heterostructure by integrating hydrogen-bond-rich DAT-HOF with conductive Co-HHTP for ampere-level $H_2O_2$ electrosynthesis. The calculated charge-density difference of DAT-HOF@Co-HHTP shows electron accumulation and depletion at the heterointerface, indicating that interfacial Co-N bonding modulates the

electronic structure of Co sites and creates a favorable local environment for oxygen-intermediate adsorption [Figure 11A]. The SEM image after the stability test further displays the rod-like heterostructure morphology of DAT-HOF@Co-HHTP, suggesting that the assembled structure is largely retained after long-term operation [Figure 11B]. From the thermodynamic perspective, the free-energy diagrams for oxygen reduction reaction over Co-HHTP and DAT-HOF@Co-HHTP compare the conversion of key intermediates, showing that the heterostructure optimizes the energy profile of the oxygen-reduction pathway [Figure 11C]. The corresponding schematic diagram of oxygen reduction reaction pathways links $O_2$ adsorption, *OOH formation, *HOOH conversion, and $H_2O_2$ desorption, further illustrating the synergy among electronic modulation, proton migration, and oxygen-intermediate transformation at the HOF/cMOF heterointerface [Figure 11D][208]. This study indicates that high-current-density $H_2O_2$ production relies not only on Co active sites, but also on a reaction microenvironment jointly constructed by conductive frameworks, proton-donating components, and interfacial electric fields. Different from the HOF@cMOF strategy that emphasizes interfacial proton migration, Wang *et al*.[248] investigated proton-transfer pathway selection in a solid-state electrolyte using NiSA-NiO/pCNs. The final structural model in the synthesis scheme of NiSA-NiO/pCNs shows the coexistence of Ni single-atom sites and NiO nanoclusters on porous carbon nanosheets, providing a basis for understanding the cooperation between single-atom oxygen reduction reaction sites and water-dissociation sites [Figure 11E]. The high-resolution TEM image, where NiO lattices are circled by dashed lines, further confirms the presence of NiO nanoclusters, suggesting their role as functional units for water dissociation and proton-feeding regulation [Figure 11F]. On this basis, the proposed illustration of two catalytic pathways distinguishes the Langmuir-Hinshelwood and Eley-Rideal mechanisms: NiSA/pCNs mainly relies on surface *H for protonation, whereas NiSA-NiO/pCNs uses NiO to promote water dissociation, allowing interfacial water to directly participate in the conversion from $*O_2^-$ to *OOH [Figure 11G][248].

Following this microenvironment-regulation perspective, the focus can be further extended from catalyst-internal structures to the electrolyte/electrode interface and second-sphere coordination environments. Wang *et al*.[249] used Co-CNT as a model catalyst to examine how alkali metal cations influence interfacial water structures and $H_2O_2$ formation in acidic media. The optimized adsorption configuration model on Co-CNT shows the local arrangement of reactants and the interfacial water environment under $H^+/Cs^+$ conditions, suggesting that $Cs^+$ can perturb the interfacial hydrogen-bond network through its hydration structure and thereby affect proton delivery to active sites [Figure 11H]. The AC-HAADF-STEM image provides microscopic structural evidence for Co-CNT, allowing the discussion of interfacial water regulation and electrochemical behavior to be connected with a defined catalyst morphology [Figure 11I]. At 0.7 V *vs*. RHE, the free-energy diagrams for oxygen reduction reaction on Co-CNT across different electrolyte systems compare both the four-electron and two-electron pathways; the insets show molecular models of different stages for $H_2O_2$ synthesis, indicating that alkali metal cation-induced interfacial water restructuring can influence proton-coupled steps and $H_2O_2$ selectivity [Figure 11J][249]. In contrast to external electrolyte regulation, Cheng *et al*.[250] adopted a bio-inspired B-coordination strategy to modify the second coordination sphere of Ni-based MOFs. The fitting models for B-NiBDC show the modified Ni coordination environment after introducing B-O-Ni motifs, indicating that second-sphere regulation changes the local electronic structure around Ni active centers [Figure 11K]. The HRTEM image of B-NiBDC after the two-electron oxygen reduction reaction tests further shows that the catalyst retains structural features after the oxygen reduction process, supporting its morphological stability during operation [Figure 11L]. The efficient the two-electron oxygen reduction reaction pathway then highlights the coupling between proton feeding and suitable *OOH adsorption, where electron-deficient Ni sites induced by B-O-Ni motifs lower the water-dissociation barrier, accelerate proton feeding, and promote *OOH formation and $H_2O_2$ desorption [Figure 11M][250].

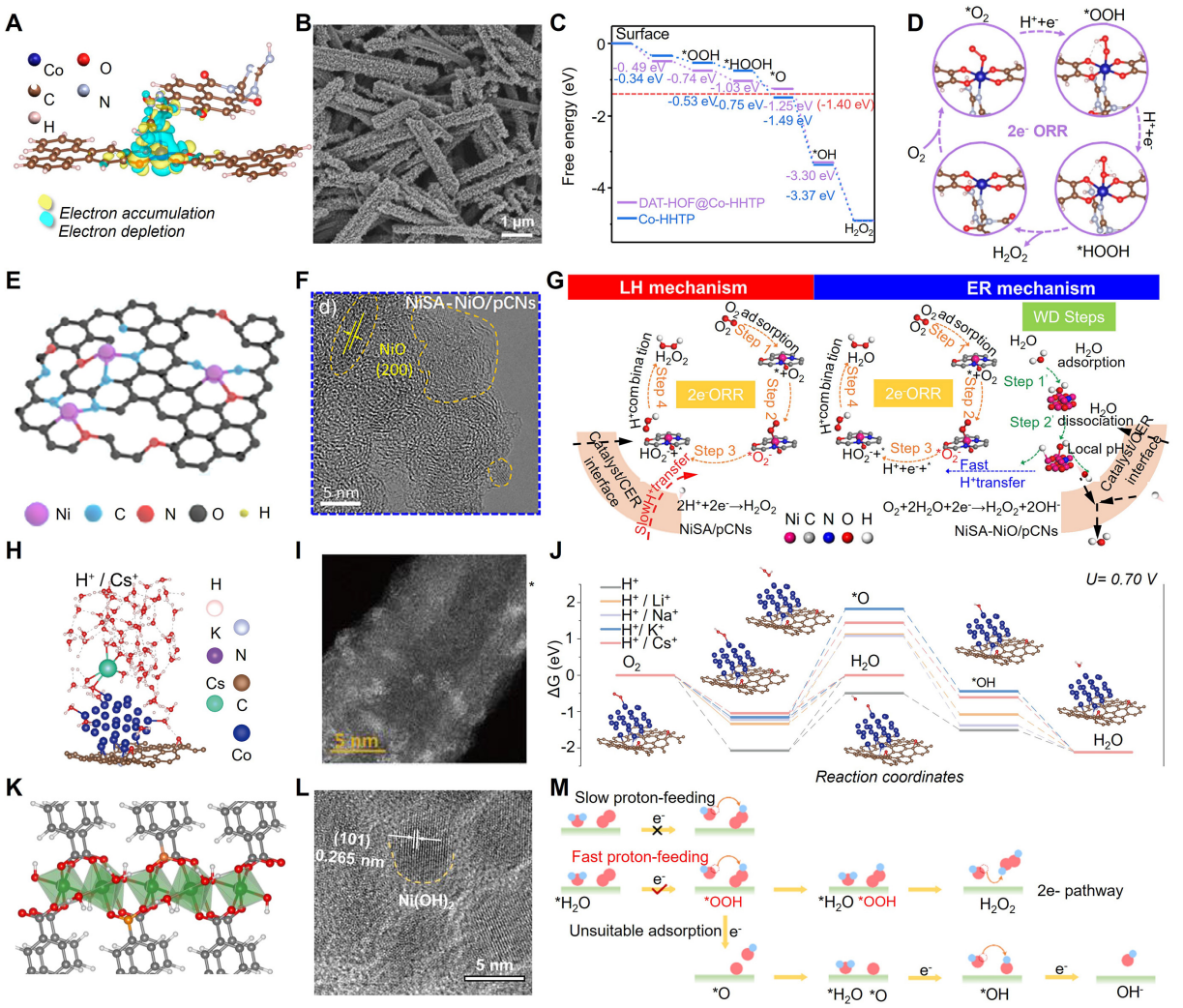



**Figure 11.** (A) Calculated charge-density difference of DAT-HOF@Co-HHTP heterostructure. (B) SEM image of DAT-HOF@Co-HHTP after the stability test. (C) Free-energy diagrams for oxygen reduction reaction over Co-HHTP and DAT-HOF@Co-HHTP heterostructure. (D) Schematic diagram of the oxygen reduction reaction pathways over DAT-HOF@Co-HHTP heterostructure. (A-D) is reprinted with permission from Ref.[208]. Copyright © 2025 Springer Nature. (E) Final structural model in the schematic illustration for the synthesis process of NiSA-NiO/pCNs; C, H, O, N, and Ni are shown in grey, yellow, red, blue, and purple, respectively. (F) High-resolution TEM image of NiSA-NiO/pCNs, where NiO lattices are circled by dashed lines. (G) Proposed illustration of two catalytic pathways for the two-electron oxygen reduction reaction process in chlorine evolution reaction electrolyte. (E-G) is reprinted with permission from Ref.[248]. Copyright © 2025 Wiley-VCH GmbH. (H) Optimized computational adsorption configuration model on the Co-CNT catalyst in $Cs^+$-containing acidic electrolyte. (I) AC-HAADF-STEM image of Co-CNT. (J) Free-energy diagrams for oxygen reduction reaction on Co-CNT catalysts across different electrolyte systems at 0.7 V_RHE, including both the 4e$^-$ and the two-electron reaction pathways; the insets show molecular models of different stages for $H_2O_2$ synthesis. (H-J) is reprinted with permission from Ref.[249]. Copyright © 2026 Springer Nature. (K) Fitting models for B-NiBDC; gray, white, green, red, and orange represent C, H, Ni, O, and B atoms, respectively. (L) HRTEM image of B-NiBDC after the two-electron oxygen reduction reaction tests. (M) Efficient the two-electron oxygen reduction reaction pathway enabled by proton feeding and suitable *OOH adsorption. (K-M) is reprinted with permission from Ref.[250]. Copyright © 2025 Springer Nature.

## Two-electron water oxidation reaction

The two-electron water oxidation reaction represents the anodic counterpart of peroxide-level oxygen electrocatalysis and is chemically remarkable because it seeks to generate $H_2O_2$ directly from $H_2O$ rather than from molecular $O_2$. In acidic medium, the overall half-reaction can be written as $2H_2O \rightarrow H_2O_2 + 2H^+ + 2e^-$, whereas in alkaline solution it is more appropriately described through hydroxide participation and the corresponding proton-balance relations at the interface. Its fundamental challenge is intrinsically different from that of the two-electron oxygen reduction reaction. Here the catalytic interface must not preserve an

existing O-O bond, but instead create an O-O linkage and terminate oxidation at the peroxide level before the system descends into the more prevalent four-electron oxygen evolution reaction[251]. The reaction is therefore a chemically stringent test of selective anodic control, because the desired product is formed in an electrochemical regime where further oxidation is not only possible but often favored. This makes two-electron water oxidation a rare example of selective overoxidation avoidance under strongly oxidizing conditions[252]. At the molecular level, the process requires the interface to mediate proton-coupled electron abstraction from water-derived oxygen species while controlling the oxidation state and coupling mode of surface-bound intermediates so that O-O bond formation yields a peroxide-equivalent state rather than a pathway leading to $O_2$ release. The core chemical issue is thus not merely water activation, but the management of oxygen-centered valence accumulation. If oxidation proceeds too weakly, the first oxygen-centered reactive state does not form efficiently and peroxide generation remains kinetically inaccessible. If oxidation proceeds too strongly or the surface stabilizes highly oxidized oxygen intermediates too effectively, the catalytic sequence is redirected toward the four-electron oxygen evolution manifold, where O-O coupling is followed by further oxidation and $O_2$ liberation. In this sense, the two-electron water oxidation reaction is best understood as a selective oxygen-coupling process that must arrest at a metastable oxidation level. This gives the reaction exceptional conceptual value within two-electron electrocatalysis. It demonstrates that selective redox synthesis is not limited to suppressing excessive reduction of a bound intermediate, but can also require suppression of excessive oxidation after bond formation has already occurred. It further reveals that $H_2O_2$ can be approached from both sides of the oxygen redox landscape, cathodically from $O_2$ and anodically from $H_2O$, yet the chemical logic of selectivity is reversed in the two cases. For this reason, two-electron water oxidation has emerged as one of the most demanding and informative systems in selective electrosynthesis, because it condenses into a single anodic transformation the broader problem of how an electrified interface can generate a high-energy oxygenated molecule directly from water while resisting the natural thermodynamic tendency toward complete oxygen evolution[253].

The two-electron water oxidation reaction provides an anodic route for $H_2O_2$ synthesis that differs from cathodic oxygen reduction reaction. Compared with oxygen reduction, which depends on $O_2$ solubility and mass transfer, the two-electron water oxidation reaction uses water or $OH^-$ as the reactant and therefore has distinct advantages in oxygen-deficient environments and anodic product-coupled systems[254,255]. However, water oxidation usually tends to proceed through the four-electron oxygen evolution reaction pathway, and the generated $H_2O_2$ may be further oxidized or decomposed at high potentials. Therefore, promoting O-O bond formation, suppressing oxygen evolution reaction competition, and stabilizing peroxide species are central issues in the two-electron water oxidation reaction catalyst design. Kim *et al.*[256] reported oxygen-deficient $Pr_{1.0}Sr_{1.0}Fe_{0.75}Zn_{0.25}O_4$-δ (D-PSFZ) perovskite oxides for $H_2O_2$ electrosynthesis under high ionic strength. The optimized configurations of RP-PSFZ first show the distribution of Fe and Zn sites in the Ruddlesden-Popper perovskite framework, providing a structural basis for understanding Zn substitution and oxygen-defect regulation [Figure 12A]. The atomic-scale HAADF-STEM image of D-PSFZ along the <100> zone axis further displays the ordered atomic arrangement of the oxide, confirming its layered lattice structure and stable cation ordering [Figure 12B]. At the mechanistic level, the schematic of $H_2O_2$ generation on the PSF surface presents both the oxygen reduction pathway and the water oxidation pathway; the water oxidation reaction pathway relevant to this section shows the transformation among HO*, O*, and HOO* intermediates during water oxidation, indicating that oxygen defects can tune oxygenated-intermediate adsorption and enhance $H_2O_2$ selectivity [Figure 12C]. The water oxidation reaction polarization profiles of D-PSFZ in $KHCO_3$ solutions with concentrations ranging from 0.1 to 2.0 M and saturated $KHCO_3$, together with the corresponding Faradaic efficiencies, further demonstrate anodic $H_2O_2$ generation and concentration-/potential-dependent selectivity [Figure 12D][256]. This system shows that oxygen-deficient perovskites can regulate not only cathodic the two-electron oxygen reduction reaction but also anodic the two-electron water oxidation reaction by modulating water-oxidation intermediate adsorption. Different

from electrochemical anodic water oxidation, Zhang *et al.*[257] reported Sn-vacancy-rich SnSe nanosheets that produce $H_2O_2$ from $H_2O$ and $O_2$ under mild thermocatalytic conditions. The side views of the optimized $H_2O$* and H*-OH* structures on SnSe, VSn, and $V_2$Sn show how water adsorbs and initially dissociates in different Sn-vacancy environments, suggesting that Sn vacancies substantially change the activation state of water molecules [Figure 12E]. The high-resolution HAADF-STEM image of the lattice along the [001] axis further shows the atomic-column arrangement and local lattice features of SnSe nanosheets, providing structural evidence for the involvement of Sn vacancies [Figure 12F]. The free-energy diagram of $H_2O_2$ production shows that Sn-vacancy-containing surfaces can lower the barriers for water dissociation and subsequent peroxide-species formation; the inset further illustrates local surface reconstruction through VSn migration, which facilitates $H_2O_2$ release [Figure 12G]. The schematic diagram of thermocatalytic $H_2O_2$ production from $H_2O$ and $O_2$ over SnSe with Sn vacancies links water dissociation, $O_2$ activation, OH* transformation, and $H_2O_2$ desorption, showing that vacancy-induced water activation and surface reconstruction can drive $H_2O_2$ formation in the $H_2O/O_2$ system [Figure 12H][257].

For externally driven water-oxidation systems, Xu *et al.*[258] constructed a $Fe^{3+}$/$BiOIO_3$ (BIO) piezo-self-Fenton system that couples two-electron water oxidation for $H_2O_2$ production with $Fe^{3+}$ reduction. The crystal structure of BIO along the b-c planes shows its non-centrosymmetric structure and polarization direction, providing the structural premise for force-induced piezo-potential, charge separation, and water oxidation [Figure 12I]. The corresponding inverse fast fourier transform (FFT) patterns of BIO further present the ordered lattice arrangement, confirming the crystalline integrity of the nanosheets and supporting their piezoelectric response [Figure 12J]. From the reaction-energy perspective, the free-energy diagram for two-electron and four-electron water oxidation reaction compares different water-oxidation pathways, indicating that piezoelectric driving can alter intermediate conversion and help redirect water oxidation from competitive four-electron oxygen evolution reaction toward $H_2O_2$ formation [Figure 12K]. The J-V curves of BIO in different systems show that the $H_2O$ oxidation current response is enhanced when ultrasound and Fe(III) coexist, suggesting that $Fe^{3+}$ and the piezoelectric field jointly promote the two-electron water oxidation reaction-derived $H_2O_2$ production and the $Fe^{3+}/Fe^{2+}$ cycle [Figure 12L][258]. This system does not simply aim to accumulate $H_2O_2$, but uses *in situ* generated $H_2O_2$ to drive the subsequent Fenton reaction for pollutant degradation. Li *et al.*[259] further developed a $ZnGa_2O_4$ anode and proposed a dual-active-site mechanism for the two-electron water oxidation reaction. The side and top views of *OH adsorption on $ZnGa_2O_4$ show that *OH can bind simultaneously with Zn and Ga sites, providing a structural basis for the direct $OH^-$-mediated water oxidation pathway [Figure 12M]. The HRTEM image and polycrystalline electron diffraction pattern of $ZnGa_2O_4$ confirm the crystallinity and polycrystalline characteristics of the spinel oxide, supporting its use as a stable anode material [Figure 12N]. The real-time $H_2O_2$ concentration curves at 2.3, 2.5, and 2.7 V *vs.* RHE show continuous product accumulation, while also reflecting the competition between $H_2O_2$ generation and decomposition at higher potentials [Figure 12O]. The proposed reaction scheme further indicates that $H_2O_2$ generation on $ZnGa_2O_4$ proceeds through both a direct $OH^-$-mediated pathway and an indirect $HCO_3^-/HCO_4^-$-mediated pathway, where Ga-Ga dual sites facilitate percarbonate intermediate formation and Zn/Ga dual sites help stabilize peroxide bonds and suppress $H_2O_2$ decomposition [Figure 12P][259].

### Two-electron carbon dioxide reduction reaction

The two-electron carbon dioxide reduction reaction occupies a distinctive position within selective electrosynthesis because it converts a highly oxidized and thermodynamically stable carbon source into an oxygen-retaining reduced product without entering the more complex multielectron manifolds associated with deep deoxygenation and C-C coupling[260,261]. In its most representative form, the cathodic half-reaction is written as $CO_2 + 2H^+ + 2e^- \rightarrow HCOOH$ in acidic media or $CO_2 + H_2O + 2e^- \rightarrow HCOO^- + OH^-$ under alkaline conditions, with the observed product speciation dictated by interfacial acid-base equilibrium. The chemical

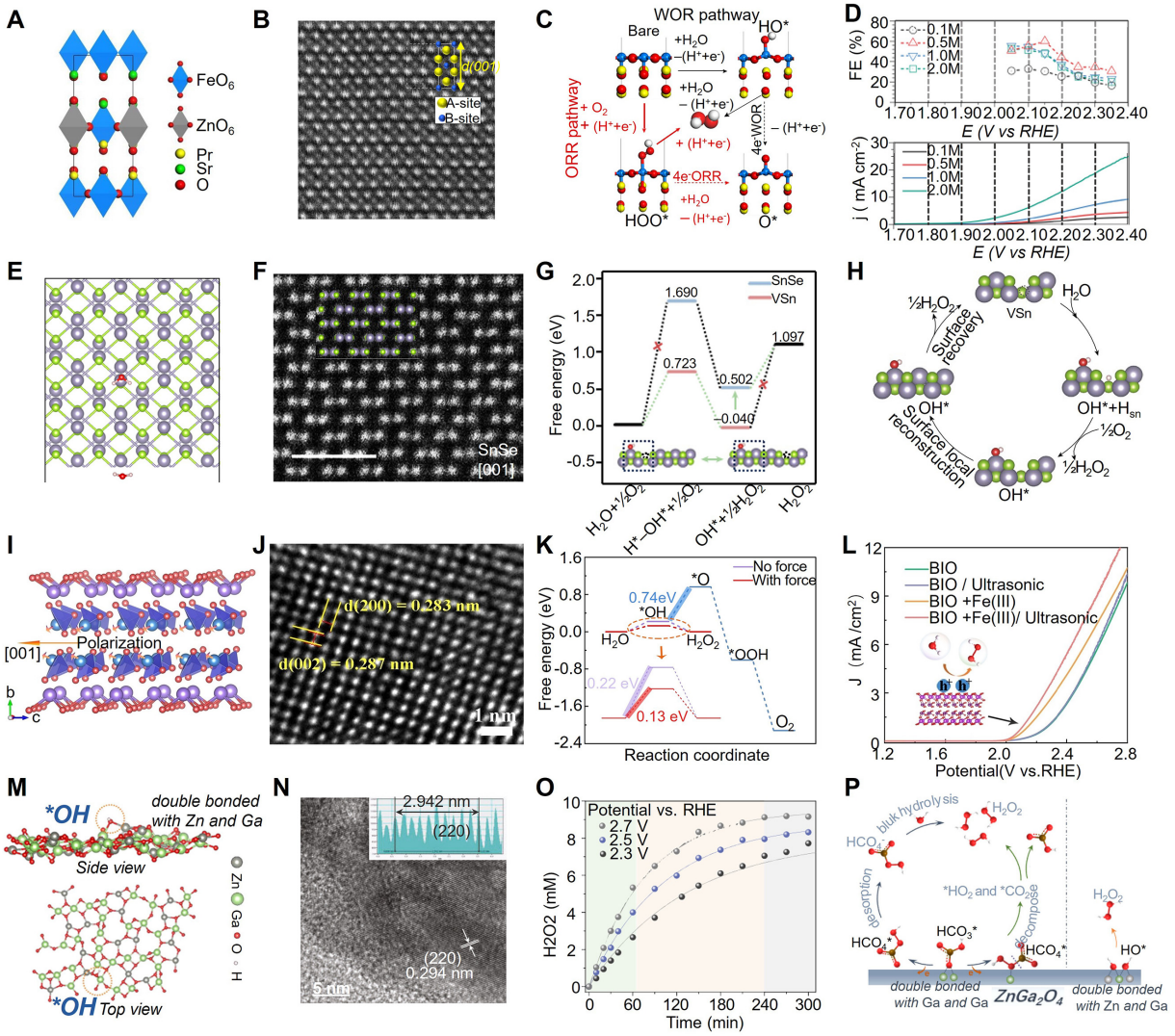



**Figure 12.** (A) Optimized configurations of RP-PSFZ; blue and gray octahedra represent Fe and Zn sites, while yellow, green, and red spheres represent Pr, Sr, and O atoms, respectively. (B) Atomic-scale HAADF-STEM image of D-PSFZ along the <100> zone axis. (C) Schematic of the $H_2O_2$ generation mechanism on the PSF surface through oxygen reduction (red arrow) and water oxidation reaction (black arrow); blue, yellow, red, and white spheres represent Fe, Pr, O, and H atoms, respectively. (D) Water oxidation reaction polarization profiles of D-PSFZ at various solution concentrations of 0.1-2.0 M and saturated $KHCO_3$ solution (lower part) and the corresponding Faradaic efficiencies determined by the titration method (upper part). (A-D) is reprinted with permission from Ref.[256]. Copyright © 2023 Springer Nature. (E) Side views of optimized $H_2O^*$ and H*-OH* structures on SnSe, VSn, and $V_2Sn$. (F) High-resolution HAADF-STEM image of the SnSe lattice along the [001] axis, with superimposed Sn and Se atoms at each atomic column. (G) Free-energy diagram of $H_2O_2$ production; the inset shows local surface reconstruction through VSn migration, where the dashed black circles represent VSn. (H) Schematic diagram of thermocatalytic $H_2O_2$ production from $H_2O$ and $O_2$ over the surface of SnSe with Sn vacancies. (E-H) is reprinted with permission from Ref.[257]. Copyright © 2025 Springer Nature. (I) Crystal structure of BIO along the b-c planes; red, purple, and blue represent O, Bi, and I atoms, respectively, and orange arrows indicate the polarization direction. (J) Corresponding inverse FFT patterns of BIO. (K) Free-energy diagram for two-electron and four-electron water oxidation reaction. (L) J-V curves of BIO in different systems under positive sweep for $H_2O$ oxidation; red and white spheres represent O and H atoms, respectively. (I-L) is reprinted with permission from Ref.[258]. Copyright © 2023 Wiley-VCH GmbH. (M) Side and top views of *OH adsorption on $ZnGa_2O_4$. (N) HRTEM image and polycrystalline electron diffraction pattern of $ZnGa_2O_4$. (O) Real-time$H_2O_2$ concentration as a function of time at 2.3, 2.5, and 2.7 V *vs.* RHE; the solid lines are fitting curves. (P) Schematic illustration of the proposed direct and indirect pathways toward $H_2O_2$ generation on the $ZnGa_2O_4$ surface. (M-P) is reprinted with permission from Ref.[259]. Copyright © 2023 Springer Nature.

significance of this transformation lies in the fact that the carbon center undergoes a discrete reduction event while preserving its one-carbon framework and substantial oxygen functionality, thereby generating a liquid

carbon product that remains chemically differentiated from both CO and more deeply reduced hydrocarbons or alcohols[262-264]. This feature makes the reaction fundamentally different from oxygen-related two-electron chemistry. There, the challenge is centered on peroxide-level oxygen redox control, whereas here the central issue is selective carbon-centered reduction coupled with oxygen retention[265,266]. At the molecular level, $CO_2$ reduction begins from a linear closed-shell molecule whose activation requires bending of the O=C=O geometry, redistribution of electron density into antibonding orbitals, and interfacial stabilization of a highly reactive adsorbate-derived state. The two-electron pathway is realized only when this activated state is directed toward a formate-level product manifold rather than toward decarbonylation-type chemistry or deeper proton-coupled reduction. This makes the reaction a stringent test of chemoselective carbon-oxygen bond management. The catalyst must provide enough interfacial driving force to overcome the intrinsic inertness of $CO_2$, yet it must not impose a binding environment that excessively favors C-O bond weakening, surface poisoning by carbonaceous intermediates, or diversion into multielectron pathways[267-269]. The chemical problem is therefore not simply the reduction of carbon dioxide, but the selective accumulation of two reducing equivalents at a stage where partial reduction itself is the desired endpoint. This requirement gives the two-electron carbon dioxide reduction reaction exceptional conceptual value. It demonstrates that electrocatalytic efficiency cannot be judged solely by how far carbon is reduced, because the synthetically meaningful outcome may instead depend on halting the reaction at an oxidation state that preserves functional oxygen chemistry while creating a transportable and chemically useful carbon product. In this sense, the reaction serves as one of the clearest examples of oxidation-state-defined carbon electrosynthesis, where the core objective is not maximal electron delivery to carbon, but precise interfacial control over how much reduction occurs, where it is localized, and when the partially reduced product is released before further chemical descent becomes dominant.

The two-electron carbon dioxide reduction reaction toward formic acid/formate ($HCOOH/HCOO^-$) represents a typical selective partial-reduction process, in which the central objective is to direct activated $CO_2$ along an oxygen-retaining pathway and release the target product at the two-electron stage, rather than allowing further deep reduction, C-C coupling, or competitive hydrogen evolution. For $CO_2$-to-$HCOOH/HCOO^-$ conversion, the formation and stabilization of OCHO or HCOO intermediates are particularly important. Meanwhile, interfacial water activation, proton sources, and proton-coupled electron transfer kinetics directly influence formic acid/formate production. Ling *et al.*[211] developed an $In_2O_3/SnO_2$@rGO-2 composite oxide catalyst, in which the interfacial synergy between$In_2O_3$ and $SnO_2$ regulates the electronic structure of Sn-based active sites and promotes acidic $CO_2$-to-HCOOH conversion. The charge-density diagram of $In_2O_3/SnO_2$@rGO-2 shows pronounced interfacial charge redistribution between $In_2O_3$ and $SnO_2$, indicating that $In_2O_3$ incorporation modifies the local electronic environment of the $SnO_2$ surface and provides more favorable active sites for $CO_2$ activation and subsequent proton-coupled electron transfer [Figure 13A]. The TEM image further displays clear lattice fringes in $In_2O_3/SnO_2$@rGO-2, where spacings of 0.33 and 0.26 nm correspond to $SnO_2$ planes, while 0.29 nm corresponds to $In_2O_3$, confirming the successful formation of the composite oxide interface [Figure 13B]. The corresponding Gibbs free-energy profile for $CO_2$-to-HCOOH conversion shows that, compared with $SnO_2$@rGO, $In_2O_3/SnO_2$@rGO-2 substantially optimizes the formic acid formation pathway by lowering the energetic barriers for *OCHO formation and subsequent transformation, thus directing the reaction toward HCOOH production [Figure 13C][211]. This catalyst achieves a HCOOH Faradaic efficiency of approximately 98.3% at 700 mA $cm^{-2}$ in a pH 1 acidic electrolyte and operates stably for a long duration in an membrane electrode assembly system, demonstrating the synergistic role of the composite oxide interface, water activation, and *OCHO stabilization. In parallel with this oxide-interface strategy, Shi *et al.*[212] reported Li-doped bismuth oxycarbonate (BOC-Li), revealing how alkali-metal incorporation enhances the $CO_2$-to-formate pathway by improving proton-electron transfer kinetics. The structural model of the $Bi_2O_2CO_3$ (161) surface displays $Li_4c$ and $Li_3c$ doping configurations and their optimized adsorption structures, indicating that trace Li doping

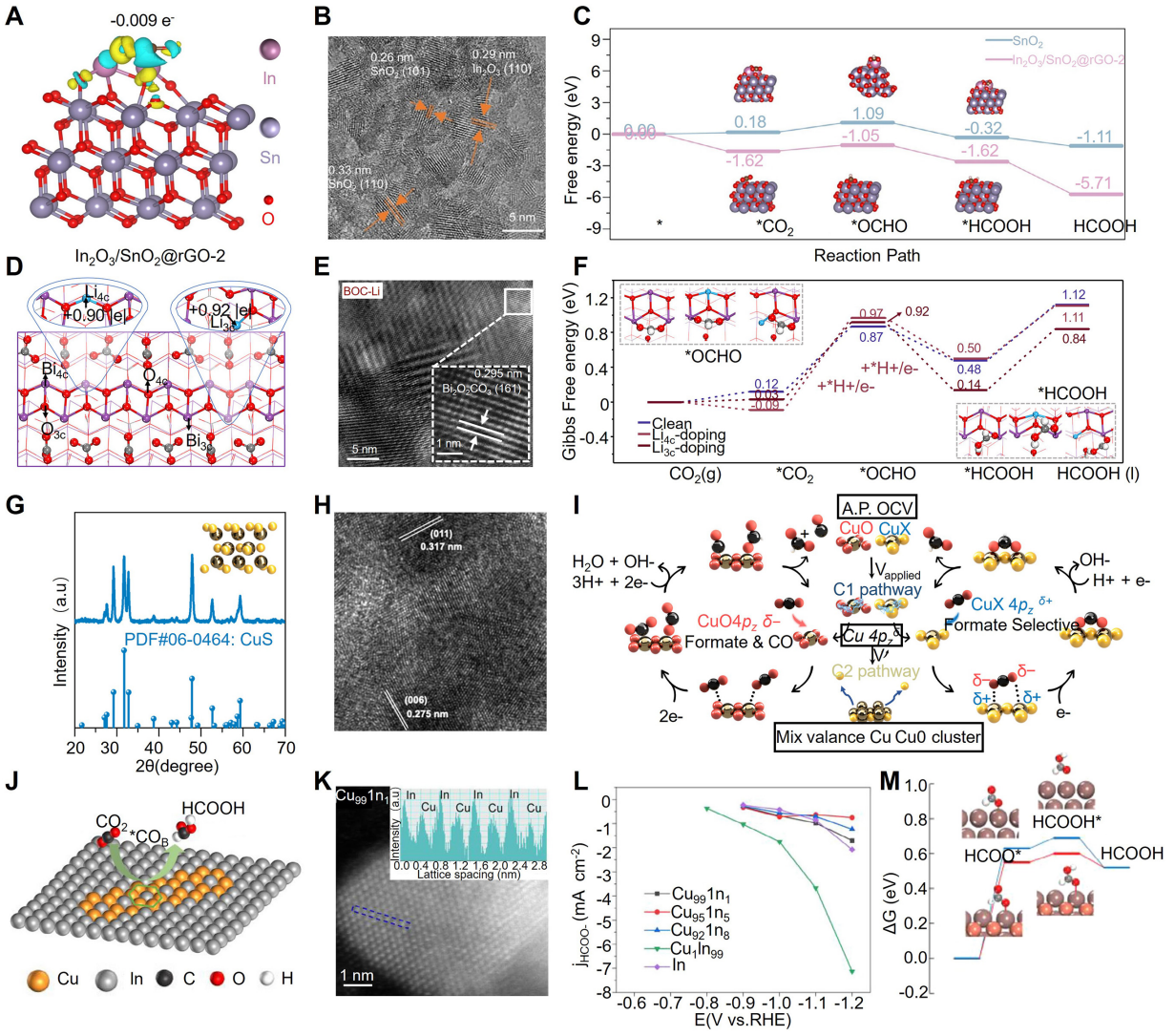



**Figure 13.** (A) Charge-density diagram of $In_2O_3/SnO_2$@rGO-2, showing interfacial charge redistribution between$In_2O_3$ and $SnO_2$. (B) TEM image of $In_2O_3/SnO_2$@rGO-2. (C) Gibbs free-energy profile for $CO_2$-to-HCOOH conversion over $SnO_2$@rGO and $In_2O_3/SnO_2$@rGO-2. (A-C) is reprinted with permission from Ref.[211]. Copyright © 2025 Wiley-VCH GmbH. (D) Structure of the $Bi_2O_2CO_3$ (161) surface with $Li_{4c}$ and $Li_{3c}$ doping sites and the optimized adsorption structure. (E) HRTEM image of BOC-Li revealing lattice distortions and dislocations. (F) Free-energy diagrams for HCOOH formation via the *OCHO mechanism. Purple, Bi; red, O; white, H; grey, C; light blue, Li. These color notations are used throughout the paper. (D-F) is reprinted with permission from Ref.[212]. Copyright © 2026 Springer Nature (G) XRD pattern of CuS. (H) HR-TEM image of CuS after catalysis at -0.6 V *vs.* RHE with 85% iR correction. (*i*, current; *R*, solution resistance) (I) Proposed carbon dioxide reduction reaction mechanism over copper-based electrocatalysts for multiple reduction products and selective reduction to formate. (G-I) is reprinted with permission from Ref.[210]. Copyright © 2025 Springer Nature. (J) Schematic illustration of $CO_2$ conversion on $Cu_1In_{99}$ catalysts. (K) HAADF-STEM image of the as-prepared $Cu_1In_{99}$ catalyst. The inset shows the line profile for HAADF intensity analysis of the blue dashed region. (L) Partial current densities of $HCOO^-$ over $Cu_{99}In_1$, $Cu_{95}In_5$, $Cu_{92}In_8$, $Cu_1In_{99}$, and In catalysts. (M) Comparison of Gibbs free-energy profiles for electrochemical $CO_2$ reduction to HCOOH on In and alloy CuIn under standard hydrogen electrode conditions. Orange, Cu; brown, In; grey, C; white, H; red, O. (J-M) is reprinted with permission from Ref.[270]. Copyright © 2025 Wiley-VCH GmbH.

changes the local coordination environment around Bi sites and modifies reactant adsorption [Figure 13D]. The HRTEM image of BOC-Li shows that the $Bi_2O_2CO_3$ (161) lattice plane is retained, while obvious lattice distortions and dislocations appear, suggesting that Li incorporation perturbs the local lattice structure and generates more active Bi sites [Figure 13E]. The free-energy diagram for HCOOH formation via the *OCHO mechanism further shows that Li-doped $Bi_2O_2CO_3$ surfaces lower the energy barrier for HCOOH production; in particular, $Li_{3c}$-related structures facilitate $H_2O/CO_2$ adsorption and O-H activation, thereby improving proton supply and *OCHO conversion [Figure 13F][212]. Combined operando NMR, kinetic isotope effect, Tafel analysis, and *in situ* ATR-SEIRAS results demonstrate that Li doping enhances concerted proton-electron transfer at Bi active sites and markedly improves formate selectivity.

From the perspective of Cu-based catalysts, Tian *et al.*[210] showed that CuS chalcogenides can redirect conventionally nonselective Cu-based carbon dioxide reduction reaction toward selective formate generation through anion-induced electronic modulation. The X-ray diffraction (XRD) pattern of CuS matches the standard CuS crystalline phase, confirming the well-defined chalcogenide structure and providing a structural basis for Cu-S interactions and electronic regulation of Cu sites [Figure 13G]. The HR-TEM image of CuS after electrolysis at -0.6 V *vs.* RHE further shows that the catalyst retains clear lattice features, indicating good structural stability under carbon dioxide reduction reaction conditions and preservation of the Cu-S coordination environment [Figure 13H]. The proposed carbon dioxide reduction reaction mechanism indicates that Cu-S interactions stabilize $Cu^{\delta+}$ sites and prevent their complete reduction to $Cu^{0}$. Meanwhile, Cu 4p orbital charge redistribution enhances the affinity of Cu sites for O-end adsorption, favoring the formation of Cu-OCHO* intermediates and ultimately steering the reaction toward $HCOO^-$ production [Figure 13I][210]. Operando X-ray absorption spectroscopy (XAS), HERFD-XAS, Raman, and IR analyses further confirm that chalcogen-induced structural stabilization and charge redistribution are responsible for the high formate selectivity of CuS. Du *et al.*[270] further demonstrated that tuning the metal environment around Cu sites in Cu-In single-atom alloys can also enhance the $CO_2$-to-HCOOH pathway. The schematic illustration of $CO_2$ conversion on $Cu_1In_{99}$ shows that when a small amount of Cu is incorporated into an In matrix, the Cu sites are embedded in an In-rich environment, and their adsorption properties are strongly regulated by neighboring In atoms, favoring oxygenated intermediate formation and HCOOH production [Figure 13J]. The HAADF-STEM image of $Cu_1In_{99}$ and the corresponding line profile from the blue dashed region reveal a specific atomic arrangement of Cu and In, confirming the single-atom alloy/alloy-phase structural features of the catalyst [Figure 13K]. The comparison of $HCOO^-$ partial current densities shows that $Cu_1In_{99}$ exhibits a higher $HCOO^-$ production capability than $Cu_{99}In_1$, $Cu_{95}In_5$, $Cu_{92}In_8$, and pure In, demonstrating that Cu sites in an In-rich host environment significantly enhance the $CO_2$-to-formate pathway [Figure 13L]. The Gibbs free-energy profile for $CO_2$ reduction to HCOOH further shows that, compared with pure In, the CuIn alloy surface provides a more favorable energetic pathway for HCOOH formation by stabilizing HCOO*-related intermediates and lowering the subsequent reaction barrier [Figure 13M][270].

### Two-electron nitrate reduction reaction

The two-electron nitrate reduction reaction represents one of the most chemically nuanced forms of selective electrocatalysis because it targets the controlled conversion of a highly oxidized nitrogen-oxoanion into nitrite without allowing the system to proceed into the far more extensive reduction chemistry that leads to NO, $N_2O$, $NH_2OH$, $NH_3$, or $N_2$. In acidic medium, the overall two-electron step can be expressed as $NO_3^- + 2H^+ + 2e^- \rightarrow NO_2^- + H_2O$, whereas in alkaline solution it is more appropriately written as $NO_3^- + H_2O + 2e^- \rightarrow NO_2^- + 2OH^-$. This reaction is chemically distinctive because it is neither a simple electron-transfer event nor a full denitrification process. Rather, it is a selective oxyanion-editing transformation in which one oxygen atom is effectively removed from the nitrate framework while the nitrogen center remains in an oxoanion environment. Such a transformation occupies the first decisive reduction threshold in the broader electrochemical nitrogen cycle, and its significance lies precisely in the fact that nitrite is both a mechanistically meaningful intermediate and, under selective conditions, a chemically defined product[271-273]. The molecular challenge begins with the strong N-O bonding network and high oxidation state of nitrate, both of which make initial activation at the electrode interface intrinsically demanding. Productive conversion requires sufficient interfacial interaction to polarize the oxyanion, reorganize charge density around nitrogen, and enable the first deoxygenation step through coupled proton-electron transfer. Yet this same activation immediately places the system on a densely connected nitrogen redox landscape in which partially reduced species are often even more susceptible to further transformation than the parent nitrate. The two-electron nitrate reduction reaction is therefore best understood as a selective decoupling problem. The catalyst must activate nitrate enough to cross the first reduction barrier, but it must also release nitrite

rapidly enough to prevent continued hydrogenation or further oxygen removal. This requirement makes the reaction especially informative in conceptual terms[274-276]. Unlike oxygen reduction, where selectivity is governed by preservation or cleavage of an O-O unit, or carbon dioxide reduction, where the central issue is controlled partial reduction of a carbon-oxygen framework, nitrate reduction is defined by selective editing of N-O connectivity within a multistage nitrogen valence ladder. The relevant chemical objective is not maximal reduction of nitrogen, but precise control over how far the nitrogen center is permitted to descend along that ladder under electrochemical conditions. For this reason, the two-electron nitrate reduction reaction provides a particularly stringent model for oxidation-state-specific inorganic synthesis. It highlights the fact that selective electrocatalysis often depends less on reaching the lowest-energy nitrogen product than on imposing a chemically disciplined stopping point within a reaction manifold that is intrinsically prone to overreduction once the first oxyanion activation event has occurred.

The two-electron nitrate reduction reaction generally refers to the selective conversion of $NO_3^-$ to $NO_2^-$, which is the initial key step in the nitrate electroreduction network. Since $NO_2^-$ is an intermediate-valence nitrogen species, it can be further hydrogenated to $NH_3$, $N_2$, or other deeply reduced products once formed. Therefore, the central challenge of the two-electron nitrate reduction reaction is not merely to activate $NO_3^-$, but to promote $*NO_3$-to-$*NO_2$ conversion while enabling $NO_2^-$ desorption and suppressing further reduction. Murphy *et al.*[277] systematically investigated a series of atomically dispersed M-N-C catalysts for nitrate reduction reaction and $NO_2^-$ reduction reaction, providing mechanistic insight into how single-atom sites regulate the $NO_3^- \rightarrow NO_2^-$ pathway. The charge-density-difference map of Br-Cu reveals pronounced electronic redistribution around the Br-modified Cu sites, with a calculated charge transfer of approximately 0.67 |e|, indicating strong electronic interaction induced by Br incorporation [Figure 14A]. The HRTEM image further shows well-resolved lattice fringes with spacings of 2.08 and 1.80 Å, corresponding to the Cu(111) and Cu(200) planes, respectively, confirming the preserved crystalline Cu framework after interfacial modification [Figure 14B]. The calculated free-energy profiles for nitrate reduction subsequently compare the reaction energetics over Br–Cu and Cu/$Cu_2O$, revealing distinct energy landscapes for the initial two-electron conversion and the subsequent six-electron reduction toward $NH_3$. These results indicate that Br-induced electronic regulation alters the energetics of nitrate-derived intermediates and thereby modulates the overall nitrate-to-ammonia pathway [Figure 14C][277]. Moving from intrinsic active-site thermodynamics to reaction-sequence control, Jiang *et al.*[278] demonstrated that separating nitrate reduction reaction into $NO_3^- \rightarrow NO_2^-$ and $NO_2^- \rightarrow NH_3$ stages can reduce the overall kinetic barrier. The atomistic structure scheme for $NO_3^-$ electroreduction to $NO_2^-$ on the $Cu_2O$ (111) lattice plane illustrates $NO_3^-$ adsorption, N-O bond activation, and $NO_2^-$ formation, providing a model basis for understanding the two-electron nitrate reduction pathway on Cu-based surfaces [Figure 14D]. TEM and HRTEM images of Cu-RD-PBS show a nanowire-derived morphology and expose Cu (111) and $Cu_2O$ (111) facets, indicating that metallic Cu and cuprous oxide-related structures coexist after reduction treatment [Figure 14E]. The free-energy comparison further shows the energetic evolution of nitrate-derived intermediates over Cu (111) and $Cu_2O$ (111), highlighting the importance of suitable Cu-based facets for $*NO_3$/$*NO_2$ formation [Figure 14F]. The Faradaic efficiency for $NO_3^-$ reduction to $NO_2^-$ demonstrates that the Cu nanowire system can achieve high nitrite formation efficiency at suitable potentials, confirming that regulating the $NO_3^- \rightarrow NO_2^-$ step as an independent two-electron stage improves nitrate reduction efficiency and selectivity [Figure 14G][278].

Once the $NO_3^- \rightarrow NO_2^-$ step is treated as a controllable two-electron stage, catalyst design can further focus on accelerating $NO_2^-$ release and suppressing its subsequent hydrogenation under practical electrolysis conditions. Li *et al.*[219] developed an Ag nanowire membrane electrode that confines nitrate reduction to a highly selective two-electron $NO_3^- \rightarrow NO_2^-$ conversion stage. The structural schematic of Ag nanowires displays the distribution of facets, edge sites, and corner sites, indicating that high-curvature metallic nanostructures provide abundant reactive sites and facilitate $NO_3^-$ adsorption and electron transfer

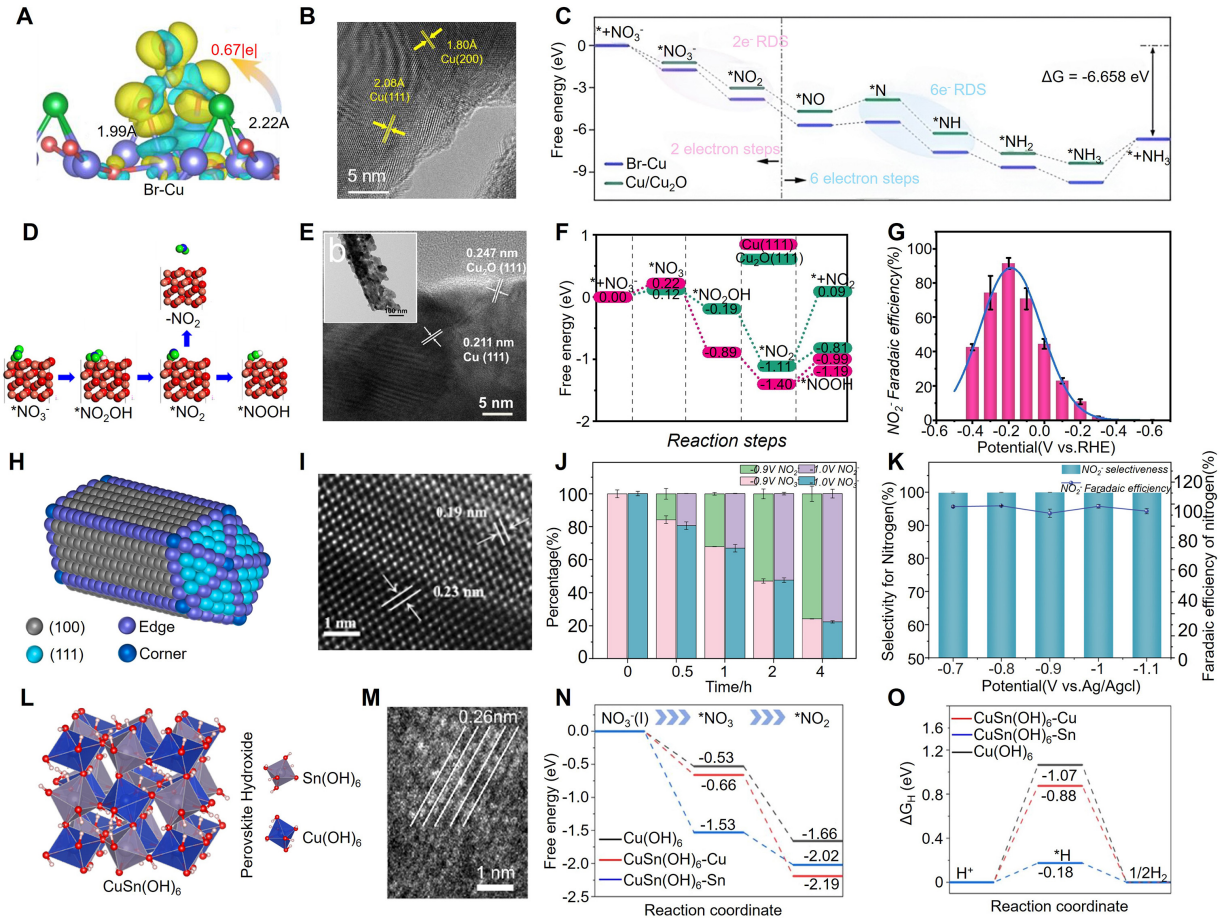



**Figure 14.** (A) Calculated charge-density-difference map of Br-Cu, showing interfacial charge redistribution and charge transfer. (B) HRTEM image showing lattice fringes assigned to Cu(111) and Cu(200), with spacings of 2.08 and 1.80 Å, respectively. (C) Calculated free-energy profiles for nitrate reduction on Br–Cu and Cu/$Cu_2O$, highlighting the two-electron and six-electron rate-determining steps toward $NH_3$ formation. (A-C) is reprinted with permission from Ref.[277]. Copyright ©2023 Springer Nature. (D) Atomistic structure scheme showing the reaction pathway for electrochemical reduction of $NO_3^-$ to $NO_2^-$ on the $Cu_2O$ (111) lattice plane. (E) Morphology characterization of Cu-RD-PBS, including TEM and HRTEM images. (F) Comparison of the free-energy diagrams for $NO_3^-$ reduction over Cu-based surfaces. (G) Faradaic efficiency for the reduction of $NO_3^-$ to $NO_2^-$. (D-G) is reprinted with permission from Ref.[278]. Copyright © 2023 Wiley-VCH GmbH. (H) Structural schematic of Ag nanowires. (I) HRTEM image of Ag nanowires, showing clear lattice fringes. (J) Ratios of nitrate and nitrite at different electrolysis times at - 0.9 and -1.0 V *vs.* Ag/AgCl. (K) Nitrite selectivity and Faradaic efficiency in the electrolysis of 100 mM nitrate solutions. (H-K) is reprinted with permission from Ref.[219]. Copyright © 2024 Elsevier B.V. (L) Crystal structure of the perovskite hydroxide $CuSn(OH)_6$. (M) High-resolution TEM image of $CuSn(OH)_6$. (N) Free energies of $NO_3^-$ and $NO_2$ adsorption on $Cu(OH)_2$ and $CuSn(OH)_6$. (O) ΔG_H values of $Cu(OH)_2$ and $CuSn(OH)_6$. (L-O) is reprinted with permission from Ref.[213]. Copyright © 2025 Wiley-VCH GmbH.

[Figure 14H]. The HRTEM image further shows clear lattice fringes of Ag nanowires, confirming their stable metallic Ag crystal structure [Figure 14I]. The ratios of nitrate and nitrite at different electrolysis times at -0.9 and -1.0 V *vs.* Ag/AgCl show that $NO_3^-$ can be continuously converted to $NO_2^-$ and that nitrite accumulates as the main product [Figure 14J]. Electrolysis in 100 mM nitrate solutions further demonstrates high nitrite selectivity and Faradaic efficiency, indicating that the Ag nanowire membrane electrode enhances mass transport and promotes $NO_2^-$ desorption, thereby reducing the probability of further hydrogenation to $NH_3$ [Figure 14K][219]. While the Ag nanowire membrane electrode mainly relies on metallic nanostructure and mass-transport regulation to release $NO_2^-$, Chen *et al.*[213] reported perovskite hydroxide $CuSn(OH)_6$, where cooperative bimetallic sites and structural stability restrict deep reduction. The crystal structure of

$CuSn(OH)_6$ shows alternating $Cu(OH)_6$ and $Sn(OH)_6$ octahedra, forming a cooperative interface for nitrate adsorption and conversion [Figure 14L]. The high-resolution TEM image displays clear lattice fringes, confirming that $CuSn(OH)_6$ maintains a stable crystalline structure during catalysis [Figure 14M]. The adsorption free energies of $NO_3^-$ and $NO_2$ on $Cu(OH)_2$ and $CuSn(OH)_6$ indicate that $NO_3^-$ adsorption is more favorable on the Sn sites of $CuSn(OH)_6$, while subsequent conversion is closely related to Cu sites. This suggests that Sn sites preferentially capture $NO_3^-$ and Cu sites promote the $NO_3^- \rightarrow NO_2^-$ transformation [Figure 14N]. The $\Delta G_H$ values of $Cu(OH)_2$ and $CuSn(OH)_6$ further show that $CuSn(OH)_6$ has weaker hydrogen adsorption, which helps suppress over-hydrogenation and the further reduction of $NO_2^-$ [Figure 14O][213].

### Two-electron halide oxidation reaction

The two-electron halide oxidation reaction provides the anodic counterpart to selective partial redox synthesis in which a halide anion is converted into a molecular halogen through a chemically discrete two-electron process. This reaction class is conceptually important because it shows that two-electron electrocatalysis is not restricted to cathodic partial reduction, but also encompasses oxidation reactions in which the desired product is defined by controlled valence increase and selective covalent bond formation. In chemical terms, the key event is the removal of electrons from halide-derived interfacial species followed by X-X coupling and molecular halogen release. The challenge, however, is not simply to oxidize halides, since many halides are electrochemically accessible substrates under anodic bias. The true selectivity problem lies in directing oxidizing equivalents toward substrate-centered halogen formation rather than toward solvent- or hydroxide-derived oxygen evolution. This makes the two-electron halide oxidation reaction a stringent test of anodic charge partitioning. The catalytic interface must recognize halide oxidation as the preferred molecular synthesis channel even in an electrochemical environment where oxygen-centered oxidation pathways are inherently available and often become increasingly competitive at elevated potentials[279-281]. From a mechanistic perspective, the reaction is governed by the balance between halide adsorption, interfacial electron withdrawal, and the kinetics of halogen-coupled bond formation. If the interaction with halide is too weak, substrate capture and interfacial oxidation become inefficient. If the surface instead accumulates highly oxidizing oxygenated states too readily, the reaction network shifts away from halogen evolution and into the four-electron oxygen evolution regime. The two-electron halide oxidation reaction is therefore best understood as a selective anodic molecular coupling process in which the catalytic surface must convert halide-centered oxidation into a product-defining X-X bond before competing oxygen chemistry consumes the applied potential. This gives the reaction a distinctive place within two-electron electrocatalysis. It demonstrates that selectivity at a prescribed electron count can also be achieved on the oxidative side of electrochemistry, where the objective is not to halt reduction at an intermediate state, but to prevent the anodic interface from escalating into a more strongly oxidizing manifold than is chemically required for the desired product[282]. For this reason, halide oxidation offers a particularly clean and revealing model for understanding how selective inorganic electrosynthesis can be achieved under anodic conditions through precise control over substrate-centered oxidation, bond formation, and competition with solvent-derived overoxidation.

Halide redox reactions represent an important class of two-electron electrochemical processes in energy conversion, disinfectant production, and halogen-based battery systems. Representative examples include chloride oxidation to $Cl_2$/active chlorine and bromide-based $Br^-/Br^+$ conversion[283,284]. Compared with competing processes such as oxygen evolution, halogen shuttling, and electrode corrosion, efficient halide redox chemistry requires selective halide adsorption, stabilization of key intermediates, and rapid product release at the electrode interface[285,286]. Zhao *et al*.[215] reported an Fe-doped $Ti_4O_7$ anode for efficient active chlorine electrosynthesis from natural seawater. The atomic structure model of Fe-$Ti_4O_7$ shows that Fe incorporation modifies the local metal-oxygen coordination environment of $Ti_4O_7$ and strengthens the

electrophilicity of lattice oxygen, thereby facilitating site-selective $Cl^-$ activation [Figure 15A]. The HRTEM image further displays clear lattice fringes with a spacing of approximately 0.337 nm, corresponding to the $Ti_4O_7$ (120) plane, indicating that Fe doping preserves the Magnéli-phase $Ti_4O_7$ crystal structure [Figure 15B]. From an energetic perspective, the chlorine evolution reaction can proceed through either the Volmer-Tafel or Volmer-Heyrovsky pathway, and the Gibbs free-energy diagram on Fe-$Ti_4O_7$ shows that *Cl formation and subsequent $Cl_2$ generation are key steps controlling chlorine evolution reaction kinetics [Figure 15C]. The corresponding theoretical overpotential comparison further indicates that the Volmer-Heyrovsky pathway requires a lower overpotential, suggesting that Fe-$Ti_4O_7$ favors $Cl_2$ formation through the reaction between *Cl and solution $Cl^-$, thereby lowering the kinetic barrier for active chlorine production [Figure 15D][215]. This system shows that lattice doping can tune the anode electronic structure and make $Cl^-$ activation more favorable than the competing oxygen evolution reaction. In contrast to chlorine evolution, Li *et al.*[287] developed a static lithium-bromide battery that illustrates another mode of two-electron halogen redox chemistry based on bromine species. The molecular model of $TBABr_3$ shows stable active bromine salts composed of tetrabutylammonium cations and $Br^{3-}$ anions, thereby avoiding the safety and cycling problems associated with liquid, volatile, and shuttle-prone $Br_2$ [Figure 15E]. The electron localization function (ELF) of $BrCl_3$ shows pronounced changes in electron distribution among Br-Cl species, indicating that $Cl^-$ coordination participates in stabilizing high-valence bromine-related structures [Figure 15F]. The cohesive-energy evolution during charging further shows that, compared with the $Cl^-$-free system, the presence of $Cl^-$ makes bromine conversion more favorable and stabilizes high-valence bromine species, thereby activating additional electron transfer and improving battery capacity [Figure 15G][287].

During halide oxidation, regulating the electronic structure and local coordination environment of catalytic sites is essential for achieving selective two-electron halogen conversion while suppressing competing oxygen evolution and catalyst degradation. Cho *et al.*[288] investigated Pt-based single-atom catalysts as a model system to understand how atomic coordination structures influence electrochemical selectivity. The T-shaped Pt-$N_4$ configuration was constructed as a representative active-site model for density functional theory calculations, providing insights into the relationship between local coordination geometry and oxygen evolution reaction pathways [Figure 15H]. The HAADF-STEM image of $Pt_1(3)$/CNT reveals atomically dispersed Pt species uniformly distributed on the carbon nanotube support, confirming the formation of isolated Pt catalytic sites [Figure 15I]. The calculated free-energy profiles further describe the stepwise oxygen evolution reaction (OER) mechanism involving *OH, *O, and *OOH intermediates on Pt-$N_4$ sites through a mononuclear pathway [Figure 15J]. These results demonstrate that the coordination structure of isolated metal sites can regulate intermediate adsorption energetics and influence oxidation reaction pathways by modifying the local electronic environment of active centers[288]. Mao *et al.*[214] further demonstrated that the position of the $Cl^-$ reaction site is crucial for the durability of non-noble-metal oxide anodes. The schematic of polyhedral distortion and $Cl^-$ adsorption modes in 3D Ce-$Co_3O_4$ shows that Ce doping induces local structural distortion in $Co_3O_4$, allowing $Cl^-$ to adsorb preferentially on Co active sites rather than on corrosion-prone lattice oxygen sites [Figure 15K]. The HAADF-STEM image shows that 3D Ce-$Co_3O_4$ maintains an ordered lattice with local atomic features, providing morphological evidence for Ce-induced structural regulation and active-site relocation [Figure 15L]. In terms of reaction energetics, the free-energy comparison among different $Co_3O_4$-based structures indicates that Ce doping lowers the energetic barriers for $Cl^-$ adsorption and $Cl_2$ formation, suggesting optimized $Cl^-$ binding on Co sites [Figure 15M]. The reaction-coordinate free-energy diagram further shows that Ce-modified Co sites exhibit lower barriers for *Cl formation and $Cl_2$ release, indicating that relocating active sites from lattice oxygen to metal Co centers can enhance $Cl^-$ oxidation while suppressing lattice-oxygen-involved corrosion [Figure 15N][214].

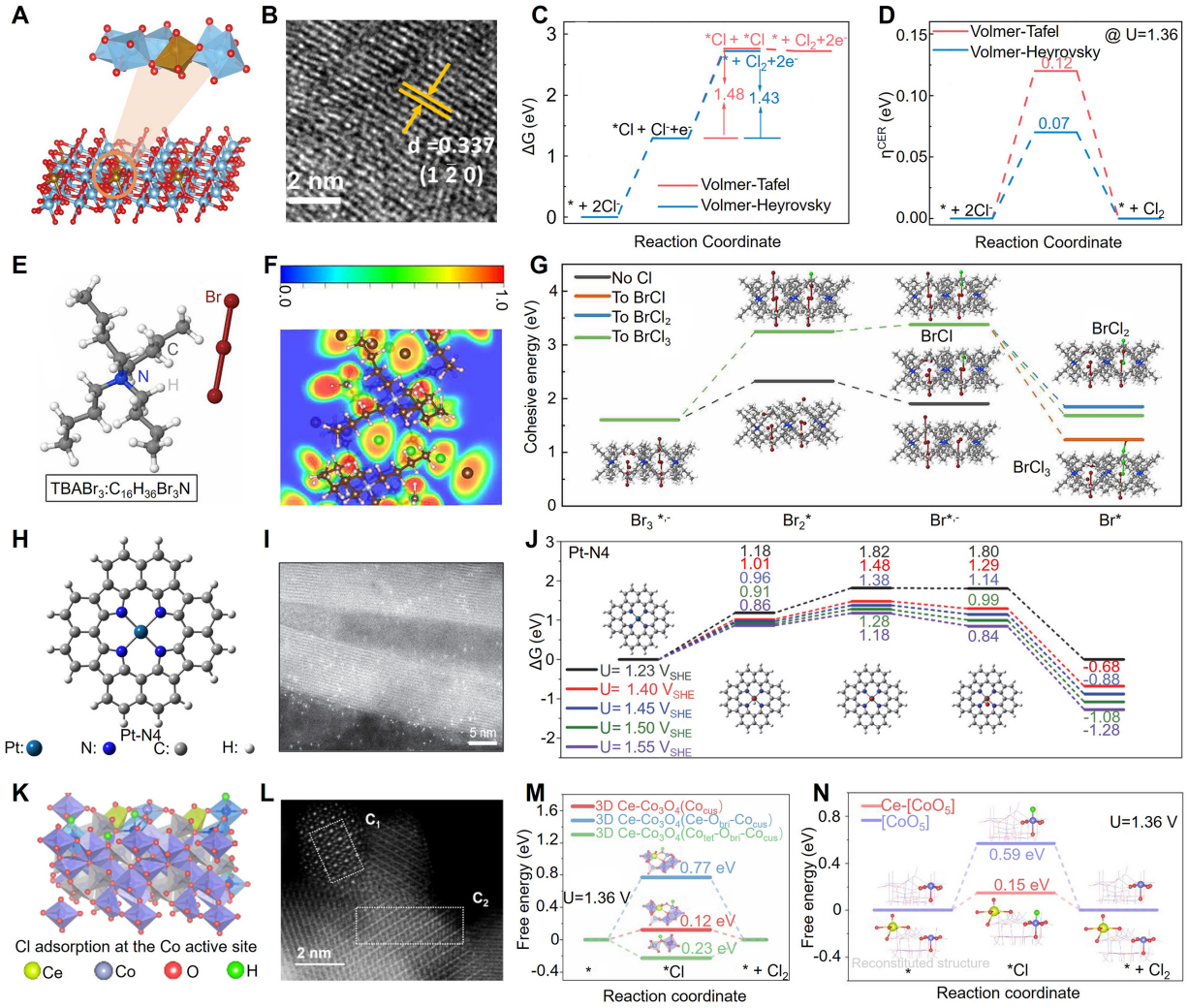



**Figure 15.** (A) Atomic structure model of Fe-$Ti_4O_7$. (B) HRTEM image of Fe-$Ti_4O_7$, showing the $Ti_4O_7$ (120) lattice plane. (C) Gibbs free-energy diagram for the chlorine evolution reaction on Fe-$Ti_4O_7$ via Volmer-Tafel and Volmer-Heyrovsky mechanisms. (D) Theoretical overpotential of the chlorine evolution reaction on Fe-$Ti_4O_7$ in Volmer-Tafel and Volmer-Heyrovsky mechanisms. (A-D) is reprinted with permission from Ref.[215]. Copyright © 2024 Springer Nature. (E) Molecular model of $TBABr_3$. (F) ELF of $BrCl_3$. (G) Cohesive energy during the charging process for the systems with and without $Cl^-$. (E-G) is reprinted with permission from Ref.[287]. Copyright © 2024 American Association for the Advancement of Science. (H) T-shaped Pt-$N_4$ models used for density functional theory calculations. (I) HAADF-STEM image of $Pt_1(3)$/CNT. (J) Free-energy profiles for the OER over Pt-$N_4$ following the mononuclear pathway, involving the *OH, *O and *OOH intermediates. (H-J) is reprinted with permission from Ref.[288]. Copyright © 2023 Springer Nature. (K) Schematics of polyhedral distortion and $Cl^-$ adsorption modes for 3D Ce-$Co_3O_4$; the green balls represent $Cl^-$ ions. (L) HAADF-STEM image of 3D Ce-$Co_3O_4$. (M) Free-energy comparison for chlorine evolution over different $Co_3O_4$-based structures at U = 1.36 V. (N) Reaction-coordinate free-energy diagram comparing Cl adsorption and $Cl_2$ formation on Ce-modified and unmodified Co sites. (K-N) is reprinted with permission from Ref.[214]. Copyright © 2026 Springer Nature.

## SUMMARY, CHALLENGES, AND OUTLOOK

In summary, this review presents inorganic two-electron electrocatalysis as a unified framework of selective redox chemistry in which the decisive scientific problem is not simply substrate activation but the controlled termination of electron transfer at a prescribed oxidation-state level. The discussion first establishes the conceptual foundation and chemical significance of two-electron pathways, followed by a systematic classification of reaction families involving oxygen, carbon dioxide, nitrogen-oxoanions, and halides, thereby revealing how diverse electrocatalytic systems share a common selectivity challenge despite fundamentally different bond-evolution chemistries. A structure-centered perspective is then introduced to connect two-electron selectivity with active-site electronic structure, coordination environment and atomic configuration,

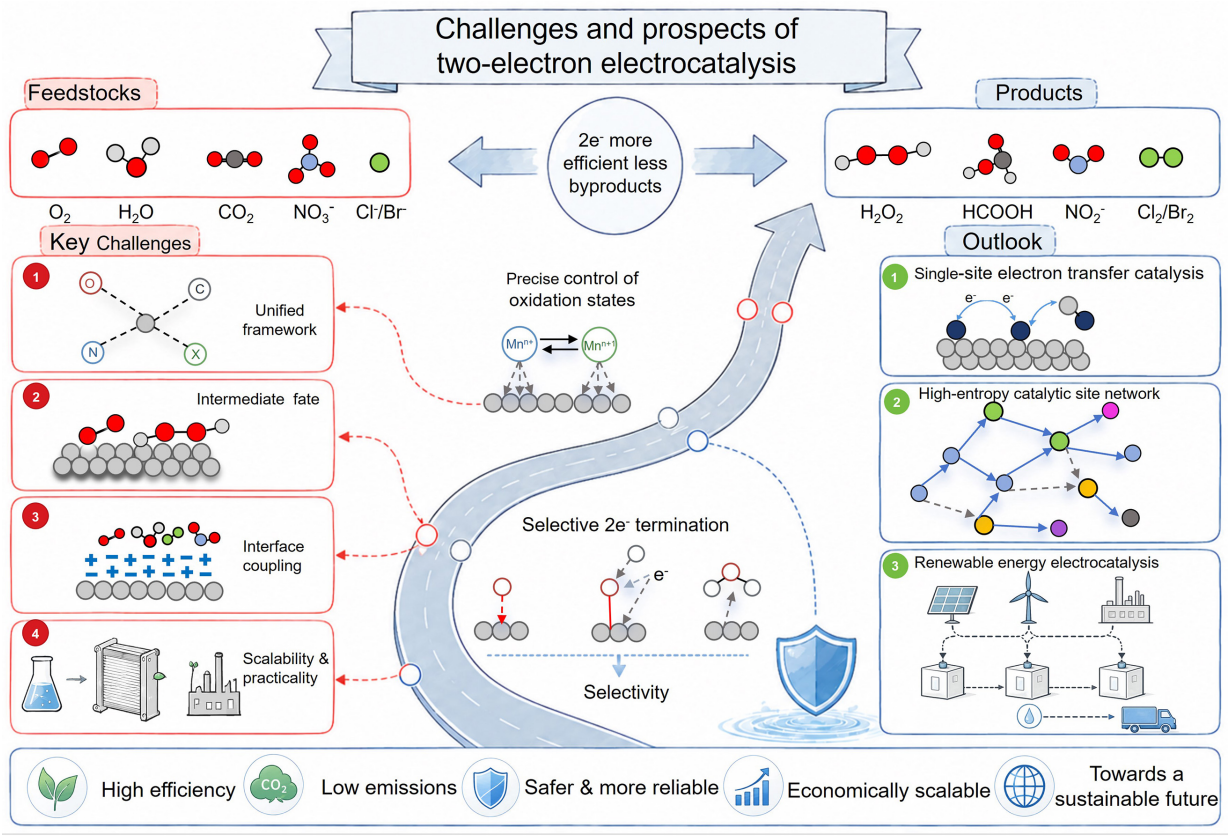



**Figure 16.** Challenges and prospects of two-electron electrocatalysis.

surface structure and defect chemistry, and interfacial microenvironment effects, which together form a hierarchical chemical basis for understanding how catalytic interfaces regulate partial redox conversion. The catalyst landscape is further organized across major inorganic material families, including metals and alloys, metal oxides and oxide-derived materials, metal hydroxides, metal sulfides and phosphides, metal carbides and nitrides, and emerging catalytic materials, allowing selective reactivity to be interpreted through the lens of materials structural chemistry rather than isolated reaction examples. Representative reaction systems are subsequently examined to illustrate how these principles manifest in practice across oxygen reduction, water oxidation, carbon dioxide reduction, nitrate reduction, and halide oxidation. The central distinctive feature of this review lies in the integration of reaction chemistry, structural chemistry, and catalyst classification into a coherent analytical framework that explains two-electron selectivity across multiple inorganic electrocatalytic systems.

Despite the rapid expansion of two-electron electrocatalysis across multiple reaction systems, the major obstacles in this field no longer lie in demonstrating that selective two-electron products can be obtained in individual reactions, but in determining whether two-electron selectivity can be understood and maintained as a general chemical principle across fundamentally different redox networks. The difficulty arises because two-electron pathways occupy a narrow kinetic boundary between substrate activation and deeper redox conversion, where selectivity depends simultaneously on adsorption energetics, proton-coupled electron transfer, intermediate stability, and product desorption dynamics. As a consequence, many reported successes remain reaction-specific rather than forming a predictive framework applicable across oxygen-, carbon-, nitrogen-, and halogen-centered electrocatalytic systems. Future progress is therefore increasingly limited not by the availability of catalyst materials, but by several deeper conceptual and translational challenges. Four issues are particularly critical for advancing two-electron electrocatalysis toward a more predictive and broadly deployable paradigm of selective electrochemical synthesis [Figure 16].

(1) A unified chemical framework for two-electron selectivity across different reaction families remains incomplete. Most mechanistic insights are still derived from isolated reaction systems, which obscures the common chemical principles that govern partial redox termination across oxygen, carbon, nitrogen, and halide chemistries.

(2) The dynamic fate of partially reduced or oxidized intermediates remains insufficiently resolved. Two-electron selectivity ultimately depends on whether a product-level intermediate can desorb before undergoing further transformation, yet this critical boundary is often inferred indirectly rather than directly observed under operating conditions.

(3) The coupling between catalyst structure and interfacial environment remains poorly integrated. Active-site structure, surface defects, solvation structure, ion distribution, and local proton activity jointly determine selectivity, yet these factors are frequently studied in isolation rather than as a unified interfacial system.

(4) Translation from laboratory-scale selectivity to practical electrosynthesis remains underdeveloped. Conditions relevant to large-scale operation introduce mass-transport limitations, product accumulation, and catalyst restructuring, which can fundamentally alter the delicate balance required for two-electron pathways.

Catalyst degradation during prolonged electrosynthesis can arise from several coupled pathways, including metal leaching, over-oxidation or over-reduction of active sites, surface passivation, dissolution-redeposition, and electrochemically induced structural reconstruction. Metal leaching can decrease the density of active sites and alter the local coordination environment, whereas over-oxidation or over-reduction may shift the electronic structure of the active center away from the optimal redox window. Surface passivation can further block active sites or modify intermediate adsorption, while dissolution-redeposition and surface reconstruction may generate new coordination motifs with different reaction energetics. These processes can therefore alter not only catalytic activity but also the balance between intermediate stabilization and product release, potentially promoting deeper multielectron pathways. Long-term stability in two-electron electrocatalysis should consequently be assessed by the simultaneous preservation of catalyst structure, active-site chemistry, and product selectivity rather than by electrochemical activity alone.

Against these challenges, the long-term significance of two-electron electrocatalysis lies not merely in improving selectivity within existing reaction systems, but in redefining how electrochemical synthesis is conceptualized at the level of oxidation-state control, interfacial chemical programming, and product-directed redox design. The field is beginning to move beyond the traditional logic of maximizing activity or total electron throughput toward a more chemically disciplined framework in which the central objective is to determine how many electrons a molecule should receive or release, at what stage the reaction should stop, and how that stopping point can be encoded into the catalyst-electrolyte interface. In this sense, the future of two-electron electrocatalysis will likely be shaped not only by better catalysts, but by broader shifts in how selective redox chemistry is designed, interpreted, and integrated into molecular manufacturing. Three directions appear especially important for the next stage of development.

(1) Two-electron electrocatalysis may evolve into a general platform for oxidation-state-precise electrosynthesis. Its broader value extends beyond the current set of representative reactions because it offers a conceptual template for producing molecules at chemically defined intermediate valence states rather than driving substrates toward full reduction or full oxidation. Such a shift could reshape electrosynthesis from a conversion-oriented discipline into one centered on redox-level precision, where product identity is controlled through deliberate electronic stopping rules at the interface.

(2) Future advances may emerge from the integration of reaction-network thinking with catalyst design. Two-electron pathways should increasingly be viewed not as isolated branches within individual reactions, but as controllable nodes embedded in broader chemical networks linking feedstocks, intermediates, and value-added products. From this perspective, catalyst development may progress toward reaction-network engineering, in which the goal is to stabilize strategically important partial-conversion states that can serve as independent synthetic outputs or as programmable intermediates for tandem electrochemical transformations.

(3) Two-electron electrocatalysis may become a key foundation for decentralized and function-specific chemical manufacturing. Many two-electron products, such as $H_2O_2$, HCOOH, nitrite, and halogens, derive their practical value precisely from their intermediate oxidation states, transportability, and downstream reactivity. As selective control becomes more reliable, two-electron electrocatalysis could enable smaller-scale, distributed production schemes tailored to local chemical demand, thereby linking fundamental advances in interfacial redox chemistry with a broader transformation in how high-value inorganic molecules are generated, delivered, and used.

## DECLARATIONS

### Authors' contributions

Conceptualization; Writing-original draft; Formal analysis; Data curation: Lu, Y.
Writing-original draft; Formal analysis; Software: Feng, J.
Software: Zhou, L.
Formal analysis; Software: Wang, H.
Conceptualization; Funding support: Xu, W.
Conceptualization; Funding support; Formal analysis; Data curation; Supervision; Validation; Writing-review & editing: Wan, J.

### Availability of data and material

Not applicable.

### AI and AI-assisted tools statement

Not applicable.

### Financial support and sponsorship statement

The authors acknowledge financial support from the National Natural Science Foundation of China (52203070) and the Natural Science Foundation of Hubei Province (2025AFB863).

### Conflict of interest

All authors declared that there are no conflicts of interest.

### Ethical approval and consent to participate

Not applicable.

### Consent for publication

Not applicable.

### Copyright

© The Author(s) 2026.

## REFERENCES

1. Chen, H.; Wang, C.; Wu, H.; et al. Host-guest-induced electronic state triggers two-electron oxygen reduction electrocatalysis. *Nat. Commun.* **2024**, *15*, 9222. DOI PubMed PMC
2. Guo, B.; Jiang, Q.; Mao, Z.; et al. B-F dual-doped carbon nanotubes for multi-site and high-rate two-electron oxygen reduction reaction electrocatalysis. *Carbon* **2024**, *222*, 118997. DOI

3. Mu, N.; Luo, Z.; Shan, W.; Huang, H.; Tang, H. Harnessing proton-coupled electron transfer in covalent organic frameworks for high-yield $H_2O_2$ photosynthesis. *ACS. Sustain. Chem. Eng.* **2025**, *13*, 16534-43. DOI
4. Liu, Y.; Wei, B.; Yang, L.; Han, X.; Wang, Y.; Zhao, X. Recent research progress in hydrogen peroxide synthesized by electrocatalytic process with two-electron transfer: a brief review. *J. Environ. Chem. Eng.* **2024**, *12*, 112972. DOI
5. Du, P.; Wang, R.; Deng, B.; et al. AC-electrochemical synthesis of $H_2O_2$ by breathing $O_2$ in three-phase interface. *Nano. Energy.* **2024**, *125*, 109600. DOI
6. Sun, M.; Zhang, G.; Qin, Y.; et al. Redox Conversion of chromium(VI) and arsenic(III) with the intermediates of chromium(V) and arsenic(IV) via AuPd/CNTs electrocatalysis in acid aqueous solution. *Environ. Sci. Technol.* **2015**, *49*, 9289-97. DOI
7. Su, Y.; Shi, Y.; Jin, L.; et al. Unlocking the potential of MOFs for waste plastic resource utilization and microplastic pollution control. *Sustain. Eng. Novit.* **2026**, *2*, 4. DOI
8. Eswaran, S. G.; Gao, Y.; Wang, A. Metal-organic frameworks: morphological diversity and applications of rod, sheet, cubic and octahedral structures. *Sustain. Eng. Novit.* **2026**, *2*, 5. DOI
9. Fu, D.; Zhu, J.; Wang, L.; et al. Biradical-mediated synergistic electrocatalysis using metal-free redox molecular catalysts. *Nat. Commun.* **2025**, *16*, 11520. DOI PubMed PMC
10. Bera, A.; Bimmermann, S.; Gerschel, P.; et al. Mechanistic promiscuity in cobalt-mediated $CO_2$ reduction reaction: one- versus two-electron reduction process. *Angew. Chem. Int. Ed.* **2025**, *64*, e202503705. DOI PubMed PMC
11. Xia, P.; Xu, T.; Niu, X.; et al. Regulating intermediate adsorption toward efficient two-electron oxygen reduction: fundamentals and perspectives. *Electrochim. Acta.* **2026**, *563*, 148696. DOI
12. Du, X.; Li, X.; Li, J.; Sun, T. Achievement of transition metal chalcogenides/oxides in hydrogen production by seawater electrolysis. *EcoEnergy* **2026**, e70072. DOI
13. Wei, L.; Dai, J.; Qin, S.; et al. Two-dimensional materials for high-current-density seawater electrolysis. *Green. Chem.* **2025**, *27*, 8755-76. DOI
14. Xu, R.; Zhu, Z.; Zhang, H.; et al. Synergistic material-structure engineering for mid-infrared thermal management in textiles. *Small* **2025**, *21*, e09257. DOI
15. Sun, M.; Yuan, Z. Valorization strategies for electrodegradation of nitrogenous wastes in sewage. *Acta. Phys. Chim. Sin.* **2025**, *41*, 100108. DOI
16. Qin, S.; Dai, J.; Tian, H.; et al. 3D printing driving innovations in extreme low-temperature energy storage. *Virtual. Phys. Prototyping.* **2025**, *20*, e2459798. DOI
17. Ma, X.; Wu, Z.; Tian, H.; et al. Durable coaxial fiber-based underwater strain sensor with reversible dry-wet transition. *InfoMat* **2025**, *7*, e70030. DOI
18. Song, H.; Liang, Y.; Zhang, G.; et al. Superhydrophobic wearable strain sensors: from strategic design to robustness paradigm. *Nano. Micro. Lett.* **2026**, *18*, 392. DOI PubMed PMC
19. Wang, W.; Ding, M.; Zhao, C. G.; et al. Unlocking migratory insertion in gold redox catalysis. *Angew. Chem. Int. Ed.* **2023**, *62*, e202304019. DOI
20. Li, L.; Wang, B.; Chen, H.; et al. Organogel polymer electrocatalysts for two-electron oxygen reduction. *Small* **2024**, *21*, 2410371. DOI
21. Song, M.; Liu, W.; Zhang, J.; Zhang, C.; Huang, X.; Wang, D. Single-atom catalysts for $H_2O_2$ electrosynthesis via two-electron oxygen reduction reaction. *Adv. Funct. Mater.* **2023**, *33*, 2212087. DOI
22. Yang, H.; An, N.; Kang, Z.; Menezes, P. W.; Chen, Z. Understanding advanced transition metal-based two electron oxygen reduction electrocatalysts from the perspective of phase engineering. *Adv. Mater.* **2024**, *36*, 2400140. DOI
23. Bernard, R. S.; Jha, A. K.; Kalek, M. Electrochemical oxidations through hypervalent iodine redox catalysis. *Tetrahedron. Chem.* **2024**, *11*, 100081. DOI
24. Xie, Z.; Gupta, N.; Niklas, J.; et al. Photochemical charge accumulation in a heteroleptic copper(i)-anthraquinone molecular dyad*via* proton-coupled electron transfer. *Chem. Sci.* **2023**, *14*, 10219-35. DOI PubMed PMC
25. Miller, D. C.; Tarantino, K. T.; Knowles, R. R. Proton-coupled electron transfer in organic synthesis: fundamentals, applications, and opportunities. *Top. Curr. Chem.* **2016**, *374*, 30. DOI PubMed PMC
26. Mondal, I.; Sheng, H.; Lee, K.; Jin, S.; Schmidt, J. R. Rationalizing the overall $H_2O_2$ selectivity of metal dichalcogenide electrocatalysts for the two-electron oxygen reduction reaction using microkinetic modeling. *ACS. Catal.* **2025**, *15*, 8788-98. DOI
27. Zhao, G.; Chen, T.; Tang, A.; Yang, H. Roles of oxygen-containing functional groups in carbon for electrocatalytic two-electron oxygen reduction reaction. *Chem. A. Eur. J.* **2024**, *30*, e202304065. DOI
28. Peng, W.; Liu, J.; Liu, X.; et al. Facilitating two-electron oxygen reduction with pyrrolic nitrogen sites for electrochemical hydrogen peroxide production. *Nat. Commun.* **2023**, *14*, 4430. DOI PubMed PMC

29. Jing, B.; Zhang, Q.; Liu, M.; et al. Magnetically-altered eg-orbital occupancy to boost the two-electron oxygen reduction electrocatalysis for faster water decontamination. *Appl. Catal. B. Environ. Energy.* **2025**, *369*, 125149. DOI
30. Zhao, Y.; Raj, J.; Xu, X.; Jiang, J.; Wu, J.; Fan, M. Carbon catalysts empowering sustainable chemical synthesis via electrochemical $CO_2$ conversion and two-electron oxygen reduction reaction. *Small* **2024**, *21*, 2311163. DOI PubMed PMC
31. Shou, W.; Zhao, W.; Liu, Y.; Wang, T. Toward rational understanding of the hydrogen evolution polarization curves through multiscale simulations. *Nat. Commun.* **2025**, *17*, 802. DOI PubMed PMC
32. Zhang, Z.; Li, J.; Wang, Y. Modeling interfacial dynamics on single atom electrocatalysts: explicit solvation and potential dependence. *Acc. Chem. Res.* **2024**, *57*, 198-207. DOI
33. Yu, A.; Liu, S.; Yang, Y. Recent advances in electrosynthesis of $H_2O_2$ *via* two-electron oxygen reduction reaction. *Chem. Commun.* **2024**, *60*, 5232-44. DOI
34. Zhu, L.; Yao, H.; Sun, L.; Ai, L.; Zhai, H.; Yi, C. Alloyed rhodium-copper nanocavities with optimized chemisorption of hydrogen radicals for efficient nitrate-to-ammonia electrocatalysis. *Small* **2025**, *21*, 2502787. DOI PubMed
35. Jiang, S.; Zhang, L.; Yu, H.; et al. Heterostructure and interface engineering of $Ni_{0.85}Se$-$MoSe_2$@PEI for enhancing electrocatalytic acidic oxygen reduction to hydrogen peroxide. *Chem. Eng. J.* **2024**, *489*, 151272. DOI
36. Mei, X.; Zhao, X.; Du, H.; et al. Adjusting the active site of single Co atoms on $CeO_2$ via cyano functional groups for selective $H_2O_2$ electrosynthesis at high yield. *Appl. Catal. B. Environ. Energy.* **2025**, *374*, 125398. DOI
37. Xu, X.; Xu, R.; Zhao, Y.; et al. Boron-doped biomass carbon nanostructures as electrocatalysts for the two-electron oxygen reduction reaction. *ACS. Appl. Nano. Mater.* **2024**, *7*, 18912-9. DOI
38. Li, Z.; Jia, J.; Sang, Z.; et al. A computation-guided design of highly defined and dense bimetallic active sites on a two-dimensional conductive metal-organic framework for efficient $H_2O_2$ electrosynthesis. *Angew. Chem. Int. Ed.* **2024**, *63*, e202408500. DOI
39. Zuo, L.; Deng, Y.; Chen, L.; He, T.; Yang, J.; Zhang, J. Fundamental insights into photoelectrochemical carbon dioxide reduction: elucidating the reaction pathways. *ACS. Catal.* **2024**, *14*, 16795-833. DOI
40. Li, Y.; Sun, X.; Liu, M.; et al. Self-hydroxylated iron oxyhydroxide nanoislands boosting near-unity two-electron oxygen reduction selectivity over conductive MOFs. *Chem. Eng. J.* **2024**, *494*, 153132. DOI
41. Guo, Q.; Huang, B.; Bo, G.; et al. Molecular engineering of wastewater nickel into single-site electrocatalysts for hydrogen peroxide production with industrial level current. *Angew. Chem. Int. Ed.* **2025**, *137*, e202514519. DOI
42. Song, J.; Yu, J. M.; Ahn, J. H.; et al. Selective, stable, bias-free, and efficient solar hydrogen peroxide production on inorganic layered materials. *Adv. Funct. Mater.* **2022**, *32*, 2110412. DOI
43. Perry, S. C.; Pangotra, D.; Vieira, L.; et al. Electrochemical synthesis of hydrogen peroxide from water and oxygen. *Nat. Rev. Chem.* **2019**, *3*, 442-58. DOI
44. Li, X.; Xu, W.; Le, L. Q.; et al. Sulfur-modulated isolated $NiN_x$ sites toward electrocatalytic hydrogen peroxide generation. *Chem. Catal.* **2023**, *3*, 100724. DOI
45. Ahn, S. M.; Lee, S.; Lee, G.; et al. Hydroxyl-blocking lignin-derived carbon catalysts for selective and durable hydrogen peroxide electrosynthesis. *Appl. Catal. B. Environ. Energy.* **2026**, *390*, 126606. DOI
46. Xia, H.; Sun, H.; Yang, D.; et al. Curvature-engineered steering of oxygen electroreduction pathways on single-atom catalysts. *Angew. Chem. Int. Ed.* **2026**, *138*, e3924995. DOI
47. Wang, Y.; Wang, Y.; Dong, Q.; et al. Boosting the electrochemical $O_2$-to-$H_2O_2$ synthesis by revamping the FeMo catalyst with N/O co-doped surface. *Chem. Eng. J.* **2023**, *460*, 141673. DOI
48. Zhang, S.; Wang, Y.; Jiang, C.; et al. Doped-Sn enhanced the performance of BiOCl nanosheet on electrocatalytic synthesis of hydrogen peroxide. *Small* **2024**, *20*, 2403862. DOI
49. Yan, L.; Wang, C.; Wang, Y.; et al. Optimizing the binding of the *OOH intermediate via axially coordinated Co-$N_5$ motif for efficient electrocatalytic $H_2O_2$ production. *Appl. Catal. B. Environ.* **2023**, *338*, 123078. DOI
50. Xie, M.; Zheng, W.; Ren, Y.; Yu, H.; Liu, J.; Liu, Y. Steering pulsed electrochemistry selectivity toward singlet oxygen via dynamic intermediate management. *Angew. Chem. Int. Ed.* **2026**, *138*, e24903. DOI
51. Yang, M.; Song, W.; Chen, C.; et al. Atomically dispersed Co/Mo sites anchored on mesoporous carbon hollow spheres for highly selective oxygen reduction to hydrogen peroxide in acidic media. *Adv. Mater.* **2025**, *37*, 2416401. DOI
52. Wang, R.; Luo, H.; Duan, C.; et al. Crystal OH mediating pathway for hydrogen peroxide production via two-electron water oxidation in non-carbonate electrolytes. *Nat. Commun.* **2024**, *15*, 10456. DOI PubMed PMC
53. Yan, H.; Jiang, J.; Huang, Y.; et al. Inter-ring bonding electron donor structure triggers efficient two-electron water oxidation for photocatalytic hydrogen peroxide synthesis. *Adv. Mater.* **2025**, *38*, e07961. DOI
54. Hu, X.; Jiang, H.; Chen, R.; et al. Breaking the scaling relationship in two-electron water oxidation via designing dual active centers for efficient $H_2O_2$ electrosynthesis. *ACS. Catal.* **2025**, *15*, 8403-13. DOI

55. Dong, X.; Shi, W.; Tao, S.; Chen, Y.; Zhang, J. Constructing frustrated Lewis acid-base Cu···N pairs on Pd metallene toward efficient oxygen reduction reaction. *DeCarbon* **2026**, *12*, 100163. DOI
56. Hong, S.; Yuan, L.; Liu, S.; et al. Unusual fullerene-like curved surface with unique Fe-$N_4$ sites for highly efficient oxygen reduction reaction in zinc-air battery. *Innov. Energy.* **2026**, *3*, 100154. DOI
57. Yan, Y.; Yang, H.; Zhou, T.; et al. Fe-free photocatalysis-self-fenton system for ultraefficient water purification enabled by carbon nitride with strong built-in electric field. *EcoEnergy* **2026**, *4*, e70044. DOI
58. Hao, A.; Qiu, X.; Ye, Y.; et al. Constructing amorphous ZnCdS/$Bi_4Ti_3O_{12}$-Ov heterostructure for enhancing piezocatalytic coupled Fenton-like reaction toward efficient wastewater purification and unraveling the mechanism. *Mater. Futures.* **2026**, *5*, 035101. DOI
59. Wang, K.; Zhang, X.; Lyu, J.; et al. Recent progress of dual-atom catalysts on zinc-air batteries. *Nano. Mater. Sci.* **2026**, *8*, 585-611. DOI
60. Ling, C.; Jin, D.; Li, R.; Li, C.; Wang, W. Self-assembled membranes modulate the active site of carbon fiber paper to boost the two-electron water oxidation reaction. *Chem. Eng. J.* **2023**, *465*, 142903. DOI
61. Liang, Z.; Lei, H.; Zheng, H.; et al. Selective two-electron and four-electron oxygen reduction reactions using Co-based electrocatalysts. *Chem. Soc. Rev.* **2025**, *5411*, 5248-91. DOI
62. Zhu, K.; Shou, W.; Jia, B.; et al. Sponge-inspired catalyst design for durable acidic $CO_2$ reduction at low $K^+$ concentration. *Nat. Commun.* **2026**, *17*, 5763. DOI PubMed PMC
63. Jiang, T.; Qin, X.; Ye, K.; et al. An interactive study of catalyst and mechanism for electrochemical $CO_2$ reduction to formate on Pd surfaces. *Appl. Catal. B. Environ.* **2023**, *334*, 122815. DOI
64. Li, Z.; Wei, X.; Zhu, Z.; et al. Synthesis, characterizations, and structure-activity relationship of dual-atom catalysts for $CO_2$ electroreduction. *DeCarbon* **2025**, *9*, 100112. DOI
65. Yang, Z.; Li, X.; Cui, X.; Zheng, Z.; Zheng, P.; Zhang, Y. Integrated strategies toward the capture and electrochemical conversion of low-concentration carbon dioxide. *Exploration* **2025**, *5*, e20240006. DOI PubMed PMC
66. Chen, R.; Wu, Q.; Luo, J.; Zu, X.; Zhu, S.; Sun, Y. Defective ultrathin two-dimensional materials for photo-/electrocatalytic $CO_2$ reduction: fundamentals and perspectives. *Acta. Phys. Chim. Sin.* **2025**, *41*, 100019. DOI
67. Wang, F.; Wang, B.; Zhang, T.; Liu, J. Electrochemical $CO_2$ reduction to $C^{3+}$ products: a review. *Green. Carbon.* **2026**, *4*, 12-26. DOI
68. Zhang, C.; Gu, Y.; Jiang, Q.; et al. Exploration of gas-dependent self-adaptive reconstruction behavior of $Cu_2O$ for electrochemical $CO_2$ conversion to multi-carbon products. *Nano. Micro. Lett.* **2024**, *17*, 66. DOI PubMed PMC
69. Liu, H.; Zhang, Y.; Xu, Q.; et al. Carnot battery with thermochemical energy storage and supercritical $CO_2$ power cycle: thermodynamic and techno-economic characteristics. *Innov. Energy.* **2026**, *3*, 100163. DOI
70. Li, B.; Ruan, X.; Ravi, S. K. Polyoxometalates in photocatalytic $CO_2$ reduction: multielectron redox regulation across molecular and hybrid architectures. *EcoEnergy* **2026**, e70076. DOI
71. Zhang, G.; Wang, Z.; Shi, D.; et al. Rational design of $H_2$ production sites for achieving photoconversion of $CO_2$ with $H_2O$ into widely adjustable syngas and highly effective $H_2$ evolution. *Green. Carbon.* **2025**, *3*, 11-21. DOI
72. Naveen, B.; Lee, S. Rational design of Cu@Pd core-shell nanostructures via galvanic replacement for dual electrochemical applications: hydrogen evolution and nitrate reduction reactions. *Molecules* **2025**, *30*, 4062. DOI PubMed PMC
73. Huang, C.; Triana, C. A.; Jia, B.; Erni, R.; Zhao, H.; Patzke, G. R. *Operando* tracking of the structural evolution of copper carbodiimide during electrocatalytic nitrate reduction. *ACS. Catal.* **2025**, *15*, 11407-16. DOI
74. Bai, L.; Franco, F.; Timoshenko, J.; et al. Electrocatalytic nitrate and nitrite reduction toward ammonia using $Cu_2O$ nanocubes: active species and reaction mechanisms. *J. Am. Chem. Soc.* **2024**, *146*, 9665-78. DOI
75. Zhang, L.; Wu, Y.; Zhu, Z.; et al. Synergistically enhancing nitrate reduction into $N_2$ in water by N-doped Pd-Cu biochar bimetallic single-atom electrocatalysis. *Biochar* **2024**, *6*, 8. DOI
76. Liu, M.; Lu, Z.; Yang, L.; et al. Co-N bond promotes the H* pathway for the electrocatalytic reduction of nitrate ($NO_3RR$) to ammonia. *J. Environ. Chem. Eng.* **2023**, *11*, 109718. DOI
77. Zhou, N.; Wang, Z.; Zhang, N.; Bao, D.; Zhong, H.; Zhang, X. Potential-induced synthesis and structural identification of oxide-derived Cu electrocatalysts for selective nitrate reduction to ammonia. *ACS. Catal.* **2023**, *13*, 7529-37. DOI
78. Wang, Y.; Zeng, W.; Gong, Q.; Zhan, M.; Hao, X.; Peng, Y. Enhancing anaerobic ammonium oxidation via polymeric ferric sulfate (PFS)-mediated dual-electron Acceptor: a solution to nitrite deficiency. *Chem. Eng. J.* **2024**, *498*, 155199. DOI
79. Sun, X.; Zheng, K. Electrochemical halogen-atom transfer alkylation via α-aminoalkyl radical activation of alkyl iodides. *Nat. Commun.* **2023**, *14*, 6825. DOI PubMed PMC
80. Peng, F.; Xiang, J.; Qin, H.; et al. Selective electrochemical oxidation of benzylic C-H to benzylic alcohols with the aid of imidazolium radical mediators. *J. Am. Chem. Soc.* **2023**, *145*, 23905-9. DOI
81. Xiao, Y.; Xia, C.; Qian, Q.; et al. Halogen cocatalysis in electrocatalytic systems. *Small* **2025**, *21*, e05412. DOI

82. Li, Z.; Wang, Q.; Gao, R.; Zhang, S. One- and two-electron carbon-halide bond activation at a phosphorus center. *Angew. Chem. Int. Ed.* **2025**, *138*, e21209. DOI
83. Wang, D.; Kong, X.; Wang, Z.; Zhang, X.; Zhang, J.; Chen, Y. Dual-functional $Fe_3O_4$-decorated porous carbon nanosheets for kinetics-enhanced aqueous zinc-iodine batteries. *Green. Carbon.* **2025**, *3*, 382-92. DOI
84. Fan, M.; Guo, J.; Fang, G.; et al. Microwave-pulse assisted synthesis of tunable ternary-doped 2D molybdenum carbide for efficient hydrogen evolution. *Chem. Synth.* **2024**, *4*, 36. DOI
85. Li, Q.; Fang, G.; Wu, Z.; et al. Advanced microwave strategies facilitate structural engineering for efficient electrocatalysis. *ChemSusChem* **2024**, *17*, e202301874. DOI
86. Wang, M.; Feng, Y.; Dai, J.; et al. Phase diversity driven mechanistic landscapes for nitrate to ammonia electrosynthesis. *J. Hazard. Mater.* **2026**, *505*, 141470. DOI
87. Zhang, S.; Zhuo, G.; Wang, R.; et al. Polymer/MXene composite-based flexible pressure sensors: from mechanisms and structural designs to emerging applications. *Polym. Sci. Technol.* **2026**, *2*, 519-55. DOI PubMed PMC
88. Zhang, H.; Huang, Z.; Chen, C.; et al. Mid-infrared transparent materials: from mechanisms to cutting-edge applications. *Nano. Micro. Lett.* **2026**, *18*, 260. DOI PubMed PMC
89. Liu, Z. L.; Zhou, J. L.; Yuan, S. X.; Zhang, M. R.; Zhang, M.; Lu, T. B. Asymmetry-engineered g-$C_3N_4$ nanosheets with dual electronic-adsorption modulation for high-efficiency solar-driven $H_2O_2$ synthesis. *Adv. Funct. Mater.* **2025**, *36*, e23126. DOI
90. Li, X.; Yang, S.; Yang, X.; et al. Modulating pore sizes and electronic properties of covalent organic polymers for the catalysis of two-electron oxygen reduction reaction in neutral media. *ACS. Catal.* **2024**, *14*, 13883-91. DOI
91. Wang, Y.; Cheng, S.; Liu, Y.; et al. Fine-tuning electronic structure through phosphorus doping and defect engineering for selective 2e- ORR. *ACS. Sustain. Chem. Eng.* **2025**, *13*, 17445-54. DOI
92. Wang, Y.; Bi, Y.; Xu, F.; et al. Synergistically crafted d-band center, d-orbital splitting manner and occupation in $Fe_2O_3$ anode for enhanced Ni-Fe battery performance. *Nano. Energy.* **2026**, *151*, 111846. DOI
93. Pei, M. J.; Gao, X.; Shuai, Y. K.; et al. Machine learning-assisted molecular orbital insights into OER activity descriptors of component gradient Ni-based LDH electrocatalysts. *Small* **2025**, *21*, 2506357. DOI
94. Nørskov, J. K.; Rossmeisl, J.; Logadottir, A.; et al. Origin of the overpotential for oxygen reduction at a fuel-cell cathode. *J. Phys. Chem. B.* **2004**, *108*, 17886-92. DOI
95. Hammes-schiffer, S.; Stuchebrukhov, A. A. Theory of coupled electron and proton transfer reactions. *Chem. Rev.* **2010**, *110*, 6939-60. DOI PubMed PMC
96. He, Q.; Lin, D.; Yin, D.; Yang, C.; Chen, D.; Feng, X. Propene epoxidation with molecular oxygen: advancements from nanoparticle to single-atom catalysts. *Smart. Mol.* **2024**, *2*, e20240025. DOI PubMed PMC
97. Wang, S.; Luan, Y.; Ye, F.; et al. Cross-conjugated donor-acceptor polymers for high-performance organic electrochemical transistors. *Poly. Sci. Technol.* **2026**, *2*, 419-28. DOI PubMed PMC
98. Lei, B.; Zhou, G.; Gong, Z.; et al. Dynamically cyclic $Fe^{2+}/Fe^{3+}$ active sites as electron and proton-feeding centers boosting $CO_2$ photoreduction powered by benzyl alcohol oxidation. *Research* **2024**, *8*, 0567. DOI PubMed PMC
99. Chen, X.; Lim, E. L.; Wei, Z. A brief overview of air-processed polycrystalline perovskite light-emitting diodes. *Mater. Matter.* **2026**, *1*, 3. DOI
100. Yang, Y.; Song, T.; Ma, J.; et al. Synthesis of $Ce_2Sn_2O_7$ pyrochlore and $Ce_2Sn_2O_{8+x}$ solid solution to support $FeO_x$ for simultaneous $NH_3$-SCR and CO oxidation: study on the paramorphism effect. *Smart. Mater. Devices.* **2026**, *2*, 202612. DOI
101. Zhang, C.; He, Z.; Qiao, L.; et al. Regulating the spin state of triple-atom catalysts for improved oxygen electrocatalysis in zinc-air batteries at subzero temperature. *Innov. Mater.* **2025**, *3*, 100131. DOI
102. Zhang, J.; Feng, L.; Zhang, J.; et al. Electronic structure tailored covalent organic frameworks for synergistic adsorptive-photocatalytic gold recovery from complex electronic waste. *Research* **2025**, *8*, 1012. DOI PubMed PMC
103. Singh, D. K.; Natchimuthu Karuppusamy, M.; Shrivastava, A.; Palanisamy, T.; Sinha, I.; Ganesan, V. Sulfonic acid functionalization-boosted ultrafast, durable, and selective four-electron oxygen reduction reaction: evidenced by EC-SHINERS and DFT studies. *ACS. Catal.* **2023**, *13*, 4155-67. DOI
104. Wang, C.; Wang, Z.; Lei, W.; Zhang, H.; Wang, Y. Enhancing the d-Electrocatalytic activity of MXene through defect engineering. *Carbon. Energy.* **2026**, *8*, e70148. DOI
105. Chen, R.; Li, J.; Zhu, K.; et al. Electrocatalytic depolymerization of PET plastic fibers for circular textiles. *Sustain. Eng. Novit.* **2026**, *2*, 6. DOI
106. Feng, Y.; Wang, M.; Zhang, H.; et al. Engineering electrocatalytic structures through molten salt-mediated mechanistic control. *EcoEnergy* **2025**, *3*, e70022. DOI

107. He, Z.; Zhu, K.; Chen, R.; Zhou, L.; Ma, Y.; Wan, J. Engineering porous 2D materials for electrocatalytic small-molecule oxidation in decarbonized energy systems. *Carb. Neutr.* **2026**, *5*, 19. DOI
108. Xie, L.; Liu, Y.; Li, S.; Shen, B.; Zhu, W. Phase and facet engineering for nanoscale catalyst discovery in electrochemical $CO_2$ reduction. *Nat. Synth.* **2026**, *5*, 489-505. DOI
109. Zhu, K.; Li, Z.; Chen, R.; Zhou, L.; Ma, Y.; Wan, J. Porous two dimensional architectures for high efficiency electrocatalytic urea oxidation. *Smart. Mol.* **2026**, *4*, e70057. DOI PubMed PMC
110. Jiao, J.; Wei, H.; Lei, Q.; et al. Recent progress on photoelectrochemical valorizations: a review of reactions, catalyst design, and future prospects. *Sustain. Eng. Novit.* **2026**, *2*, 5. DOI
111. Jiang, Y.; Xie, Y.; Pan, Q.; et al. Universal taxol molecular binding engineering in dual-polarity $MoS_2$ photodetector. *Innov. Mater.* **2026**, *4*, 100191. DOI
112. Geng, Y.; Cao, Y.; Zhu, J. Graphene quantum dots: synthesis, properties, and applications in electroanalysis. *Nano. Electrochem. Nano. Photochem.* **2025**, *1*, 3. DOI
113. Zhang, M.; Li, J.; Mao, W.; Zhang, W.; Chu, L. Air-processed FA-Cs perovskite scalable films without $Pb^0$ defects for efficient inverted photovoltaic modules. *J. Mater. Chem. A.* **2026**, *14*, 14603-11. DOI
114. Wei, R.; Li, S.; Li, A.; Lin, Y. Photo-/electrocatalytic reduction of $CO_2$ based on ferroelectrics. *Research* **2025**, *8*, 0843. DOI PubMed PMC
115. Zhou, L.; Feng, J.; Zhu, K.; et al. Crystallographic symmetry-governed oxygen-defect chemistry in perovskite oxides for electrocatalytic water splitting. *Mater. Matter.* **2026**, *1*, 1. DOI
116. Zhang, H.; Fan, M.; Liu, K.; et al. Unconventional trigonal $PrNiO_3$ nanosheets for efficient electrocatalytic degradation of PET fibers. *Nano. Mater. Sci.* **2026**, S2589965126000693. DOI
117. Qin, S.; Chen, R.; Zhu, K.; et al. Electrocatalytic degradation strategies for plastic fibers with sustainable resource recovery potential. *Coord. Chem. Rev.* **2026**, *558*, 217806. DOI
118. Chen, J.; Chu, L. AB epoxy encapsulation-induced transparency in perovskite films. *Sci. China. Mater.* **2025**, *69*, 570-4. DOI
119. Ma, T.; Yang, M.; Feng, J.; et al. Spinel oxide crystallography governing lattice-coupled water-redox electrocatalysis. *Smart. Mater. Devices.* **2026**, *2*, 202546. DOI
120. Zhang, S.; Liu, F.; Zhang, Y.; Zhou, W.; Chen, L.; Liu, Y. $CeO_2$ facet-directed interfacial engineering in $Ru_1/CeO_2$ catalysts for efficient 2-butanol production from levulinic acid. *Innov. Energy.* **2026**, *3*, 100156. DOI
121. Zhu, Z.; Zhang, H.; Hu, R.; Yao, Y.; Xu, W.; Wan, J. Thermally stable 2D $YMnO_3$ enabling blue visible camouflage with mid-infrared transparency. *Nat. Commun.* **2026**, *17*, 8247. DOI PubMed PMC
122. Costentin, C. Electrochemical approach to the mechanistic study of proton-coupled electron transfer. *Chem. Rev.* **2008**, *108*, 2145-79. DOI
123. Zhou, P.; Zhao, X.; Song, Y.; Ge, R.; Duan, H. pH-dependent electrochemical oxidation of 5-hydroxymethylfurfural: reaction mechanism, catalyst design, and reactor design across alkaline to acidic media. *Smart. Mol.* **2025**, *4*, e70027. DOI PubMed PMC
124. Tian, H.; Yao, M.; Guo, Y.; et al. Hydrogel electrolyte with regulated water activity and hydrogen bond network for ultra-stable zinc electrode. *Adv. Energy. Mater.* **2024**, *15*, 2403683. DOI
125. Yu, M.; Wu, J.; Yin, G.; Jiao, F.; Yu, Z.; Qu, J. Dynamic regulation of hydrogen bonding networks and solvation structures for synergistic solar-thermal desalination of seawater and catalytic degradation of organic pollutants. *Nano. Micro. Lett.* **2024**, *17*, 48. DOI PubMed PMC
126. Zhang, S.; Gou, Q.; Chen, W.; et al. Co-regulating solvation structure and hydrogen bond network via bio-inspired additive for highly reversible zinc anode. *Adv. Sci.* **2024**, *11*, 2404968. DOI PubMed PMC
127. Anantharaj, S.; Pitchaimuthu, S.; Noda, S. A review on recent developments in electrochemical hydrogen peroxide synthesis with a critical assessment of perspectives and strategies. *Adv. Colloid. Interface. Sci.* **2021**, *287*, 102331. DOI PubMed
128. Kim, J.; Kim, Y. E.; Je, M.; et al. A conformal titanyl phosphate amorphous overlayer for enhancing photoelectrochemical hydrogen peroxide production. *J. Energy. Chem.* **2023**, *86*, 399-408. DOI
129. Wang, Y.; Sun, M.; Li, B.; Zhu, Y. Bubble engineering on flexible electrodes: from static interfaces to dynamic control. *FlexMat* **2026**, flm2.70074. DOI
130. Zhang, K.; Zhang, C.; Lin, Z.; et al. Carbon-based perovskite solar cell enables graded utilization of full solar spectrum beyond the photovoltaic S-Q limit via hybrid photovoltaics-photothermal conversion. *Mater. Matter.* **2026**, *1*, 2. DOI
131. Liu, Q.; Zhu, Z.; Zhang, H.; et al. Advanced warming textiles for personalized thermal management through radiative, insulating, and electrothermal strategies. *Mater. Today. Energy.* **2026**, *56*, 102192. DOI
132. Wu, J.; Zhang, S.; Gu, Q.; Zhang, Q. Recent progress in covalent organic frameworks for flexible electronic devices. *FlexMat* **2024**, *1*, 160-72. DOI

133. Long, Y.; Chen, Z.; Xie, J.; et al. Sustainable plant-based electrodes for electrocatalytic conversion of small molecules: from biomass to functional electrodes. *Exploration* **2026**, *6*, 20250158. DOI PubMed PMC
134. Li, Y.; Lei, Q.; Hong, W. T.; Liu, X.; Xue, C.; Kim, J. K. Transition metal-based materials for electrochemical and photoelectrochemical carbon-free nitrogen cycling as H-carrier. *Exploration* **2025**, *5*, 20240245. DOI PubMed PMC
135. Fan, M.; Tian, H.; Wu, Z.; et al. Microwave shock synthesis of porous 2D non-layered transition metal carbides for efficient hydrogen evolution. *SusMat* **2024**, *5*, e252. DOI
136. Liu, C. F.; Huang, J.; Wang, S.; Li, Y.; Lai, W. Y. Flexible organic crystals: from rational design to applications. *FlexMat* **2025**, *2*, 582-90. DOI
137. Hu, Y.; Dai, L.; Li, B.; Yu, C.; Li, Z. Synergistic catalytic mechanism and performance regulation strategies between nanoparticles/clusters and single-atom sites. *Mater. Futures.* **2025**, *4*, 032102. DOI
138. Yang, G.; Chen, F.; Fang, Q.; et al. Structural engineering of photoisomerizable covalent organic frameworks: design principles and functional applications. *Polym. Sci. Technol.* **2025**, *1*, 672-91. DOI PubMed PMC
139. Man, H.; Chen, G.; Wang, F.; et al. Entropy engineering activates Cu-Fe inertia center from prussian blue analogs with micro-strains for oxygen electrocatalysis in Zn-air batteries. *Carbon. Energy.* **2025**, *7*, e693. DOI
140. Zhan, X.; Tong, X.; Ye, H.; et al. Atomically dispersed metal site materials for hydrogen energy utilization: theoretical and experimental study in fuel cells and water electrolysis. *DeCarbon* **2025**, *7*, 100091. DOI
141. Wu, Z.; Yang, P.; Gao, M. Dynamic evolution of copper-based catalysts during $CO_2$ electroreduction. *Nano. Mater. Sci.* **2026**, *8*, 687-702. DOI
142. Hussain, M. S.; Ahmed, S.; Irshad, M.; et al. Recent engineering strategies for enhancing $C^{2+}$ product formation in copper-catalyzed $CO_2$ electroreduction. *Nano. Mater. Sci.* **2026**, *8*, 207-33. DOI
143. Tan, X.; Liu, H.; Hou, T.; et al. Hardness augmentation engineering of $TiFe_2$ with doping design and single-crystal realization. *Innov. Mater.* **2025**, *3*, 100140. DOI
144. Zhang, J.; Liang, P.; Xu, X.; et al. Synergy of compress strain and antioxidant of platinum-copper for enhanced the oxygen reduction performance. *Nano. Mater. Sci.* **2025**, *7*, 105-12. DOI
145. Shang, Z.; Chen, G.; Cui, Z.; Jiao, W.; Han, Y. Ordered modulation of electronic structure for efficient alkaline hydrogen oxidation. *FlexMat* **2025**, *3*, 93-100. DOI
146. Zhang, B.; Han, B.; Guan, C.; Guo, Q.; Luo, Y.; Jiang, J. Highly selective oxygen reduction to $H_2O_2$ on π-d conjugated coordination polymers: the effect of coordination atoms. *Chem. Eng. J.* **2023**, *460*, 141688. DOI
147. Liu, X.; Wang, J.; Ma, C.; et al. Dual-isolation effect of bismuth in non-noble BiNi alloys for enhanced performance in $H_2O_2$ electrosynthesis. *ACS. Catal.* **2025**, *15*, 1819-28. DOI
148. Du, J.; Jiang, S.; Zhang, R.; et al. Generation of Pd-O for promoting electrochemical $H_2O_2$ production. *ACS. Catal.* **2023**, *13*, 6887-92. DOI
149. Zhang, X.; Wang, C.; Chen, K.; et al. Optimizing the Pd sites in pure metallic aerogels for efficient electrocatalytic $H_2O_2$ production. *Adv. Mater.* **2023**, *35*, 2211512. DOI
150. Lin, S. C.; Chang, C. W.; Tsai, M. H.; et al. Decreasing the $O_2$-to-$H_2O_2$ kinetic energy barrier on dilute binary alloy surfaces with controlled configurations of isolated active atoms. *Adv. Funct. Mater.* **2024**, *34*, 2314281. DOI
151. Hu, R.; Wei, L.; Xian, J.; et al. Microwave shock process for rapid synthesis of 2D porous $La_{0.2}Sr_{0.8}CoO_3$ perovskite as an efficient oxygen evolution reaction catalyst. *Acta. Phys. Chim. Sin.* **2023**, *39*, 2212025. DOI
152. Liu, R.; Kan, H.; Ma, X.; et al. Hydroxyl self-trapping strategy enables electrocatalysis at ampere-level current densities: kinetics-driven lattice oxygen activation for Cl-rich alkaline water electrooxidation. *Carbon. Energy.* **2025**, *8*, e70143. DOI
153. Wang, J.; Xu, K.; Yu, Z.; et al. Lead-doped ruthenium-iridium oxide catalysts for durable acidic oxygen evolution in proton exchange membrane electrolyzers at 3 A $cm^{-2}$. *Mater. Futures.* **2026**, *5*, 015101. DOI
154. Wang, M.; Zhang, H.; Dai, J.; et al. Non-equilibrium construction of layered ruddlesden-popper $La_2NiO_4$ porous nanosheets for efficient urea electrooxidation. *Carbon. Neutral.* **2026**, *5*, e70132. DOI
155. Xue, L.; Li, Y.; Deng, Y. Multicomponent porous metal oxide semiconductors for advanced gas sensing. *Micro. Nano. Sci.* **2025**, *1*, 2. DOI
156. Zhang, S.; Gong, J.; Rong, Z.; Mao, W.; Chu, L. Blade coating large-area 3D/1D perovskite heterojunction films for effective synaptic memristors. *Int. J. Miner. Metall. Mater.* **2026**, *33*, 2778-86. DOI
157. Kim, J.; Kwon, I. S.; Lim, J.; et al. Machine-learning-guided tungsten single atoms promote oxyhydroxides for noble-metal-free water electrolysis. *Nat. Commun.* **2026**, *17*, 2344. DOI PubMed PMC

158. Wang, T.; Xing, Z.; Wang, M.; et al. Bioinspired $O_2$-evolution catalysts with proton-coupled electron transfer pathway for portable oxygen generation. *Adv. Mater.* **2025**, *37*, 2502102. DOI
159. Hao, Y.; Li, J.; Cao, X.; et al. Origin of the universal potential-dependent organic oxidation on nickel oxyhydroxide. *ACS. Catal.* **2023**, *13*, 2916-27. DOI
160. Liu, S.; Wu, L.; Tang, D.; et al. Transition from sequential to concerted proton-coupled electron transfer of water oxidation on semiconductor photoanodes. *J. Am. Chem. Soc.* **2023**, *145*, 23849-58. DOI
161. Guo, X.; Qiu, L.; Li, M.; et al. Accelerating the generation of NiOOH by in-situ surface phosphating nickel sulfide for promoting the proton-coupled electron transfer kinetics of urea electrolysis. *Chem. Eng. J.* **2024**, *483*, 149264. DOI
162. Yue, Y.; Zhu, K.; Li, X.; Ye, K. Porous metal-based catalysts for water electrolysis. *Mater. Futures.* **2025**, *4*, 032001. DOI
163. Cheng, K.; Liu, C.; Wang, Y.; et al. Design of noble metal catalysts and reactors for the electrosynthesis of hydrogen peroxide. *Acta. Phys. Chim. Sin.* **2025**, *41*, 100112. DOI
164. Yin, H.; Yuan, J.; Wang, J.; Hu, S.; Wang, P.; Xie, H. Crystalline nitrogen-doped-carbon anchored well-dispersed $Fe_3O_4$ nanoparticles for real-time scalable neutral $H_2O_2$ electrosynthesis. *Energy. Environ. Sci.* **2025**, *18*, 2231-42. DOI
165. Hu, X.; Mei, G.; Chen, X.; Liu, J.; Xia, B. Y.; You, B. Simultaneous generation of $H_2O_2$ and formate by Co-electrolysis of water and $CO_2$ over bifunctional Zn/$SnO_2$ nanodots. *Angew. Chem. Int. Ed.* **2023**, *62*, e202304050. DOI
166. Zhou, Y.; Xu, L.; Wu, J.; et al. The operation active sites of $O_2$ reduction to $H_2O_2$ over ZnO. *Energy. Environ. Sci.* **2023**, *16*, 3526-33. DOI
167. Deng, D.; Wang, Y.; Jiang, J.; et al. Indium oxide with oxygen vacancies boosts $O_2$ adsorption and activation for electrocatalytic $H_2O_2$ production. *Chem. Commun.* **2024**, *60*, 9364-7. DOI
168. Wondimu, T. H.; Yong, Z.; Shah, A. A.; et al. The recent progress of high-entropy layered double hydroxides and high-entropy amorphous materials for water electrocatalysis. *DeCarbon* **2025**, *8*, 100110. DOI
169. Zhang, T.; Fan, H. J. Grafted superstructure renders catalyst stability in alkaline water oxidation. *cScience* **2025**, *1*, e70000. DOI
170. Elbachraoui, F.; Aymé-Perrot, D.; Girault, H. H. Ionic transport aspects of water electrolysis in alkaline media. *Research* **2025**, *8*, 0788. DOI PubMed PMC
171. Nie, J.; Jiang, Q.; Sang, Z.; et al. Accelerating water dissociation to achieve ampere-level hydrogen peroxide electrosynthesis in brine and seawater. *Nat. Commun.* **2025**, *16*, 5895. DOI PubMed PMC
172. Zhang, T.; Wang, W.; Liu, W.; Guo, Z.; Liu, J. Residual ligand-functionalized ultrathin $Ni(OH)_2$ via reconstruction for high-rate $HO_2^-$-electrosynthesis. *Nat. Commun.* **2025**, *16*, 5240. DOI PubMed PMC
173. Qi, D.; Xu, J.; Zhou, Y.; et al. Cyclodextrin-supported $Co(OH)_2$ clusters as electrocatalysts for efficient and selective $H_2O_2$ synthesis. *Angew. Chem. Int. Ed.* **2023**, *62*, e202307355. DOI
174. Yu, K.; Yang, H.; Xu, J.; et al. Synergistic active heterostructure design for enhanced two electron oxygen reduction via chemical and electrochemical reconstruction of heterosulfides. *Angew. Chem. Int. Ed.* **2024**, *63*, e202408508. DOI
175. Li, M.; Han, Z.; Hu, Q.; et al. Recent progress in solar-driven $CO_2$ reduction to multicarbon products. *Chem. Soc. Rev.* **2024**, *53*, 9964-75. DOI
176. Shi, Z.; Zhou, L.; Pan, S.; et al. Confinement phosphorization strategy unlocks FeP-N-C catalysts for highly stable zinc-air batteries. *Carbon. Neutral.* **2025**, *4*, e70065. DOI
177. Tao, W.; He, G.; Feng, Q.; et al. Direct charge-transfer transition drives triplet generation and photon upconversion in 2D hybrid perovskites. *J. Am. Chem. Soc.* **2025**, *147*, 47280-8. DOI
178. Hong, L.; Jing, C.; Zhang, Y.; Huang, H.; Jiang, Q.; Tang, J. Heterostructures with transition metal sulfides and transition metal phosphide: NiMnS/FeP achieve efficient seawater OER. *J. Environ. Chem. Eng.* **2025**, *13*, 115224. DOI
179. Nishiwaki, E.; Kuo, D.; Cossairt, B. M. Utilizing the complexity of transition metal phosphide surfaces to tune nitrate reduction selectivity. *Meet. Abstr.* **2023**, *MA2023-02*, 2778. DOI
180. Guo, W.; Zhang, S.; Zhang, J.; et al. Accelerating multielectron reduction at $Cu_xO$ nanograins interfaces with controlled local electric field. *Nat. Commun.* **2023**, *14*, 7383. DOI PubMed PMC
181. Li, H.; Shao, Y.; Zhang, Z.; et al. Understanding the unique selectivity of cobalt phthalocyanine in multielectron reduction of carbon dioxide. *ACS. Catal.* **2024**, *15*, 139-47. DOI
182. Gui, T.; Wu, Z.; Li, J.; et al. Transition metal phosphides for seawater electrolysis: dynamic reconstruction, synergistic mechanisms and design paradigms. *Adv. Funct. Mater.* **2026**, *36*, e26293. DOI
183. Wang, W.; Wang, A.; Xu, J.; et al. Surface reconstruction of pyrite-type transition metal sulfides during oxygen evolution reaction. *J. Colloid. Interface. Sci.* **2024**, *657*, 334-43. DOI
184. Zhang, C.; Shan, P.; Zou, Y.; et al. Stable and high-yield hydrogen peroxide electrosynthesis from seawater. *Nat. Sustain.* **2025**, *8*, 542-52. DOI

185. Che, H.; Wang, X.; Yue, H.; et al. Precise regulation of D-band centers inducing to high-efficiency dual-channel piezocatalytic $H_2O_2$ production. *Adv. Funct. Mater.* **2025**, *36*, e16979. DOI
186. Kim, S. H.; Kim, J. H.; Park, B.; et al. Facet-controlled growth of molybdenum phosphide single crystals for efficient hydrogen peroxide synthesis. *Adv. Mater.* **2025**, *37*, 2500250. DOI
187. Kim, J. H.; Lee, J. G.; Kim, C. S.; Choi, M. J. Ligand-driven electron-deficient cobalt pentlandite nanocrystals for efficient hydrogen peroxide electrosynthesis. *Energy. Environ. Mater.* **2024**, *8*, e12848. DOI
188. Hu, C.; Zhang, G.; Duan, Q.; et al. Advances in surface-modification-driven functional MXenes for multidisciplinary applications. *Smart. Mater. Devices.* **2026**, *2*, 202601. DOI
189. Cai, J.; Wu, Z.; Wang, S.; et al. Exploring advanced microwave strategy for the synthesis of two-dimensional energy materials. *Appl. Phys. Rev.* **2024**, *11*, 041320. DOI
190. Luo, L.; Wang, Q.; Xiong, Y.; Mao, G.; Wang, H.; Lu, S. Ordered bimetallic Pt-based intermetallic catalysts enable highly efficient oxygen reduction reaction in zinc-air batteries. *Carbon. Neutral.* **2026**, *5*, e70114. DOI
191. Ao, X.; Wu, F.; Yu, L.; Zhao, K.; Humayun, M.; Wang, C. Tailoring antiperovskite carbide for electrocatalysis hydrogen evolution applications. *Chin. J. Struct. Chem.* **2026**, *45*, 100851. DOI
192. Kwon, H. R.; Yang, J. W.; Jang, H. W. Metal nitride catalysts for photoelectrochemical and electrochemical catalysis. *Exploration* **2025**, *5*, 20240013. DOI PubMed PMC
193. Tan, Z. W.; Agesta, N. F.; Yeo, R. Y. Z.; Foo, J. J.; Ong, W. J. Unlocking the potential of carbon nitride ($C_xN_y$) electrocatalysts in hydrogen evolution, oxygen evolution and overall water splitting. *Exploration* **2026**, *6*, 20240008. DOI PubMed PMC
194. Peng, S.; Wang, X.; Bi, J.; et al. Wafer-scale epitaxy of TiN nanoarrays on fluorophlogopites for flexible, refractory, and multifunctional plasmonic metamaterials. *Innov. Mater.* **2026**, *4*, 100189. DOI
195. Yoo, R. M. S.; Ngozichukwu, B.; Yesudoss, D. K.; et al. Vibrational property tuning of MXenes revealed by sublattice N reactivity in polar and nonpolar solvents. *J. Am. Chem. Soc.* **2025**, *147*, 10104-17. DOI PubMed PMC
196. Li, N.; Huo, J.; Zhang, Y.; et al. Transition metal Carbides/Nitrides (MXenes): properties, synthesis, functional modification and photocatalytic application. *Sep. Purif. Technol.* **2024**, *330*, 125325. DOI
197. Liu, J.; Zhang, Z.; Wang, X.; Han, C.; Yang, M. Triazolate-functionalized zirconium nitride for air-fed $H_2O_2$ production with industrial-level current density. *J. Am. Chem. Soc.* **2025**, *147*, 36618-25. DOI
198. Li, B.; Ma, C.; Liu, X.; et al. Ordered Ni-Zn-C intermetallics enable highly selective two-electron oxygen reduction and efficient peroxone oxidation. *Appl. Catal. B. Environ. Energy.* **2026**, *391*, 126702. DOI
199. Liu, J.; Zhang, Z.; Xu, Z.; et al. Tailoring oxygen adsorption on nickel nitride for selective $2e^-$ ORR to hydrogen peroxide. *Chem. Eng. J.* **2025**, *519*, 165448. DOI
200. Yin, J.; Jin, J.; Yin, Z.; et al. The built-in electric field across FeN/$Fe_3N$ interface for efficient electrochemical reduction of $CO_2$ to CO. *Nat. Commun.* **2023**, *14*, 1724. DOI PubMed PMC
201. Du, J.; Han, G.; Zhang, X.; et al. Chaos of active site structure as a ladder to climbing the apex of the $2e^-$ ORR volcano plot. *J. Am. Chem. Soc.* **2026**, *148*, 6905-14. DOI
202. Sun, Y.; Fan, K.; Li, J.; et al. Boosting electrochemical oxygen reduction to hydrogen peroxide coupled with organic oxidation. *Nat. Commun.* **2024**, *15*, 6098. DOI PubMed PMC
203. Yan, M.; Wei, Z.; Gong, Z.; et al. $Sb_2S_3$-templated synthesis of sulfur-doped Sb-N-C with hierarchical architecture and high metal loading for $H_2O_2$ electrosynthesis. *Nat. Commun.* **2023**, *14*, 368. DOI PubMed PMC
204. Zhang, Z.; Zhou, F.; Wang, Y.; et al. Synergistic $t_{2g}$-to-π* electron transfer and nanotube engineering in spinal catalysts for ultra-efficient chloride evolution. *Angew. Chem. Int. Ed.* **2025**, *64*, e202513009. DOI
205. Shao, L. Y.; Wang, Y.; Meng, J.; et al. Exclusive bridged *OCHO pathway activated by phenol-quinone conversion on the surface of $Cu(OH)_2$ for highly selective formate production in $CO_2$ electroreduction. *Adv. Funct. Mater.* **2025**, *36*, e14222. DOI
206. Wang, Z.; Liu, D.; Xia, C.; et al. Tip carbon encapsulation customizes cationic enrichment and valence stabilization for low $K^+$ acidic $CO_2$ electroreduction. *Nat. Commun.* **2025**, *16*, 1754. DOI PubMed PMC
207. Bao, T.; Wu, Y.; Tang, C.; et al. Highly ordered conductive metal-organic frameworks with chemically confined polyoxometalate clusters: a dual-functional electrocatalyst for efficient $H_2O_2$ synthesis and biomass valorization. *Adv. Mater.* **2025**, *37*, 2500399. DOI
208. Zou, Y.; Zhang, Y.; Zhang, C.; et al. Hydrogen-bonded organic framework@conductive metal-organic framework heterostructures for ampere-level hydrogen peroxide production. *Nat. Commun.* **2025**, *16*, 10908. DOI PubMed PMC
209. Sun, M.; Peng, Y.; Duan, C.; et al. Field-regulated dynamics at electrode/electrolyte interface toward efficient $H_2O_2$ generation via two-electron water oxidation. *Adv. Funct. Mater.* **2025**, *36*, e13578. DOI

210. Tian, F.; Chang, W.; Liang, P.; et al. Charge redistribution dynamics in chalcogenide-stabilized cuprous electrocatalysts unleash ampere-scale partial current toward formate production. *Nat. Commun.* **2025**, *16*, 9426. DOI PubMed PMC
211. Ling, Z.; Yin, Y.; Ni, W.; et al. Efficient $CO_2$-To-HCOOH conversion at industrial current density in strong acid via synergistic water activation. *Adv. Funct. Mater.* **2025**, *36*, e29166. DOI
212. Shi, Y.; Liu, Y.; Dong, H.; et al. Operando nuclear magnetic resonance decodes alkali-tuned proton-electron relay boosting $CO_2$-to-formate conversion. *Nat. Commun.* **2026**, *17*, 2136. DOI PubMed PMC
213. Chen, Q.; Li, B.; Gu, J.; et al. Selective electrosynthesis of nitrite from nitrate catalyzed by perovskite hydroxide $CuSn(OH)_6$. *ACS. Sustain. Chem. Eng.* **2025**, *13*, 4046-54. DOI
214. Mao, Z.; Zhang, J.; Tu, T.; et al. Cerium driven active site relocation in spinel $Co_3O_4$ enables stable chlorine evolution in acidic media. *Nat. Commun.* **2026**, *17*, 3763. DOI PubMed PMC
215. Zhao, S.; Li, H.; Dai, J.; et al. Selective electrosynthesis of chlorine disinfectants from seawater. *Nat. Sustain.* **2024**, *7*, 148-57. DOI
216. Li, H.; Xin, X.; Sun, W.; Li, C.; Zhong, B. Regenerable surface-reconstructed silver mesh enables high-throughput electrocatalytic nitrate-to-nitrite conversion for near-perfect $N_2$ selectivity in a tandem system. *J. Colloid. Interface. Sci.* **2026**, *702*, 139018. DOI
217. Zhang, W.; Guo, F.; Gong, W.; et al. Electrochemical shortcut denitrification coupled with chemical diazotization for low-carbon nitrate wastewater treatment. *Angew. Chem. Int. Ed.* **2025**, *65*, e16226. DOI
218. Guo, J.; Brimley, P.; Liu, M. J.; et al. Mass transport modifies the interfacial electrolyte to influence electrochemical nitrate reduction. *ACS. Sustain. Chem. Eng.* **2023**, *11*, 7882-93. DOI
219. Li, H.; Wang, L.; Du, Q.; Liu, C.; Li, C.; Sun, W. Synergistic nitrate removal: coupling electrocatalysis and chemical reduction for exceptional nitrogen selectivity. *Chem. Eng. J.* **2024**, *496*, 153972. DOI
220. Liu, Y.; Li, C.; Tan, C.; et al. Electrosynthesis of chlorine from seawater-like solution through single-atom catalysts. *Nat. Commun.* **2023**, *14*, 2475. DOI PubMed PMC
221. Adam, D. B.; Tsai, M.; Awoke, Y. A.; et al. Iodide oxidation reaction catalyzed by ruthenium-tin surface alloy oxide for efficient production of hydrogen and iodine simultaneously. *ACS. Sustain. Chem. Eng.* **2021**, *9*, 8803-12. DOI
222. Ma, J.; Lee, W.; Kim, J. H.; et al. Leveraging the intermetal distance in dual-atom catalysts: revealing optimized synergistic interactions for $CO_2$ electroreduction. *ACS. Nano.* **2025**, *19*, 18698-707. DOI
223. Sun, W.; Liu, S.; Sun, H.; et al. Low-coordinated Ni single atom catalyst with carbon coordination for efficient $CO_2$ electroreduction. *Adv. Energy. Mater.* **2025**, *15*, 2500283. DOI
224. Ni, L.; Wang, P.; Wang, Y. Sustainable electro-fenton antifouling strategy simultaneously improves nitrogen-removal efficiency of anammox in membrane bioreactors. *Environ. Sci. Technol.* **2025**, *59*, 17545-57. DOI
225. Zang, Y.; Liu, Y.; Lu, R.; et al. Tuning transition metal 3d spin state on single-atom catalysts for selective electrochemical $CO_2$ reduction. *Adv. Mater.* **2025**, *37*, 2417034. DOI PubMed PMC
226. Liu, M.; Liu, S.; Xu, Q.; et al. Dual atomic catalysts from COF-derived carbon for $CO_2$RR by suppressing HER through synergistic effects. *Carbon. Energy.* **2023**, *5*, e300. DOI
227. Hamkins, K. S.; Vallez, L.; Zheng, X. Platinum-supported indium tin oxide catalyst for efficient $H_2O_2$ production via two-electron water oxidation reaction. *ACS. Catal.* **2025**, *15*, 11431-9. DOI
228. Khan, R.; Chakraborty, J.; Singh Rawat, K.; et al. Super-oxidizing covalent triazine framework electrocatalyst for two-electron water oxidation to $H_2O_2$. *Angew. Chem. Int. Ed.* **2023**, *62*, e202313836. DOI
229. Liu, Z.; Liu, Y.; Zhang, Y.; et al. Universal catalyst design framework for electrochemical hydrogen peroxide synthesis facilitated by local atomic environment descriptors. *Angew. Chem. Int. Ed.* **2025**, *65*, e18027. DOI
230. Barasa Guta, C.; Gemechu Edao, H.; Bafe Dilebo, W.; et al. Novel electrocatalyst with abundant oxygen vacancies enabling efficient two-electron water oxidation reaction for $H_2O_2$ synthesis. *Chem. Eng. J.* **2024**, *500*, 156418. DOI
231. Xiao, L.; Zhou, R.; Zhang, T.; et al. Porous indium nanocrystals on conductive carbon nanotube networks for high-performance $CO_2$-to-formate electrocatalytic conversion. *Energy. Environ. Mater.* **2023**, *7*, e12656. DOI
232. Jiang, Z.; Ren, S.; Cao, X.; et al. pH-universal electrocatalytic $CO_2$ reduction with ampere-level current density on doping-engineered bismuth sulfide. *Angew. Chem. Int. Ed.* **2024**, *63*, e202408412. DOI
233. Zhang, B.; Liu, W.; Liu, Z.; et al. Scalable and efficient electrochemical bromination of arenes with Faradaic efficiencies surpassing 90%. *Nat. Commun.* **2025**, *16*, 3052. DOI PubMed PMC
234. Tao, Z.; Wu, Z.; Wu, Y.; Wang, H. Activating copper for electrocatalytic $CO_2$ reduction to formate via molecular interactions. *ACS. Catal.* **2020**, *10*, 9271-5. DOI
235. Nie, J.; Li, Z.; Liu, W.; et al. Recent progress in oxygen reduction reaction toward hydrogen peroxide electrosynthesis and cooperative coupling of anodic reactions. *Adv. Mater.* **2025**, *37*, 2420236. DOI

236. Wang, Q.; Ren, L.; Zhang, J.; et al. Recent progress on the catalysts and device designs for (photo)electrochemical on-site $H_2O_2$ production. *Adv. Energy. Mater.* **2023**, *13*, 2301543. DOI
237. Xu, L.; Nan, X.; Yu, J. C. Recent progress on graphitic carbon nitride-based photocatalysts for hydrogen peroxide synthesis. *Exploration* **2026**, *6*, 20240484. DOI PubMed PMC
238. Chen, J.; Ma, Q.; Zheng, X.; Fang, Y.; Wang, J.; Dong, S. Kinetically restrained oxygen reduction to hydrogen peroxide with nearly 100% selectivity. *Nat. Commun.* **2022**, *13*, 2808. DOI PubMed PMC
239. Zhang, C.; Lu, R.; Liu, C.; et al. Trimetallic sulfide hollow superstructures with engineered d-band center for oxygen reduction to hydrogen peroxide in alkaline solution. *Adv. Sci.* **2022**, *9*, 2104768. DOI PubMed PMC
240. Yang, M.; Zhao, Z.; Zhi, T.; et al. Multiscale catalyst engineering for stable, selective, and carbon-neutral industrial hydrogen peroxide electrosynthesis. *Carbon. Neutral.* **2025**, *4*, e70017. DOI
241. Huang, H.; Sun, F.; Luo, Z.; et al. MOF@MOF hierarchical heterotructures for enhanced photocatalytic $H_2O_2$ production and furfuryl alcohol oxidation. *Chin. J. Struct. Chem.* **2025**, *44*, 100717. DOI
242. Zhang, H.; Li, H.; Zhang, X.; Yu, S.; Wang, S.; Sun, G. Enhanced metal-support interaction of nitrogen-doped carbon supported Pt nanoparticles with high activity for electrocatalytic oxygen reduction reaction. *Carb. Neutrality.* **2025**, *4*, 10. DOI
243. Kang, D.; Zhang, C.; Wang, X.; et al. Efficient atomically dispersed Fe catalysts with robust three-phase interface for stable seawater-based zinc-air batteries. *Green. Carbon.* **2025**, *3*, 1-10. DOI
244. Liu, J.; Li, S.; Li, H.; Wan, X.; Shui, J. Oxophilic $Yb_2O_3$ nanoparticles as radical scavengers to enhance the durability of Fe-N-C oxygen reduction catalysts. *Smart. Mol.* **2026**, *4*, e70049. DOI PubMed PMC
245. Li, L.; Qin, N.; Ma, H.; et al. Rational design of nitrogen and fluorine co-doped metal-free porous carbons electrocatalysts for highly efficient oxygen reduction and zinc-air batteries. *Carb. Neutrality.* **2025**, *4*, 1. DOI
246. Liu, R.; Wang, C.; Yan, Y.; Wang, R.; Chen, G. Reversed charge transfer to modulate the d-band center of Pd for efficient direct $H_2O_2$ synthesis. *ACS. Catal.* **2024**, *14*, 3955-65. DOI
247. Hu, J.; Shang, W.; Xin, C.; et al. Uncovering dynamic edge-sites in atomic Co-N-C electrocatalyst for selective hydrogen peroxide production. *Angew. Chem. Int. Ed.* **2023**, *62*, e202304754. DOI
248. Wang, J.; Huang, J.; Jia, C.; et al. Catalyst-engineered proton transfer pathways for selective hydrogen peroxide electrosynthesis in solid-state electrolytes. *Angew. Chem. Int. Ed.* **2025**, *64*, e202510645. DOI
249. Wang, Y.; Duan, P.; Liao, Y.; et al. Differentiating interfacial water structures via alkali metal cation promotor for $H_2O_2$ electrosynthesis in acid. *Nat. Commun.* **2026**, *17*, 4973. DOI PubMed PMC
250. Cheng, F.; Liu, Y.; Zhao, Z.; et al. Enhanced proton-feeding kinetics of metal-organic framework toward industrial-level $H_2O_2$ electrosynthesis for sustainable bleaching. *Nat. Commun.* **2025**, *16*, 10183. DOI PubMed PMC
251. Xie, H.; Nie, G.; Fang, Y.; et al. Synergistically boosting charge separation and surface activity for efficient solar-powered cathodic metal protection. *Carb. Neutrality.* **2026**, *5*, 1. DOI
252. Liu, H.; Luo, G.; Han, Q.; et al. Generation of hydrogen peroxide by using solid $CaCO_3$ suspension via two-electron water oxidation. *Chem. Eng. J.* **2025**, *518*, 164498. DOI
253. Zhou, Q.; Yan, Z.; Lan, Y.; et al. A general strategy to enhance hydrogen peroxide generation via two-electron water oxidation by antimony modification for removal of triethyl phosphate and hexavalent chromium. *Appl. Catal. B. Environ.* **2024**, *342*, 123427. DOI
254. Lei, Y.; Gao, L.; Ling, C.; Guo, S. Q. Electrosynthesis of hydrogen peroxide via two-electron water oxidation reaction: mechanistic insights, materials design, and practical feasibility. *Chem. Eng. J.* **2026**, *535*, 175221. DOI
255. Feng, J.; Chen, J.; Xu, F.; et al. Boosting photocatalytic $H_2O_2$ production via two-electron water oxidation over Ag decorated on ZIF-8 derived ZnO nanostructure. *Chem. Eng. J.* **2026**, *538*, 176632. DOI
256. Kim, C.; Park, S. O.; Kwak, S. K.; Xia, Z.; Kim, G.; Dai, L. Concurrent oxygen reduction and water oxidation at high ionic strength for scalable electrosynthesis of hydrogen peroxide. *Nat. Commun.* **2023**, *14*, 5822. DOI PubMed PMC
257. Zhang, X.; Wan, Y.; Wen, Y.; et al. SnSe nanosheets with Sn vacancies catalyse $H_2O_2$ production from water and oxygen at ambient conditions. *Nat. Catal.* **2025**, *8*, 465-75. DOI
258. Xu, J.; Zhang, Q.; Gao, X.; et al. Highly efficient $Fe^{III}$-initiated self-cycled fenton system in piezo-catalytic process for organic pollutants degradation. *Angew. Chem. Int. Ed.* **2023**, *62*, e202307018. DOI
259. Li, L.; Hu, Z.; Kang, Y.; et al. Electrochemical generation of hydrogen peroxide from a zinc gallium oxide anode with dual active sites. *Nat. Commun.* **2023**, *14*, 1890. DOI PubMed PMC
260. Tian, G. Disentangling activity-selectivity trade-offs in $CO_2$ conversion through multifunctional catalytic systems. *cScience* **2026**, *2*, e70020. DOI

261. Fang, G.; Liu, K.; Fan, M.; et al. Unveiling the electron configuration-dependent oxygen evolution activity of 2D porous Sr-substituted $LaFeO_3$ perovskite through microwave shock. *Carbon. Neutral.* **2023**, *2*, 709-20. DOI
262. Yan, F.; Bai, B.; Huang, J.; Xu, J.; Fu, Y. Rational design of transition-metal dual-atom catalysts: exploiting neighboring effects for efficient $CO_2$ Reduction. *Carbon. Neutral.* **2026**, *5*, e70146. DOI
263. Wang, S.; Yang, Y.; Xu, W.; et al. Crucial role of hydroxyl in CO selectivity for integrated $CO_2$ capture and electrocatalytic reduction. *Carb. Neutrality.* **2026**, *5*, 4. DOI
264. Lu, R.; Liu, Y.; Wang, Z. Advances in the understanding of selective $CO_2$ reduction catalysis. *EcoEnergy* **2024**, *2*, 695-713. DOI
265. Xing, L. Electrified $CO_2$-to-methanol pathways: a time-resolved roadmap from deployment to disruption. *cScience* **2026**, *2*, e70018. DOI
266. Liu, W.; Duan, X.; Jiang, L.; et al. Compressed carbon dioxide energy storage in salt caverns holds promise for China's hard-to-abate sectors. *Innov. Energy.* **2025**, *2*, 100065. DOI
267. Zhang, H.; Wang, X.; Chen, C.; et al. Selective $CO_2$-to-formic acid electrochemical conversion by modulating electronic environment of copper phthalocyanine with defective graphene. *Chin. J. Struct. Chem.* **2023**, *42*, 100089. DOI
268. Mang, C.; Luo, S.; Luo, J.; Li, H.; Li, G.; Jiang, T. ZnO@cryptomelane-type $MnO_2$ heterostructures for high-efficiency photocatalytic $CO_2$ reduction: synergistic charge transfer and reaction pathway elucidation. *cScience* **2026**, *2*, e70012. DOI
269. Peng, C.; Yan, M.; Liu, Z. Regulating oxygen defects over $CeO_2$ via rare earth oxide doping for Pt-catalyzed oxidative dehydrogenation of propane with carbon dioxide. *Smart. Mater. Devices.* **2026**, *2*, 202604. DOI
270. Du, J. H.; Liu, Z.; Sheng, T.; et al. Host-guest metal interaction in Cu-In single atom alloy switching electrocatalytic $CO_2$ reduction pathway. *Angew. Chem. Int. Ed.* **2025**, *64*, e202512970. DOI
271. Chen, F.; Elgazzar, A.; Pecaut, S.; et al. Electrochemical nitrate reduction to ammonia with cation shuttling in a solid electrolyte reactor. *Nat. Catal.* **2024**, *7*, 1032-43. DOI
272. Gu, X.; Zhang, J.; Guo, S.; et al. Tiara Ni clusters for electrocatalytic nitrate reduction to ammonia with 97% faradaic efficiency. *J. Am. Chem. Soc.* **2025**, *147*, 22785-95. DOI PubMed PMC
273. Guo, C.; Guo, M.; Zhang, Y.; Han, S.; Yu, Y. Lattice hydrogen involved electrocatalytic nitrate reduction to hydroxylamine. *J. Am. Chem. Soc.* **2025**, *147*, 14869-77. DOI
274. Wu, Z.; Song, Y.; Guo, H.; et al. Tandem catalysis in electrocatalytic nitrate reduction: unlocking efficiency and mechanism. *Interd. Mater.* **2024**, *3*, 245-69. DOI
275. Li, J.; Wang, Y.; Ji, X.; et al. Unraveling tandem catalytic sites for electrocatalytic nitrate reduction to ammonia. *Adv. Energy. Mater.* **2025**, *16*, e03822. DOI
276. Zhang, H.; Fang, K.; Yang, J.; et al. Strategies and applications of electrocatalytic nitrate reduction towards ammonia. *Coord. Chem. Rev.* **2024**, *506*, 215723. DOI
277. Murphy, E.; Liu, Y.; Matanovic, I.; et al. Elucidating electrochemical nitrate and nitrite reduction over atomically-dispersed transition metal sites. *Nat. Commun.* **2023**, *14*, 4554. DOI PubMed PMC
278. Jiang, H.; Chen, G. F.; Savateev, O.; et al. Enabled efficient ammonia synthesis and energy supply in a zinc-nitrate battery system by separating nitrate reduction process into two stages. *Angew. Chem. Int. Ed.* **2023**, *62*, e202218717. DOI
279. Liang, N.; Choi, W.; Suk, Han. D.; Park, H. Electrocatalytic conversion of ethylene to ethylene oxide mediated by halide oxidation: chloride vs. bromide vs. iodide. *Chem. Eng. J.* **2024**, *494*, 153042. DOI
280. Li, R.; Zhang, L.; Qin, X.; et al. Efficient photocatalytic two-electron halide oxidation over p-block metal Bi- and Sb-based catalysts. *ACS. Catal.* **2025**, *15*, 2171-9. DOI
281. Pang, H.; Ji, X.; Liu, Y.; et al. Tailoring Se-mediated Co-Co dual-atom sites for oxygen and iodide electrocatalysis toward high-efficiency and ultradurable zinc-air/iodide hybrid batteries. *Carbon. Energy.* **2026**, *8*, e70221. DOI
282. Maiti, A.; Pachfule, P.; Biswas, A.; Mahalingam, V.; Bhunia, A. Controlled heterogeneous electrocatalytic oxidation of carboxylates and halides for the synthesis of novel chemicals. *ChemCatChem* **2025**, *17*, e202500069. DOI
283. Li, X.; Liu, T.; Li, P.; et al. Aqueous alkaline zinc-iodine battery with two-electron transfer. *ACS. Nano.* **2025**, *19*, 2900-8. DOI
284. Xu, Y.; Xie, C.; Li, T.; Li, X. A high energy density bromine-based flow battery with two-electron transfer. *ACS. Energy. Lett.* **2022**, *7*, 1034-9. DOI
285. Chen, Z.; Wang, Y.; Wei, Z.; et al. Highly efficient chlorine fixation based on organic selenium for 3.7-V aqueous batteries. *J. Am. Chem. Soc.* **2026**, *148*, 11531-9. DOI PubMed PMC
286. Lu, H.; Zhuang, X.; Ding, J.; et al. Ion-defect dual management for achieving efficient air-processed perovskite solar cells with certified efficiency 27.1%. *Adv. Mater.* **2026**, *38*, e17596. DOI
287. Li, X.; Wang, Y.; Lu, J.; et al. Constructing static two-electron lithium-bromide battery. *Sci. Adv.* **2024**, *10*, eadl0587. DOI PubMed PMC

288. Cho, J.; Lim, T.; Kim, H.; et al. Importance of broken geometric symmetry of single-atom Pt sites for efficient electrocatalysis. *Nat. Commun.* **2023**, *14*, 3233. DOI PubMed PMC

**Disclaimer/Publisher's Note:** All statements, opinions, and data contained in this publication are solely those of the individual author(s) and contributor(s) and do not necessarily reflect those of OAE and/or the editor(s). OAE and/or the editor(s) disclaim any responsibility for harm to persons or property resulting from the use of any ideas, methods, instructions, or products mentioned in the content.



© The Author(s) 2026. Open Access This article is licensed under a Creative Commons Attribution 4.0 International License (https://creativecommons.org/licenses/by/4.0/), which permits unrestricted use, sharing, adaptation, distribution and reproduction in any medium or format, for any purpose, even commercially, as long as you give appropriate credit to the original author(s) and the source, provide a link to the Creative Commons license, and indicate if changes were made.